12-2022

Search for Gravitational Waves from Core Collapse Supernovae in Ligo's Observation Runs Using a Network of Detectors

Shahrear Khan Faisal

The University of Texas Rio Grande Valley

Recommended Citation

Faisal, Shahrear Khan, "Search for Gravitational Waves from Core Collapse Supernovae in Ligo's Observation Runs Using a Network of Detectors" (2022). *Theses and Dissertations*. 1137.
https://scholarworks.utrgv.edu/etd/1137

SEARCH FOR GRAVITATIONAL WAVES FROM CORE COLLAPSE SUPERNOVAE IN LIGO'S OBSERVATION RUNS USING A NETWORK OF DETECTORS

A Thesis

by

SHAHREAR KHAN FAISAL

Submitted in Partial Fulfillment of the
Requirements for the Degree of
MASTER OF SCIENCE

Major Subject: Interdisciplinary Studies

The University of Texas Rio Grande Valley

December 2022

SEARCH FOR GRAVITATIONAL WAVES FROM CORE COLLAPSE SUPERNOVAE IN LIGO'S OBSERVATION RUNS USING A NETWORK OF DETECTORS

A Thesis
by
SHAHREAR KHAN FAISAL

COMMITTEE MEMBERS

Dr. Soma Mukherjee
Chair of Committee

Dr. Soumya Mohanty
Committee Member

Dr. Malik Rakhmanov
Committee Member

December 2022

ABSTRACT

Faisal, Shahrear Khan, Search for Gravitational Waves from Core Collapse Supernovae in LIGO's observation runs using a network of detectors. Master of Science (MS), December, 2022, 82 pp., 2 tables, 41 figures, 96 references.

Core-Collapse Supernova (CCSN) is one of the most anticipated sources of Gravitational Waves (GW) in the fourth observation run (O4) of LIGO and other network of GW detectors. A very low rate of galactic CCSN, coupled with the fact that the CCSN waveforms are unmodeled, make detection of these signals extremely challenging. Mukherjee et. al. have developed a new burst search pipeline, the Multi-Layer Signal Enhancement with cWB and CNN or MuLaSEcC, that integrates a non-parametric signal estimation and Machine Learning. MuLaSEcC operates on GW data from a network of detectors and enhances the detection probability while reducing the false alarm significantly. The aim of this research is to analyze the detection probability of CCSN during O4 and how well the signals may be reconstructed for parameter estimation. CCSN waveforms are generated in supercomputers by the implementation of complex physics. The CCSN GW waveforms used in this analysis correspond to various explosion scenarios. These are Powell and Muller s18, Scheidegger R3E1AC_L, Ott 2013_s27_fheat1d00, Mezzacappa 2020_c15_3D, Morozova 2018_M13_SFHo_multipole, Andresen 2019 s15fr, Kuroda 2016_TM1, Kuroda 2017 s11.2 and Richers 2017 A300w0_50_HSDD2. The study has demonstrated improved result in terms of reduction in the false alarm rate and broadband reconstruction of the detected signals. Efficiency of the pipeline as a function of distance has been seen to be sensitive up to the galactic range. Receiver operating characteristics have been generated to demonstrate the performance of the pipeline in comparison to other standard operating pipelines within the GW community.

DEDICATION

I would like to dedicate this thesis to my parents, whose support has been irreplaceable.

ACKNOWLEDGMENTS

I would like to acknowledge my advisor Dr. Soma Mukherjee's guidelines and enormous support without which this thesis would not be possible. I am grateful to the past members of our research group Gaukhar Nurbek and Oscar Valdez who taught me everything about running the analysis. I would like to thank the members of my thesis committee Dr. Soumya Mohanty and Dr. Malik Rakhmanov for their help and suggestions. I also acknowledge LIGO Scientific Collboration (LSC) for access to the data required for our analysis and being able to run the analysis in LIGO High Performance Computing cluster. I was supported by UTRGV Presidential Graduate Research Assistantship during my master's studies.

TABLE OF CONTENTS

LIST OF TABLES

LIST OF FIGURES

CHAPTER I

INTRODUCTION

Gravitational waves (GW) were first predicted in Albert Einstein's General Theory of Relativity[3] 2nd and 3rd citations required. Gravitational waves are described as ripples in the curvature of space-time. These are generated by accelerated masses and they propagate as waves outward from their source at the speed of light. Gravita- tional Waves were first observed directly with the detection of GW signal from a binary black hole (BBH) system[4] in 2015 by the LIGO detectors[5, 6] at Hanford and Livingston. Several other BBH signals have been detected by the LIGO detectors in the following years. Some of the most notable observation are as follows. (i) In 2017 the LIGO and Virgo[7] detectors observed a GW signal from a colliding neutron star system (BNS)[8]; (ii) In 2019, an object of 2.6 solar masses was observed to merge with a black hole of 23 solar masses by LIGO and Virgo, placing it in the 'mass gap'[9].

The LIGO-Virgo-KAGRA[10] Collaboration published the third observation run catalog in November 2021 from the second phase of the third observation run (O3b). So far 90 observed events have been catalogued since LIGO and Virgo observations started[11, 12]. The distribution of the detected black holes and neutron stars as a function of mass has been shown in 1.0.1.

1.1 Sources of GW

Figure 1.1.1 shows the sources and corresponding detectors of the entire GW spectrum across the frequency band.

One type of GW is the background from the big bang itself and also other types of astrophysical processes taking place in the universe. And this background GW is responsible for the polarization

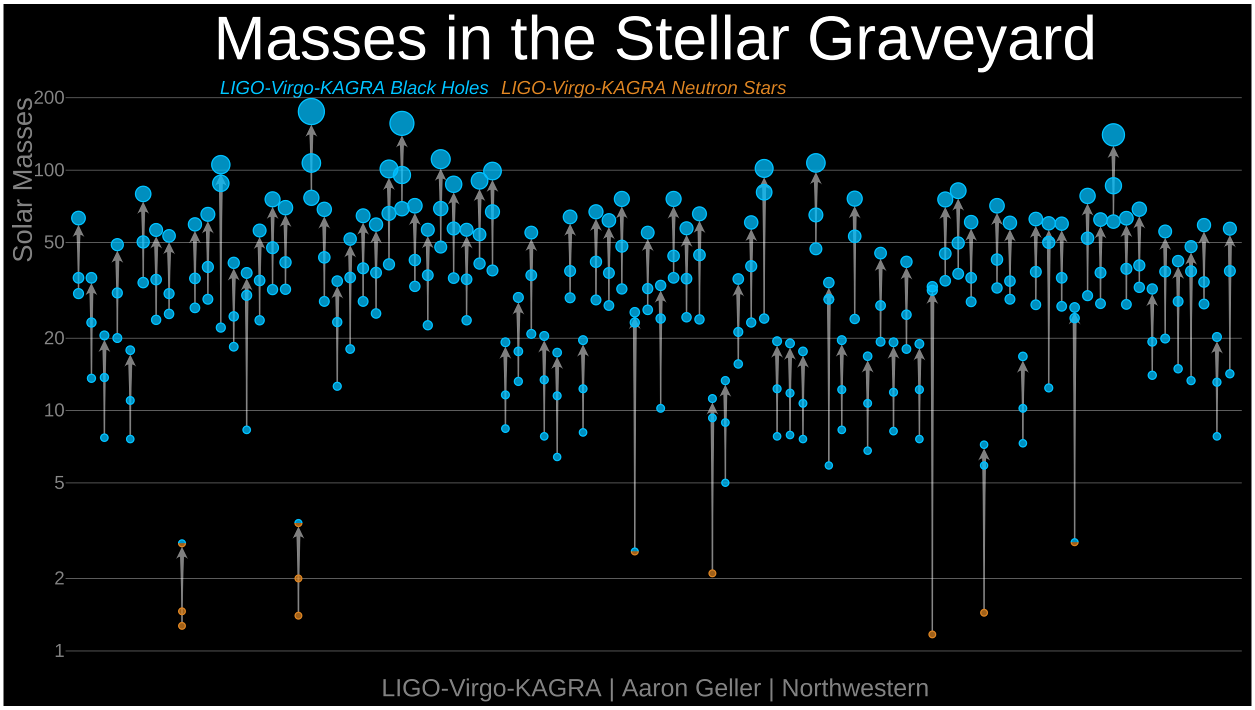

Figure 1.0.1: This figure shows the masses of all compact binaries detected by LIGO and Virgo. Black holes are shown in blue and neutron stars are shown in orange. [Credit: LIGO-Virgo / Aaron Geller / Northwestern University]

of Cosmic Microwave Background (CMB)[13]. Therefore, the CMB Polarization can work as a detector for the GW from the early universe. The frequency of this GW is around 10^{16} Hz. Supermassive black holes live at the centers of galaxies[14]. GWs are emitted when two galaxies with supermassive blackholes at their centers merge[15]. These GWs cannot be detected with ground based detectors like LIGO, however, they can be potentially detected with Pulsar Timing Array (PTA)[16], where the actual pulse time of arrival from a milisecond pulsar is compared to the predicted time of arrival[17]. They can also be detected with proposed Laser Interferometer Space Antenna (LISA)[18]. The frequency range for this type of GW fall between $10^{-9} - 10^{-6}$ Hz, as can be seen in Figure 2. Then we have GW with frequency range $10^{-4} - 1$ Hz. At the far right of the GW spectrum we have sources like compact binaries, supernovae and rotating neutron stars. The GW frequency is in the range of 10 Hz to 10 kHz and the detectors that are being used are terrestrial interferometers like LIGO.

There are four main classes of sources of GW that are expected to be detected by the terrestrial GW detectors like LIGO, Virgo, KAGRA. These are termed (i) Burst sources, (ii) Compact object coalescence sources, (iii) Continuous Wave sources, and (iv) Stochastic background sources.

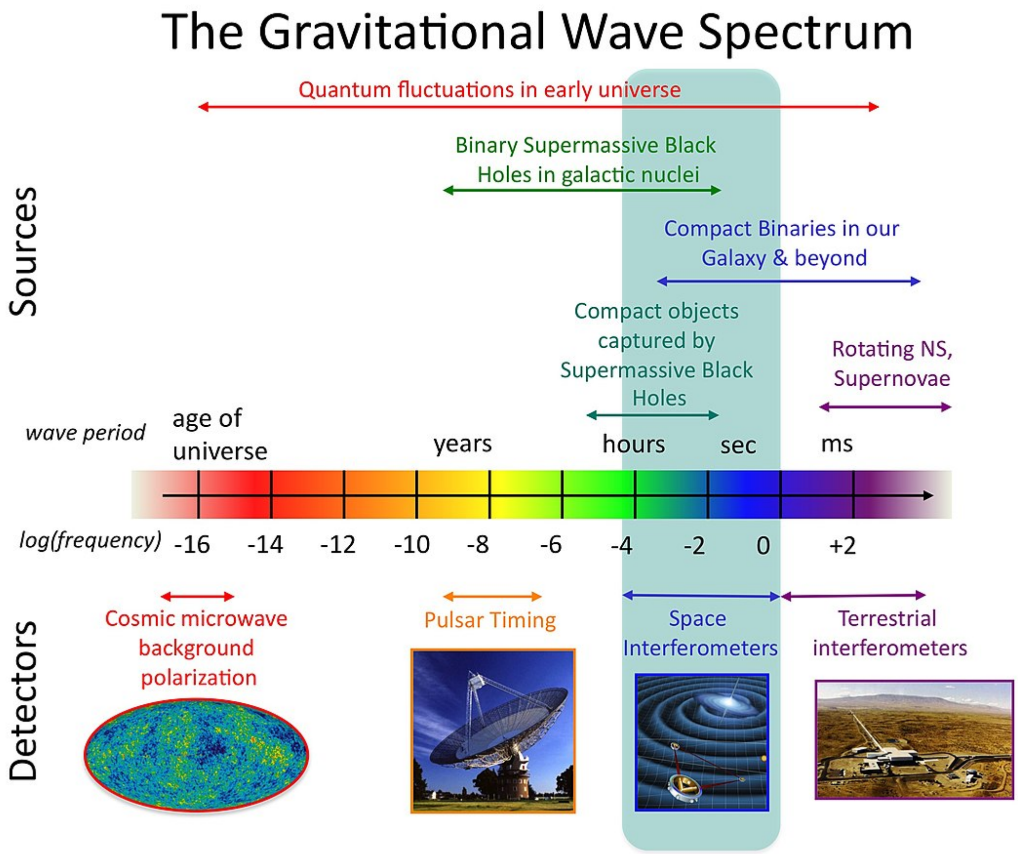

Figure 1.1.1: This figure shows the GW spectrum with sources and detectors across the frequency band. [Credit: NASA Goddard Space Flight Center]

1.1.1 Burst Sources

Gravitational Waves from the "burst" sources come from short-duration unmodeled sources. Core collapse supernovae (CCSN) or gamma ray bursts fall in this category. Figure 1.2.1 shows a CCSN as seen in the optical band in the Hubble Space Telescope. More detailed study of these sources will be the main topic of this thesis.

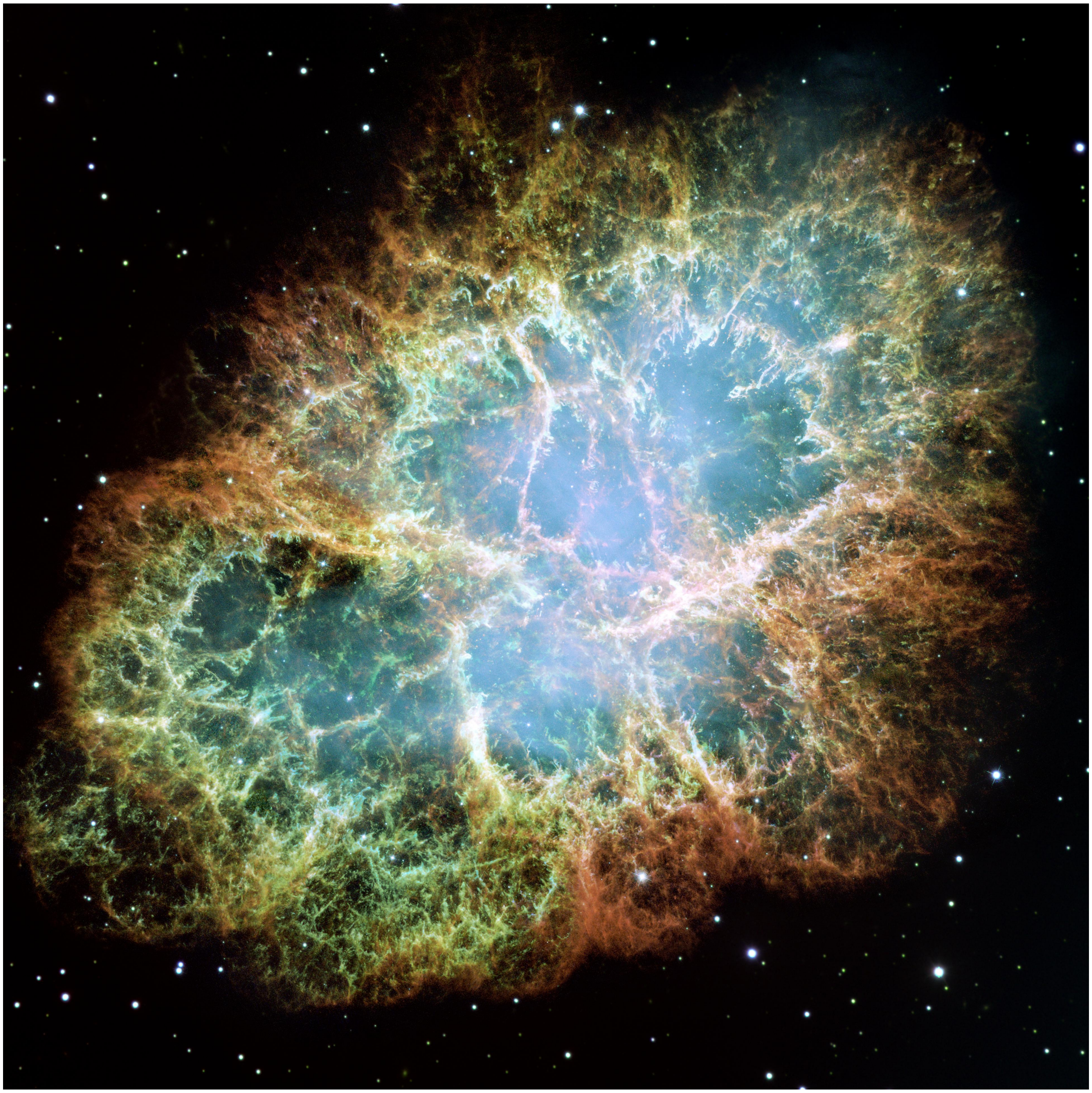

Figure 1.1.2: This figure shows the Crab Nebula obtained with the Hubble Space Telescope. The Crab Nebula is the leftover of a CCSN explosion which happened in the year 1054.

1.1.2 Compact Object Coalescence Sources

When two compact objects orbiting each other in binary systems merge at the end of their lifetime they emit GW. The two objects spiral into one another, losing energy and orbiting faster with time. That is why the frequency and amplitude of the GW increases until they merge. This is followed by the ringdown phase, where the new single object created from the merger settles down. Sources include binary black hole merger, binary neutron star merger or binary black hole and neutron star merger.

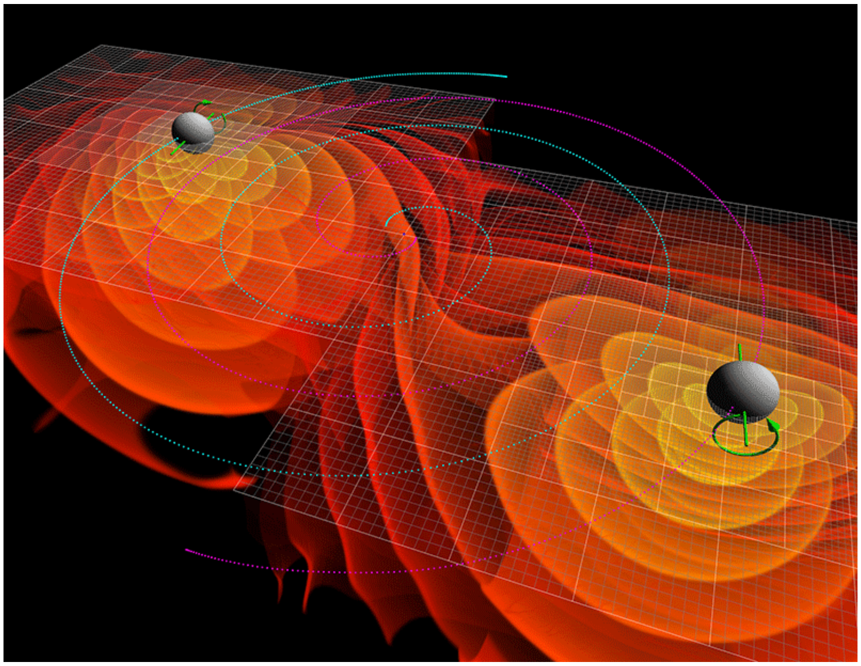

Figure 1.1.3: Numerical Simulation of GW from binary black hole merger [C. Henze/NASA Ames Research Center]

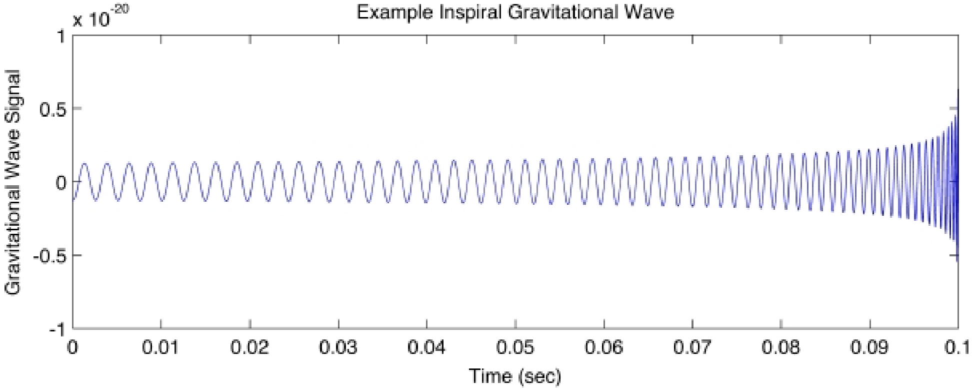

Figure 1.1.4: Inspiral Gravitational Wave [Image:A. Stuver/LIGO]

1.1.3 Continuous Wave Sources

As the name suggests, these GWs are continuous and periodic in nature. Frequencies of their sources are almost constant. Examples of the sources include binary star or blackhole systems long before merger and fast-spinning neutron star[19] with some kind of irregularity like non-axisymmetric spin or neutron star with a mountain. These GW signals are weak with a much longer duration as compared to binary mergers[20].

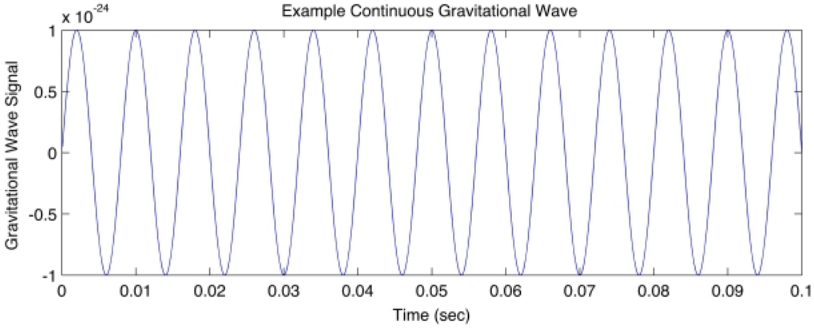

Figure 1.1.5: Continuous Gravitational Wave [Image:A. Stuver/LIGO]

1.1.4 Stochastic Background Sources

One important source of this type of GW is the inflation of the early universe[21] after big bang. This is known as stochastic gravitational wave background and is comparable to the CMB. Different physical processes like quantum fluctuations[22] of early universe, binary merger events all over the universe[23] in the past would be responsible for stochastic GWs. Stochastic background signals are same for all directions in the sky. Just like CMB, stochastic GW will be an important probe to the early universe and how it evolved to this stage, and hence will lead to a deeper understanding of the universe[22].

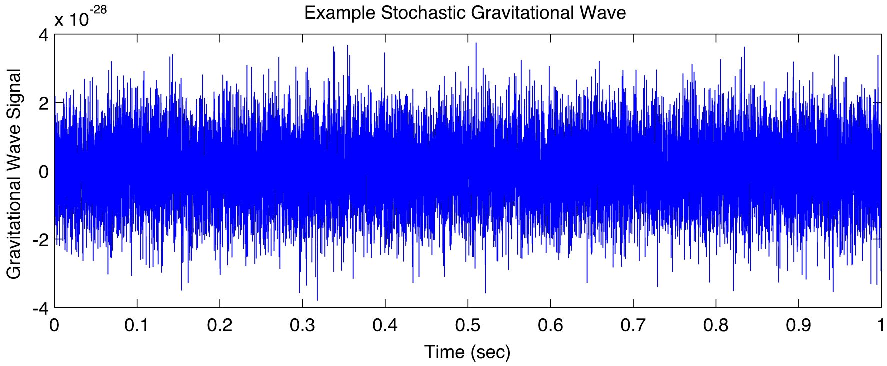

Figure 1.1.6: Stochastic GW background [Image:A. Stuver/LIGO]

1.2 GW Detectors

GW detectors use LASER interferometry to detect GW. Detectors consist of 2 arms each 4 km in length at right angle with each other, shaped like an L. A LASER beam is passed through the beam splitter at the intersection of the arms where it get divided into 2 beams, each travelling through the optical cavity of each arm, get reflected back by the mirrors at the end and recombines at the beam splitter. The recombined beam then hits the photodetector where it creates interference pattern. In the absence of GW lengths of both arms will be the same. As a result the reflected waves will be out of phase with each other at the beam splitter and there will be no pattern observed in the photodetector. In the presence of GW one of the arms will be stretch and another compressed, hence the LASER beams will not be completely out of phase. As a result, interference patterns will be observed in the photodetector.

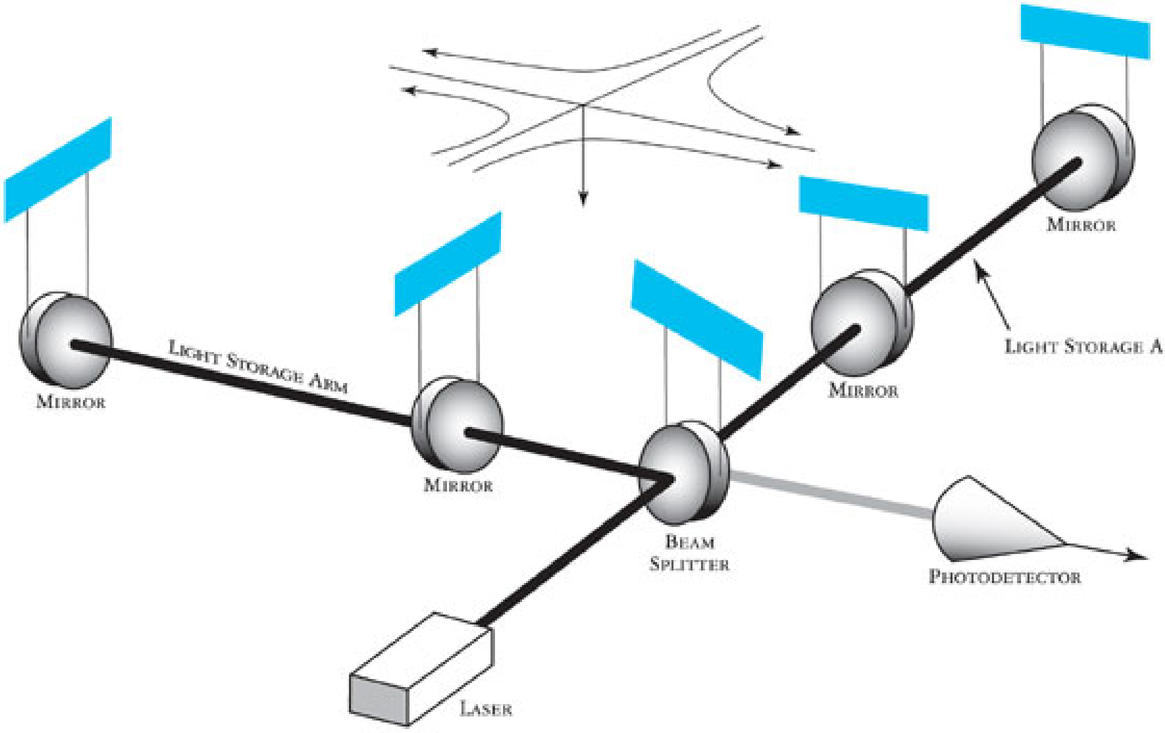

Figure 1.2.1: Gravitational Wave Detector [Image: LIGO]

1.3 Gravitational Waves from Core-Collapse Supernovae

Core-collapse supernova (CCSN) is one of the most violent and energetic events in the universe, which is responsible for short-duration GW burst[2]. CCSNe are responsible for the production of heavy elements and influencing the evolution of galaxies in terms of star formation and many more[1]. The core of a CCSN that is left can either be a neutron star or a blackhole. If it gives birth to a neutron star, the properties of the neutron star will be defined by the explosion mechanism of the supernova[1]. Therefore, it is very important to understand the explosion mechanism of CCSNe. So far all the supernovae have been observed electromagnetically(cite). A neutrino burst was also detected from the supernova SN 1987A[24][25]. The electromagnetic emission from CCSNe happens after the initial collapse, which contains most of the important information about the explosion mechanism. However, GW is generated at the moment of core bounce, carrying the important details of the explosion. Therefore, it is of enormous importance to detect GW from CCSN.

1.3.1 Supernova Explosion Mechanism

Not all stars become supernova. The condition that determines if a star will become a supernova at the end of its' lifetime is the mass of the progenitor which needs to have a mass of at least 12 solar mass while it is in the main sequence[26].

After the star leaves the main sequence stage, it starts burning He into C, C into O and so on. This process continues until it reaches Fe. No more nuclear fusion is taking place in the inert Fe core since it would take more energy to fuse Fe than will be gained from the nuclear fusion, as can be seen in the nuclear binding energy curve in figure 4. The Fe core keeps growing due to the shell burning of Si around the core until 1.4 solar mass, which is the Chandrasekhar limit[27]. It defines the upper limit of the mass a white dwarf can have. Until Chandrasekhar limit the core is resisting gravity with electron degeneracy pressure. The core temperature reaches 10^{10} K and density reaches 10^{10} g/cc. At this point electron capture[28] and photo disintegration[29] are taking place in the core as follows:

Electron capture:

$$e^- + p \to n + \nu_e$$

Photo-disintegration:

$$\gamma + {}^{56}Fe \to {}^{4}He + 4n$$

$$\gamma + {}^{4}He \to 2p^+ + 2n$$

Once the mass of the core exceeds Chandrasekhar limit electron degeneracy pressure[30] is no longer enough to resist gravity and hence the core starts to collapse. Due to electron capture neutrons and neutrinos are produced in the core. Also, because of the high temperature and density that comes from the gravitational energy, the high energy photons in the core cannot go far. As a result they disintegrate Fe nuclei, thus reversing years of nuclear fusion. Nuclear photo-disintegration produces more neutrons and protons. The protons react with electrons and produce more neutrons and neutrinos. Neutrinos escape the core taking out energy with it, which accelerates the collapse. As the core collapses the outer layers of the star also fall inwards. The core keeps collapsing until it reaches nuclear matter density. The collapse happens within a fraction of a second. Once it happens, neutron degeneracy pressure takes over and the collapse stops for a moment and the core bounces back. This core bounce gives rise to a shock wave which propagates towards the edge of the core. This is known as the initial shock.

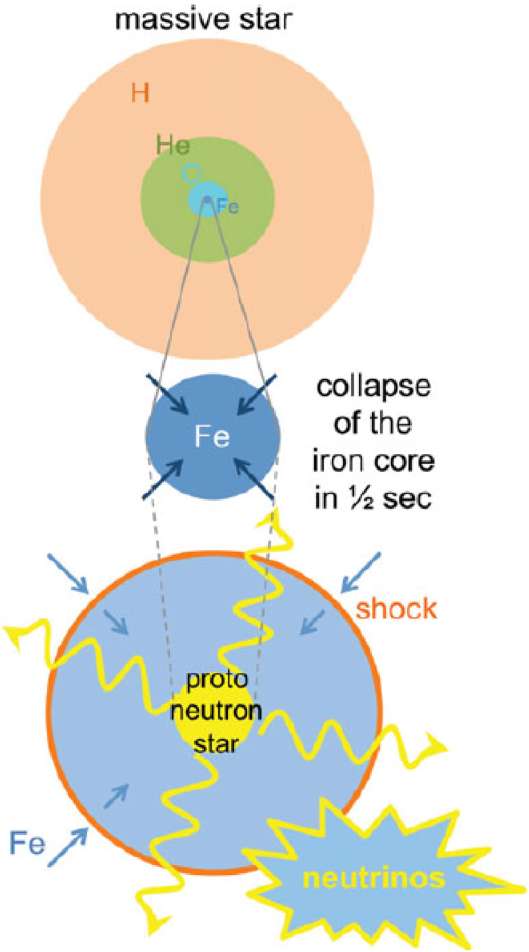

Figure 1.3.1: Neutrino-driven delayed explosion[1]

The core bounce is not elastic, since a large part of the gravitational energy is spent in the dissociation of Fe nuclei[31]. As a result the initial shock cannot reach the edge of the Fe core, leading to an unsuccessful explosion. This is because of the in-falling outer layers of the star that gives rise to a phenomenon called Standing Accretion Shock Instability (SASI)[32] that causes the shock to stall. However, the neutrinos that were produced in the core help revive the shock. Although most of the neutrinos are escaping from the core, due to the high density of the core a lot of neutrinos are trapped in the core. These neutrinos provide the energy to break the shock stagnation through an uneven convection, which makes the shock wave propagate outward and finally makes the star explode. The energy produced in a CCSN explosion is in the order of 10^{53} erg.

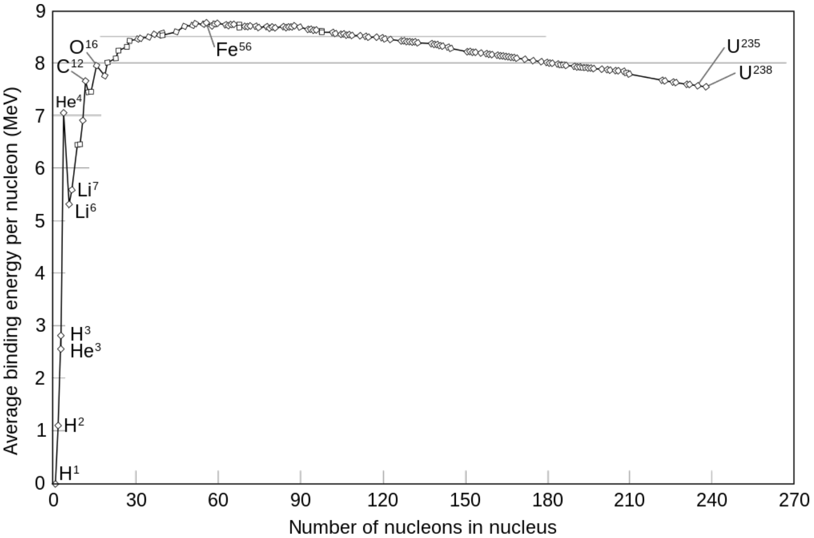

Figure 1.3.2: Binding energy curve per nucleon
Source: https://commons.wikimedia.org/wiki/File:Binding$_{e}nergy_{c}urve_{-c}ommon_{i}sotopes.svg$

1.3.2 Motivation

Core-collapse Supernova (CCSN) is one of the most anticipated sources of gravitational wave[33]. So far all the gravitational waves that have been detected [4][34] are from binary mergers with very well modeled signals. However, GW from CCSN are challenging to detect because of very low rate of occurrence (about 2 per century) [35] and the GW signals from them being weak and not well modeled. Moreover, the signals often mimic the detector glitches that are produced by noise. This makes it extremely important to distinguish between CCSN GW signals and detector glitches. In order to do so we used a Convolutional Neural Network (CNN). A comparison between GW waveform and detector glitch can be seen in Figure 10.

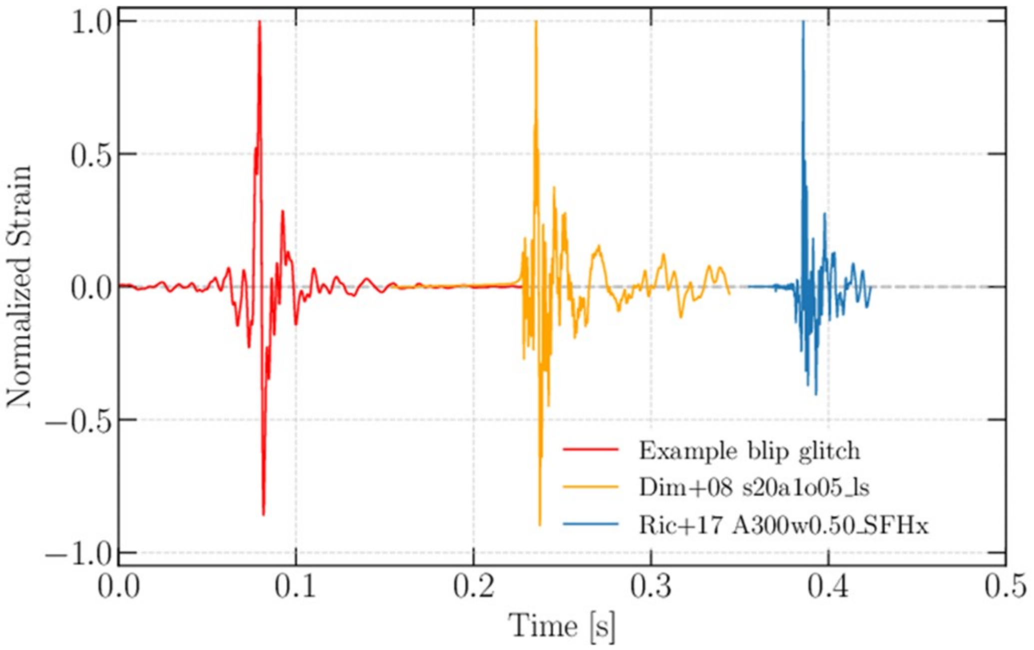

Figure 1.3.3: Comparison of detector glitch with GW waveform[2]

CHAPTER II

LITERATURE REVIEW

2.1 A review of recent work and CCSN models used in this study

Work done in the domain of GW from CCSN has two main directions. They are (i) theoretical simulation of CCSN waveforms and (ii) detection algorithms of GW from CCSN.

A large number of CCSN explosion scenarios has been discussed in the literature. Extensive information can be sought at [36]. The Powell-Muller and Morozova waveforms have been described in the previous section. Here we will also describe the waveforms that have been used in the CNN training. An excellent summary of properties of all available waveforms is given in Szczepanczyk [37].These different simulations vary in terms of input physics and produce very different time evolution signatures on the time-frequency plane.They also make varying predictions about the detectability of the CCSN signals by the current and future generation of detectors. Kuroda et. al. [38, 39] have presented general relativistic 3D simulations with different nuclear equations of state (EoS). A strong SASI development was observed for softer EoS. The evolution shows the first prompt convection phase, the sloshing SASI phase, and finally to the neutrino-driven convection phase. The study confirmed previously reported emissions originated from the PNS surface g-mode oscillation [40, 41]). The predicted waveforms are in the detection range of Advanced LIGO, Virgo Virgo and KAGRA [42] detectors. The peak frequency appears at 635, 671, and 681 Hz in order of the stiffness of nuclear EoS. Andresen et al.'s study make GW signal predictions from 3D multi-group neutrino hydrodynamics simulations of CCSN of progenitors with 11.2, 20 and 27 solar mass. It has been shown that the SASI activity produces a strong signal component below 250 Hz. Both convection- and SASI-dominated models show GW emission above 250 Hz.In the exploding 20 solar mass model, shock revival results in enhanced low-frequency emission due to a change of the preferred scale of the convective eddies in the PNS convection zone. Estimates suggest that second-generation detectors will not be able to see all events in inside the galaxy. However, the third-generation detectors could distinguish SASI and convection dominated models up to 10 kpc. Richers et al. [43] carried out more than 1800 2D rapidly rotating general relativistic hydrodynamic core collapse simulations. They predict that GW generated by axisymmetric rotating galactic CCSN, the bounce and early post-bounce phases can be detected by current generation of interferometers. They have examined the effects of the nuclear EoS on GWs from rotating CCSN in general-relativistic hydrodynamic simulations that cover 98 different rotation profiles and 18 different EoS. Their simulations show that the bounce GW signal is independent of the EoS and sensitive to the ratio of rotational to gravitational energy, and to the degree of differential rotation at high rotation rates. The relatively small differences in the GW characteristics and PNS oscillations induced by EoS variations indicate that a GW signal from CCSN may not be able to discern the EoS with current GW detectors. O'Connor and Ott [44] have performed spherically symmetric general relativistic simulations of CCSN and the post-bounce pre-explosion phase in 32 pre-supernova stellar models of solar metallicity with ZAMS masses of 12–120 solar mass. They have shown that the emitted neutrino luminosities and spectra follow systematic trends that are correlated with the compactness (mass to radius ratio) of the progenitor star's inner regions. Quantitative observational statements will require independent constraints on the EoS, the rotation rate and the neutrino oscillations. They conclude that large statistics of a galactic CCSN events may lead to robust conclusions on the inner structure of the progenitor star. O'Connor and Couch [45] use a 3D simulation with multidimensional neutrino transport, high-resolution hydrodynamics, and approximate general relativistic gravity with a 20 solar mass progenitor. While none of their 3D CCSN simulations explode within 500 ms after core bounce, it shows that large-scale aspherical motion help the shock expansion and bring the models closer to explosion. A strong SASI is seen to develop at later times. Both the progenitor asphericities and the SASI-induced transient shock expansion generate GW and neutrino signal modulations. Scheidegger et al. [46] have performed a set of 11 3D magnetohydrodynamical CCSN simulations to explore how GW signal depends on the progenitor initial conditions. Their study uses 15 solar mass progenitor in a general relativistic gravitational potential and a finite temperature nuclear EoS. They concluded that the non-rotating and the slowly rotating models show GW emission due to prompt convection that reveals details about the hydrodynamical state of the fluid inside the PNS. Their study shows that that the inclusion of deleptonization during the postbounce phase is important for the quantitative GW prediction.

Work done about the data analysis issues [47, 48, 49, 50, 51, 52, 53] associated with detection and parameter estimation of the CCSN signals has been summarized well in [54] using new search pipeline Multi-Layer Signals Enhancement integrated with cWB and CNN abbreviated as MuLaSECC developed by MUKHERJEE et al.[55]. Recently, Raza et al. [56] have studied the reconstruction of the GW signals from CCSN with Advanced LIGO-Virgo and the BayesWave algorithm [57]. They studied how well the BayesWave algorithm can recover the GW signal from CCSN models in simulated advanced detector noise. They show that BayesWave could reconstruct the signal in Advanced LIGO-Virgo for network signal-to-noise ratios (SNR) ≥ 30.Szczepanczyk and Zanolin [58] have investigated the detection probability and reconstruction of GW from CCSN using simulated data from future detectors between late 2020s and early 2030s. They found that the detection range and sky location would improve by a factor of 2 for the second-generation GW detectors. Their study indicated that, with a frequency cut-off of 250 Hz, high er frequencies were reconstructed more accurately. Srivastava et al. [59] have analyzed how to optimize the third-generation GW detector to maximize the range to detect CCSN. Based on 3D simulations, they showed that the detection range for these waveforms is limited to within our Galaxy even in the era of third-generation detectors. Abbott et. al. [47] explored GW bursts coincident with two CCSN within 15 Mpc observed optically in 2007 and 2011 using LIGO, Virgo and GEO600 [60] data. Another study [48] included the possibility of detection of GW from CCSN within a source distance of approximately 20 Mpc. Hayama et. al. [49] analyzed the circular polarization of GW using results from a 3D analysis of CCSN from a 15 solar mass non-rotating progenitor by using a coherent network of detectors viz, LIGO, Virgo and KAGRA. Their result demonstrated that the

SASI-induced accretion flows create a low-frequency modulation in the 100 and 200 Hz range. Gossan et. al. [50] have shown that GWs from CCSN within 5 Mpc are detectable, using realistic noise at the predicted sensitivity of the Advanced LIGO and Advanced Virgo detectors. Using phenomenological waveforms [51, 52], e.g. long-lived bar-mode instabilities and disk fragmentation instabilities, Gossan et. al.'s study, have been shown to detect emission from all considered long-lived bar-mode instability waveforms in the direction of M31 up to 0.77 Mpc with 2019 LIGO three detector network. Bizouard et. al. [53] have shown a parameter estimation approach for GW associated with PNS oscillation. The study involves a set of 1D CCSN simulations to model evolution of the PNS properties as a function of frequency of the dominant g-mode to infer about the time evolution with a combination of the mass and the radius of the PNS.

Machine learning (ML) techniques are becoming increasingly more useful in CCSN analysis. In a recent study, Antelis et al. [61] have used supervised ML to improve the performance GW search from CCSN using the cWB pipeline. The ML model differentiates noise from signal events by using a set of reconstruction parameters provided by cWB. The study has been performed by using LIGO O3 data and CCSN GW signals extracted from 3D simulations. The noise and signal reduction levels were examined in single (L1 and H1) detectors and two detector network (L1H1). The false alarm (FA) was reduced by a factor of more than 10. Iess et. al. [62] describe a search and classification procedure for GW emitted by CCSN, using CNN combined with Wavelet Detection Filter (WDF). A 1-D CNN was used with time series of GW strain data, and a 2-D CNN was used with time-frequency images. Their study indicated a classification accuracy of over 95% for both 1-D and 2-D CNN pipelines. Cavaglia et. al. [63] have studied an ML-based method to discriminate galactic GW CCSN signals from glitches with a reduction in FA and an improved detection statistic. Chan et. al. [64] also applied CNN to distinguish glitches from CCSN signals using simulated data. George et. al. [65] used a data set of twenty-two classes of glitches from LIGO's observation run, and demonstrated tan accuracy level above 98.8%. Lopez-Portilla [66] et. al. have used O2 data to demonstrate a newly developed Mini-Inception Resnet neural network using time-frequency images of simulated phenomenological signals. Astone et. al. [67] have analysed data from the LIGO, Virgo and KAGRA network with a CNN-based classification procedure of the time-frequency images using phenomenological waveforms [51, 52] in Gaussian noise.

R. Abbott et al. (2021)[68] did an all-sky targeted search for short duration GW burst. They injected 5 different simulated CCSN waveforms to determine the sensitivity of the search for galactic CCSN GW events. The efficiencies of the pipelines were found to be over 50% for two of them.

B. P. ABBOTT et al. (2020)[69] performed an optically targeted search with data from advanced detectors. Although no GW was detected, they were able to achieve better constraints of GW energy level for both low and high frequencies as compared to the previous search with first generation detectors. Detection efficiencies as a function of time for 5 different simulated GW waveforms were obtained, including extreme emission models.

CHAPTER III

METHODOLOGIES AND ANALYSIS PIPELINES

This part of the thesis will focus on the methods and search pipelines that were used to perform the analysis. The analysis pipeline used in this work is called the Multi-Layer Signal Enhancement with cWB and CNN or “MuLaSEcC” for short. MuLaSEcC integrates Machine Learning techniques with a network of Gravitational Wave detectors to detect and reconstruct core collapse supernova (CCSN) signals. At the same time, it reduces false alarm by using a trained convolutional neural network (CNN). In this chapter, the three main algorithms and pipelines are described.

3.1 Coherent Wave Burst

The coherent wave burst or cWB[70] is a pipeline that detects a broad range of gravitational-wave (GW) transients in a network of GW detectors. It uses network of detectors in a coherent manner and allows source localization. One important feature of cWB is that unlike traditional methods[71] that use coincidence to generate triggers from different detectors, it combines data from all detectors for analysis.

The data from the detectors is conditioned, whitened and have narrowband noise removed. The whitened data is analyzed in the time-frequency domain. Pixels whose energy is larger than a preset threshold are selected towards further analysis. The selected pixels from all detectors in the network are combined in a constrained likelihood function that depends on the (a) sky position of the source, (b) antenna patterns of the interferometers and (c) time delays between interferometer pairs. After maximizing the constrained likelihood, a candidate event is identified when a specific measure of signal coherence exceeds the threshold [72][73][74].

The cWB is based on C++ library, the WAT (Wavelet Analysis Tool) library, which are located within the CERN ROOT data-analysis framework [75][76]. Python scripts are used for the most crucial tasks of cWB low-latency analysis, e.g., the trigger uploading to the Gravitational-wave Candidate Event Database[8], which is a web service for early-warning information about candidate events. cWB is built with the Frame Library [9] to access data frames which has been the standard format for LIGO-Virgo data.

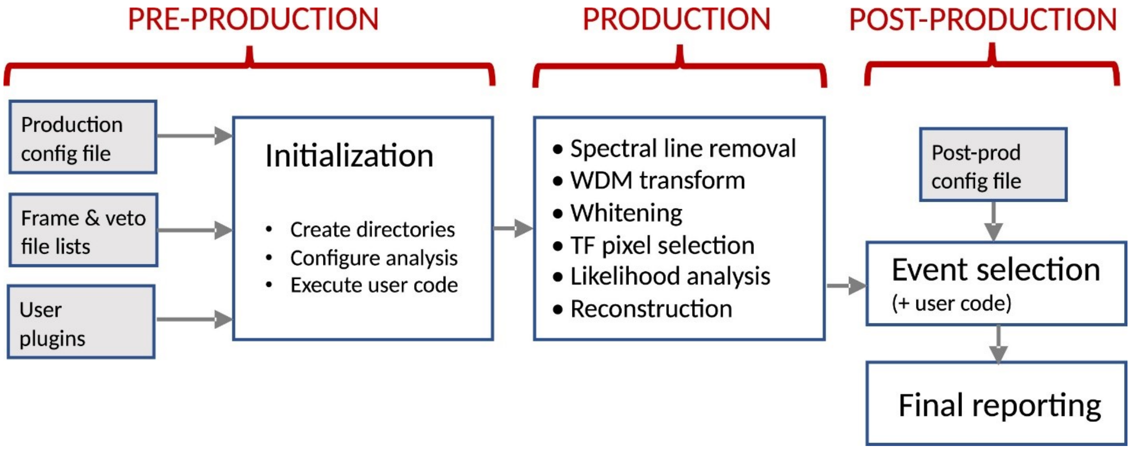

Figure 3.1.1: This figure shows the functionalities of the cWB pipeline. A description has been given in details in the text.

Figure 1 describes the functionalities of the cWB pipeline. The figure has been obtained from [1]. During PRE-PRODUCTION the pipeline reads (i) the production configuration file which specifies the parameters for the analysis, (ii) the frame files, which contain data, and (iii) veto files which mark time intervals of poor data quality. During PRODUCTION, the pipeline searches for triggers, and when one is found, it reconstructs the gravitational waveform. In the POST-PRODUCTION, events are selected according to conditions specified, and finally, the pipeline outputs a report in the form of a properly formatted web page.

3.1.1 cWB Algorithm

The algorithm is based on a time–frequency analysis with the Wilson–Daubechies–Meyer wavelets[77] to identify unmodeled signal waveforms. cWB is used to analyze observation data from the LIGO-Virgo detectors. There are 4 steps in the data analysis using cWB:

(i) Wavelet Transform

Wavelet transform[78] is the first step of cWB, where Discrete Wavelet Transform (DWT)[79, 80] is performed on the time series. It transforms the data from time domain to wavelet domain, which gives the time-frequency (TF) plot of the data. In order to account for frequency and time resolution, a range of scales are used in DWT.

(ii) Linear Prediction Error Filter

A filter is applied to the data to whiten, which means removing narrow band noise due to different components of the detector. The filter is called Linear Prediction Error (LPE) filter[81] and it is constructed after performing wavelet decomposition to the data to remove the lines.

As the filter is applied after decomposing time series data into wavelet domain, the time series is reconstructed after the filtering is done.

(iii) Time Shift Filter

GWs have finite speed, that is the speed of light. Therefore, there is a delay between the time of arrival of GW signal to the detectors that needs to be accounted for when likelihood is being calculated.

For likelihood analysis data streams from different detectors are shifted before taking the inner products. A time delay filter is applied for shifting the data stream in wavelet domain, due to the colored detector noise.

(iv) Trigger Generation

cWB uses likelihood statistic which uses both excess power statistic[82] and CorrPower algorithm[83] to generate events or triggers.

cWB calculates likelihood functional after time-frequency (TF) decomposition of the data segment. Likelihood functional is maximized over the source coordinates which gives the maximum likelihood statistic. The maximum likelihood is a function of time and frequency, which, when summed over detectors in the network and time-frequency indices, gives a time-frequency map of the data. Coherent trigger can be identified by finding those pixels in the TF map which are above a threshold.

3.2 Machine Learning

Machine Learning (ML) is being used in wide range of areas and GW is no exception. ML is particularly important in the detection of short-duration burst signals, which we have seen previously. Convolutional Neural Network (CNN)[84] is an ML algorithm that makes a substantial part of this thesis. CNN has been used here in order to extract features from the time-frequency plots (spectrograms) of GW waveforms.

Convolutional Neural Network

The Convolutional Neural Network or CNN [85, 86, 87, 88, 89] has been used in a variety of classification problems. CNN is very fast and effective in image classification [15, 16]. The image classification is the process of taking an input image and giving an output or a probability that the input belongs to a particular class of objects. In this work, the time-frequency plots of glitches or signals have been used [17]. A CNN works by extracting features from images that are learned while the network trains. Hidden layers of a CNN increase the complexity of the learned features. A CNN follows the sequential steps described below in a repetitive manner until a well-trained network is obtained. (i) starts with time-frequency input image (ii) creates a feature map by applying filters to the input time-frequency image (iii) applies a ReLU (rectilinear linear unit) function to increase non-linearity (iv) applies a pooling layer to each feature map and creates one single vector of pooled images (v) inputs the vector into a fully connected artificial neural network (ANN) (vi) processes the features through the network. The final fully connected layer provides the “voting” of the classes (vii) trains through forward propagation and backpropagation for many, many epochs.

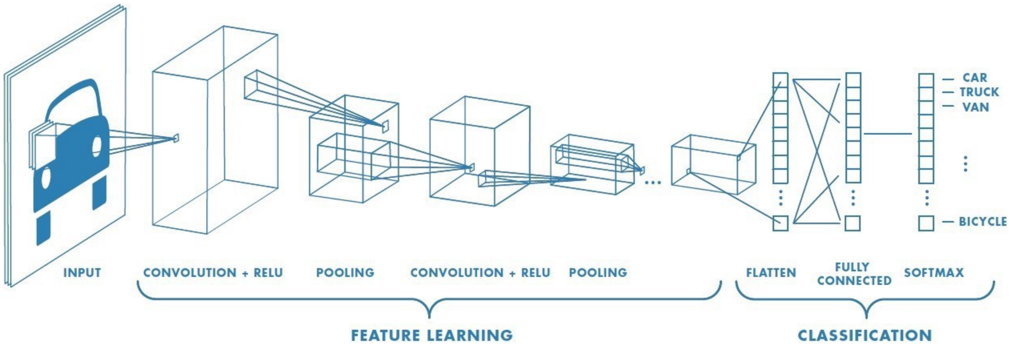

Figure 3.2.1: A schematic diagram of the CNN by using a cartoon image of a car. This image has been taken from https://towardsdatascience.com/a-comprehensive-guide-to-convolutional-neural-networks-the-eli5-way-3bd2b1164a53

The figure displays the steps (i) to (vii) in the above text. A CNN convolves learned features with input data and uses 2D convolutional layers, making it suitable for processing 2D images. CNN has an input layer, and output layer, and hidden layers. The hidden layers usually consist of convolutional layers that pass information to following layers, ReLU layers, pooling layers that combine the outputs of clusters of neurons into a single neuron, and fully connected layers that connect every neuron in one layer to the next level.

The main characteristic of CNN is the convolutional operation, as the name suggests. CNN has particularly high performance in image classification[90]. CNN has 4 layers: (i) Convolution, (ii) Pooling, (iii) Activation Layer, (iV) Fully Connected Layer, (v) Classification. These steps are described below in details:

(i) Convolution

The image is broken down into pixels, where each pixel contains a value or number. The image is essentially transformed into a matrix. A filter or kernel which is a smaller dimensional matrix is applied to the image for convolution. The filter convolves with the elements of the matrix, which is an element-wise multiplication. The filter slides across the image with a specified stride or step size and keeps multiplying with the elements of the image. The resultant matrix obtained at the end of convolution is called feature map.

Besides stride another important parameter in the convolution layer is padding. Padding, which is adding extra rows and columns around the image is done in the corners or borders of the image to prevent information loss. Zero-padding is a popular and useful choice in many cases.

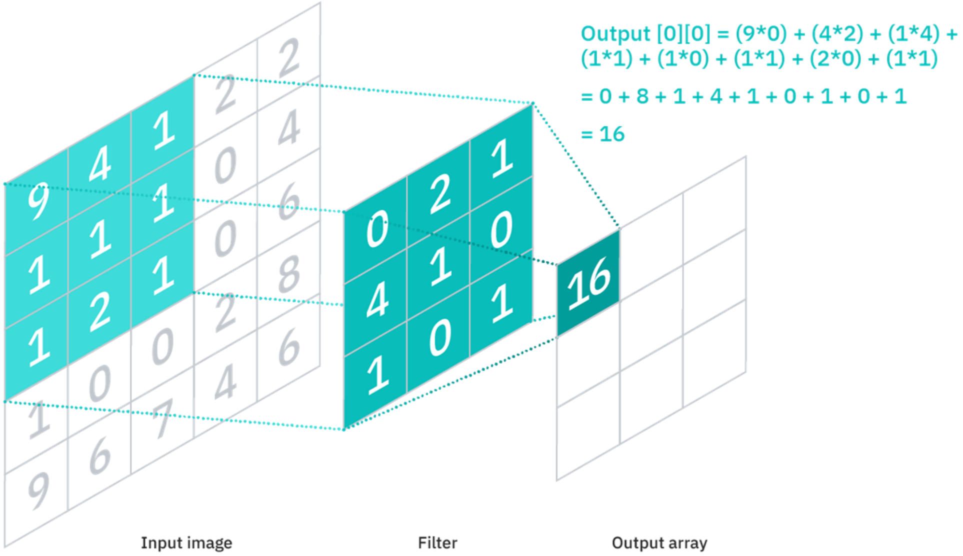

Figure 3.2.2: Convolution Operation
Source: https://www.ibm.com/cloud/learn/convolutional-neural-networks

(ii) Pooling

Pooling layer is where the feature map is down sampled. There are 2 types of pooling - max pooling and average pooling. In max pooling for each of the convolution operation only the maximum value from each of the smaller resultant matrices are selected. Similarly in average pooling the average of all the values of each of the matrices are selected. AVerage pooling was used in the CNN that was used in this thesis.

(iii) Activation Layer

After the pooling and flattening, the outputs are passed to activation layer, which is a mathematical function known as activation function. The activation function prepares outputs from pooling layer to pass them to the fully connected layer. There are different types of activation functions like sigmoid, ReLU and so on. We used Rectified Linear Unit (ReLU) as activation functio in our CNN. For high and positive values, ReLU assigns a number close to 1 and for negative values it assigns 0.

(iv) Fully Connected Layer

At the end of pooling layer the image is flattened, which means an $n \times n$ matrix will be converted into $n^2 \times 1$ matrix. This flattened matrix is passed to the fully connected layer with a specified number of nodes or 'neurons' with different weights assigned to each of the outputs from the pooling layer.

Fully connected layer is also known as dense layer. There can be multiple dense layers with specified number of neurons.

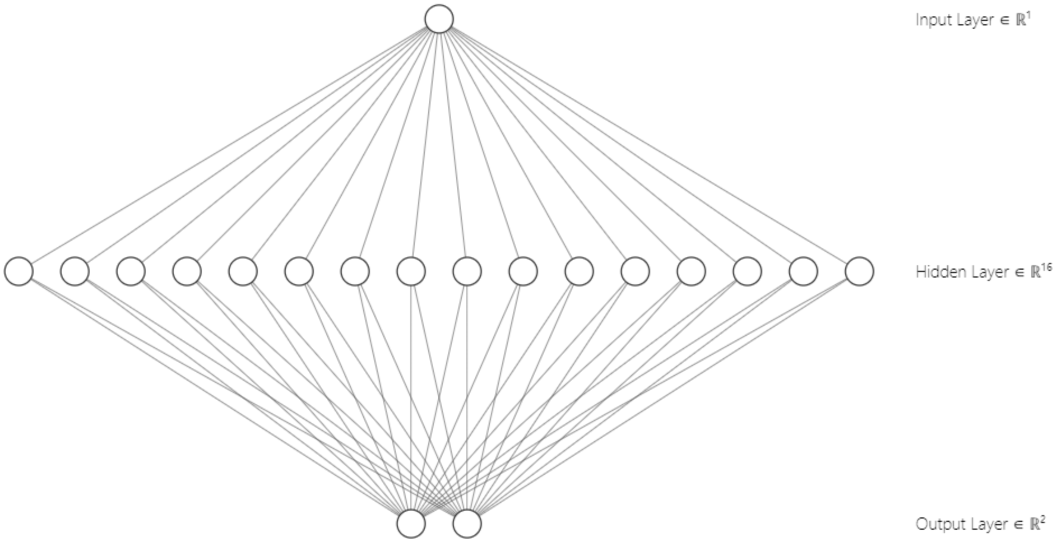

Figure 3.2.3: Fully Connected Layer

(v) Classification Layer

This is where the classification occurs, for example whether the input image is of a cat or a dog. Input of the classification layer is the output from the dense layer. Classification layer uses a function called softmax as classifier, which is an exponential function that assigns probabilities to the outputs from the dense layer. For example, 90% probability that the image is of a dog and 10% probability that it is of a cat.

3.3 Multi-Layer Signal Enhancement with cWB and CNN

Multi-Layer Signal Enhancement with cWB and CNN or MuLaSEcC is the main pipeline used for this analysis. The pipeline is based on a signal estimation algorithm called MuLaSE [18] that works in conjunction with a network analysis like the cWB and with an integrated CNN [17]. MuLaSE has been described in great detail in [18]. It is a non-parametric method of estimation of a stochastic signal in noisy data by a two-step noise reduction technique that involved a decision directed approach and a harmonic regeneration technique at the end to compensate for any distortions that may have been caused in the process. MuLaSEcC is a multi-modular pipeline as demonstrated in figure 3. In the red box, the CNN training takes place. Data from the LH network is read, followed by data conditioning to whiten the data, bandpass to remove the low frequency seismic noise and the high frequency shot noise and remove the narrowband noise or “lines”. The conditioned data then performs a background run where all possible noise signals are generated, converted to their time-frequency representation and used for training the CNN. Simultaneously, CCSN signals are injected and passed through the network pipeline. The triggers detected at the output are converted to their time-frequency representation and used for training the CNN. In the middle blue box, MuLaSEcC runs in the detection mode. Here, the signals detected at the output are then subjected to the CNN classifier to discriminate between the actual CCSN signals and the noise. The selected signals are then processed further to study the reconstruction of the signal in time domain, frequency domain and in the time-frequency plane. In the right-most green box, another type of analysis takes place. Here the CCSN waveforms are injected at various distances across the galaxy. At the end of the analysis, an efficiency curve is produced to show the detection probabilities as a function of distance.

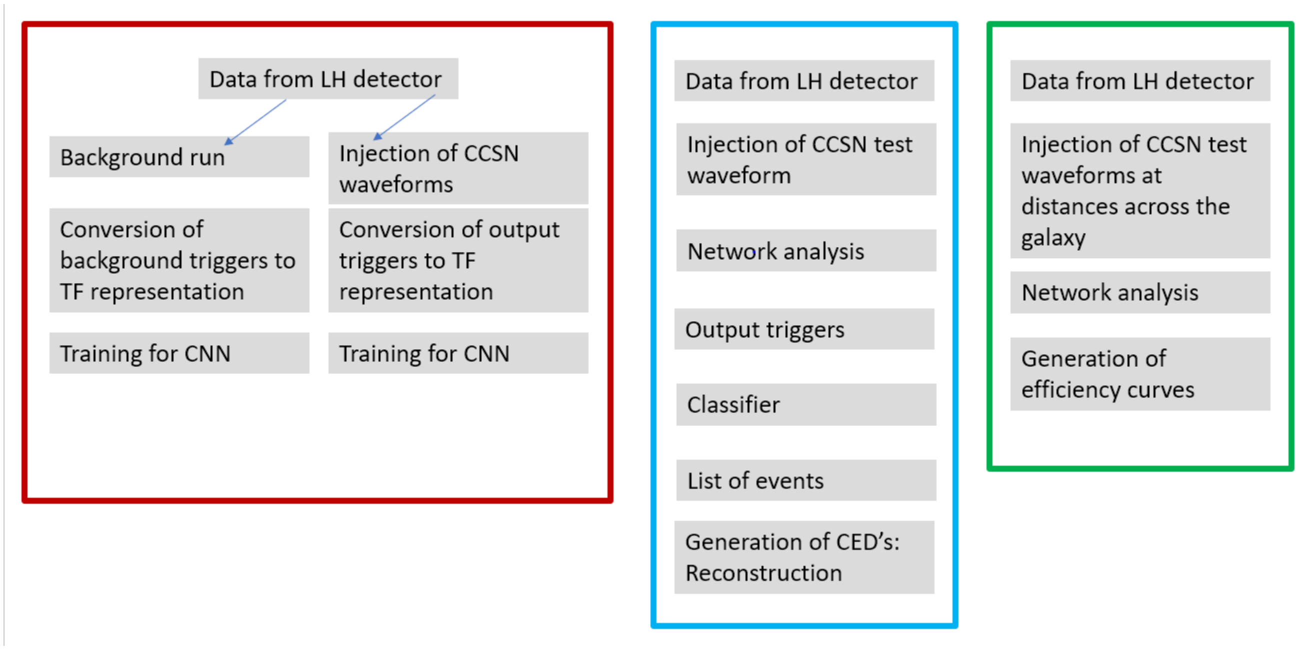

Figure 3.3.1: The MuLaSEcC pipeline in modular form. See the text in this section for detailed description of each module

3.3.1 MuLaSEcC Algorithm

Data from GW detectors like LIGO are noisy. The MuLaSEcC algorithm starts with the assumptiom that both signal and noise are Wide Sense Stationary (WSS) with additive noise model. It is also assumed that the signal and noise have no correlation.

The entire data is divided into smaller segments and the target is to find the estimate of the signal if there is any in each of those segments by applying a spectral gain function, which is a function of two parameters that are defined in the corresponding paper - a posteriori snr and a priori snr, which are not in a Bayesian sense. They are defined as follows -

$$snr_{post}(p,k) = \frac{|X(p,k)|^2}{P_{NN}(p,k)}$$

$$snr_{priori}(p,k) = \frac{P_{SS}(p,k)}{P_{NN}(p,k)}$$

where $P_{NN}(p,k)$ = Noise PSD,

$P_{SS}(p,k)$ = Signal PSD and

$X(p,k)$ = DFT coefficients of noisy data

The noise power spectral density (PSD) is estimated using the minimum power statistic method[91].

The spectral gain function in this case is Wiener filter[92]. A finite impulse response (FIR) filter is applied to the noisy data and the mean square error (MSE) equation is obtained for the estimated signal and the actual signal. Minimization of Mean Square Estimation (MMSE) error is used in order to find the optimal values of filter coefficients.

One important concept that was used in this method is the Decision Directed (DD) approach. In DD approach the data is divided into frames and the estimated signal amplitudes of each frame is combined with the one in the previous frame. The reason being that the entire signal may not be contained in a single frame, but rather in more than one frame.

To overcome the overestimation problem a two step noise reduction (TSNR) technique is used. In this approach the DD algorithm is not only applied to the current and previous frame, but also to the next frame.

3.4 Detection Statistic

The detection statistic in this analysis was RHO, which is a measure of signal strength. It depends on the SNR of the signal and the Network Correlation Coefficient (cc). The relationship is:

$$\text{RHO} \sim \sqrt{SNR \times cc}$$

3.4.1 Receiver Operating Characteristic Generation

Receiver Operating Characteristic (ROC) curves were generated by putting thresholds on RHO. For False Alarm Probability (FAP) the number of noise triggers above certain values of RHO were calculated. For Detection Probability (DP) the same were done using detected signals that were injected at different distances. For both FAP and DP RHO values go from minimum to maximum at a specified step.

CHAPTER IV

RESULTS

4.1 Overview of the pipeline and results

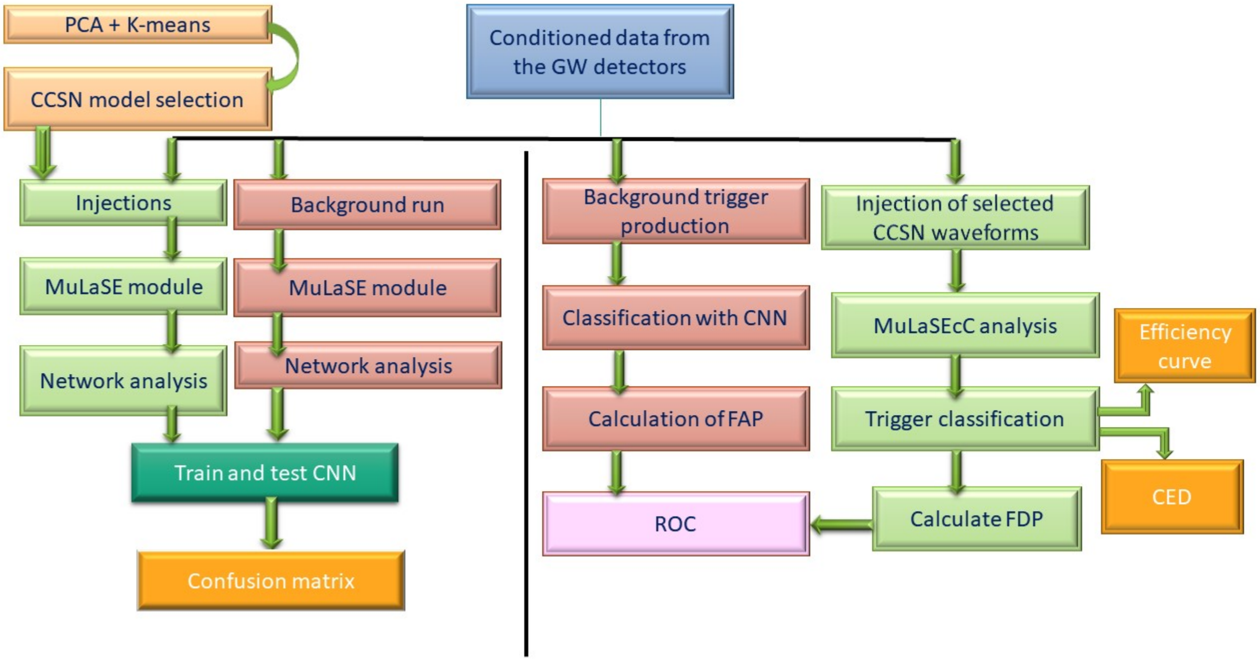

Figure 4.1.1: This figure provides a general overview of all the steps that were used for this analysis. The details of these steps are described in the following sections.

4.2 Data Selection

In our analysis we used data from LIGO's 3rd observation run (O3), specifically from the O3b portion of the data. In order to train the CNN model 1 month of data was used, namely from GPS 1266332442 seconds to 1268751642 seconds. The justification of using this data segment is that during this time both detectors of LIGO (L1, H1) were in their peak sensitivity, which can be seen from the figure below. For the same reason we chose the test data segment to be from 1263913242 to 1264258842. A 2 detector network was used for this analysis (Hanford-Livingston).

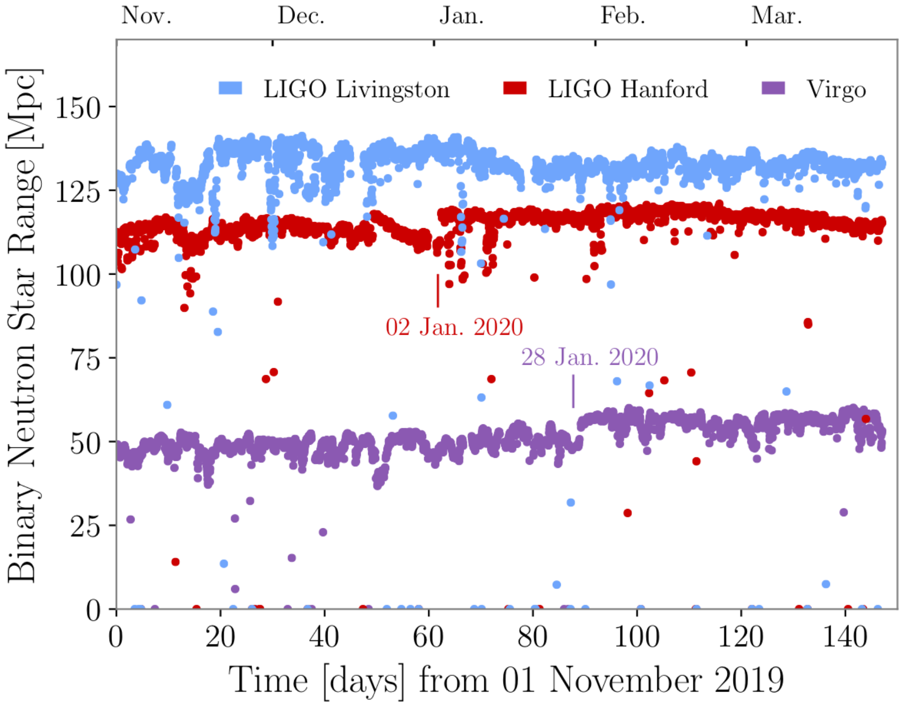

Figure 4.2.1: Sensitivity of the detectors in LVK network[11]. The y-axis represents the sensitivity of 3 detectors LIGO Hanford, LIGO Livingston and Virgo in terms of detection range of Binary Neutron Star mergers.

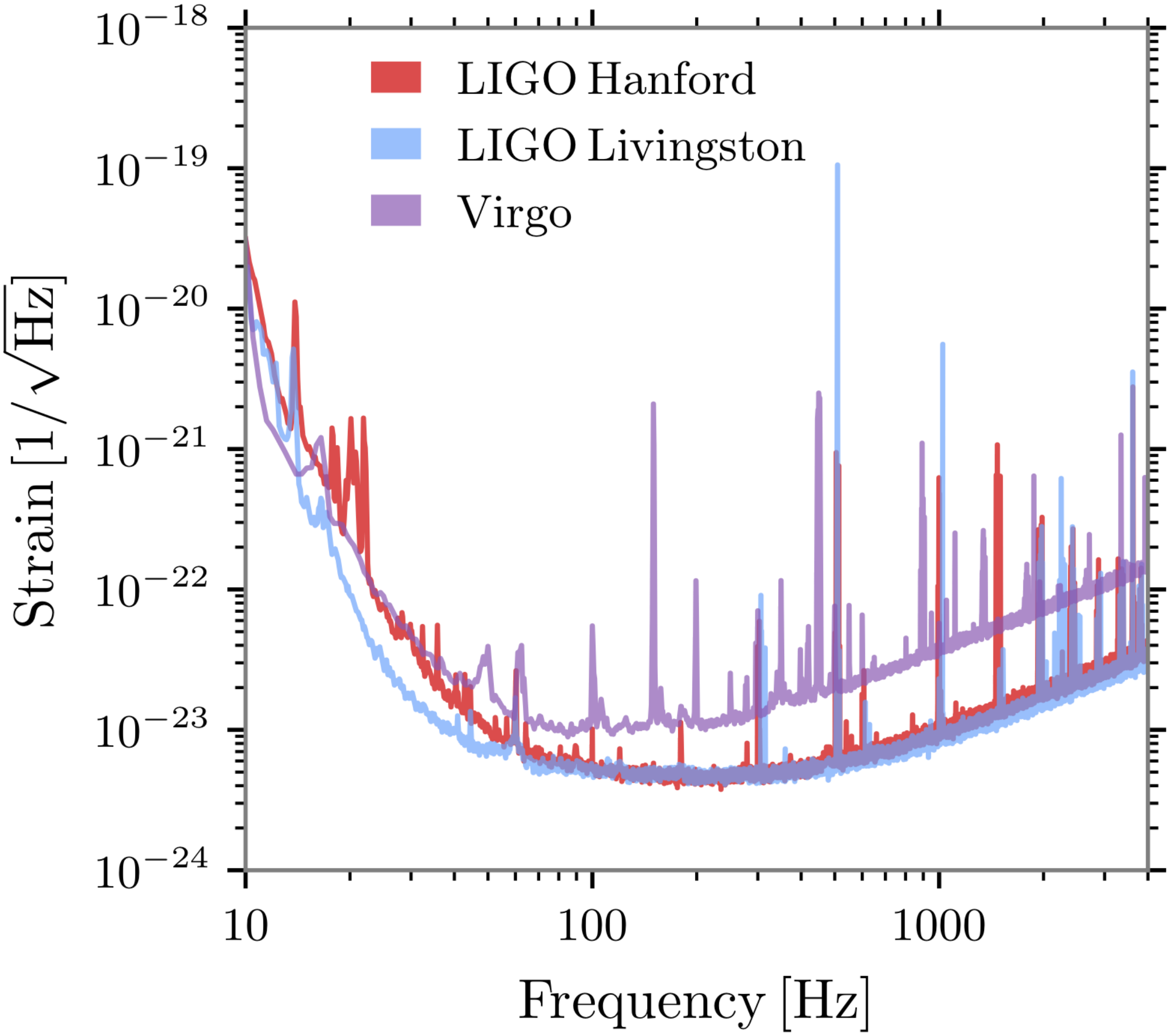

Figure 4.2.2: This is the Power Spectral Density of the data from the LIGO Livingston (L1), LIGO Hanford (H1) and Virgo detectors. The plot depicts strain in $1/\sqrt{Hz}$. From the graph, LIGO Hanfod and Livingston have more sensitivity than Virgo. [11]

4.3 Background

GW detectors mostly pick up noise from various sources. These noise are sources of false alarms in the detection pipeline, which means that they should be estimated and cut down as much as possible. Background run is the type of analysis we do to find the number of triggers produced by noise. A stretch of data is selected using the method mentioned in the Data selection section and analysis is done with different number of lags including zero lag. Background run provides us with important information like the number of noise triggers, their strength in terms of Signal to Noise Ratio (SNR), False Alarm Rate (FAR) and so on.

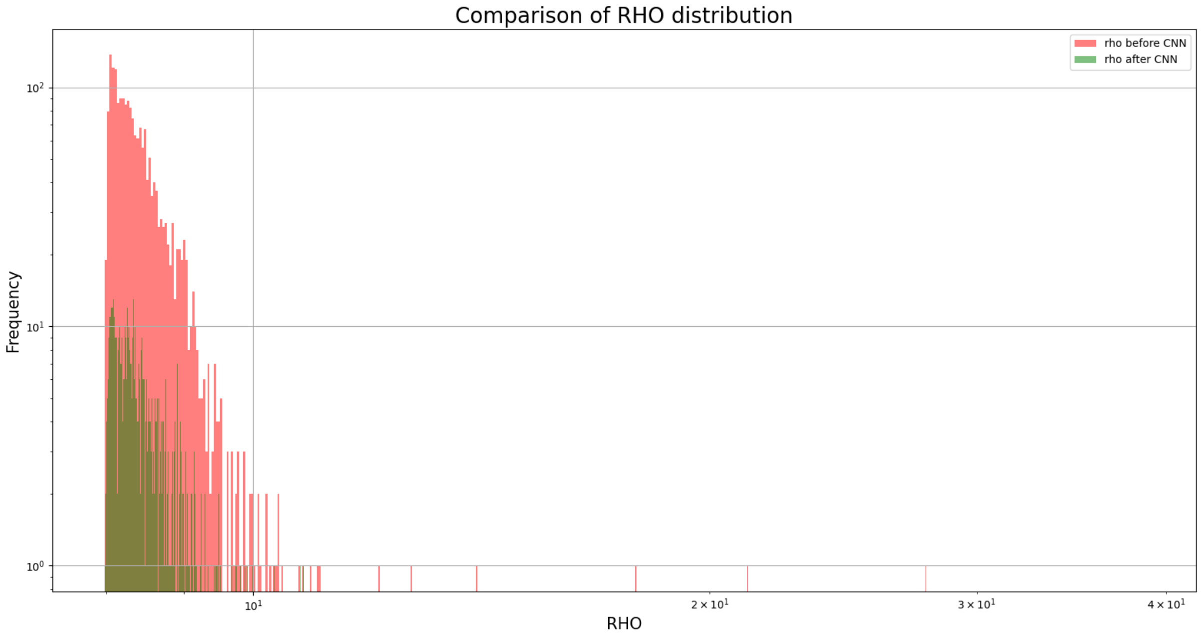

Figure 4.3.1: Distribution of RHO values of noise triggers before and after applying CNN classifier. CNN was able to cut down a substantial portion of noise triggers including higher RHO values.

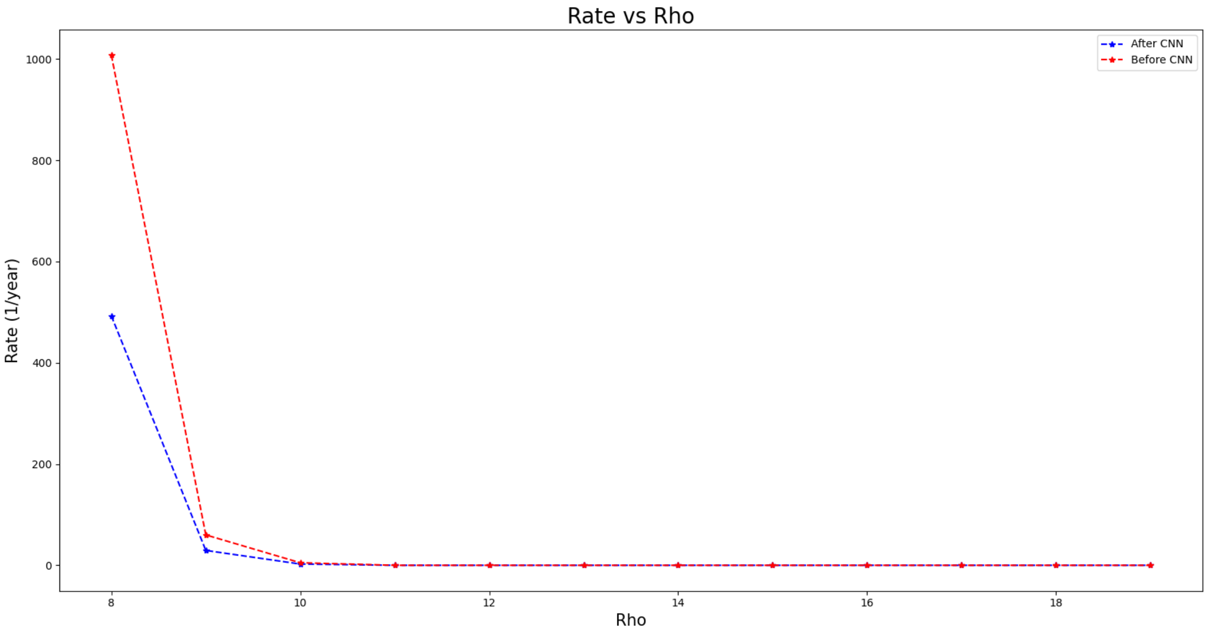

Figure 4.3.2: This figure shows the plot of Rate vs RHO. As the threshold for RHO goes up, False Alarm Rate per year goes down.

4.4 Injection

In this type of analysis simulated CCSN signals are added to the time series data from LIGO at a specified interval for different distances. Then we analyze the noisy data using our pipeline and try to recover the injected signals.

4.4.1 CNN Training

We trained our CNN with time-frequency images of 9 different types of simulated Core-Collapse Supernova GW waveforms and noise triggers. These waveforms were chosen from a multi-variate analysis of all the CCSN waveforms which are similar in nature.

Table 4.1: List of 9 simulated CCSN GW waveforms used for CNN training with important properties

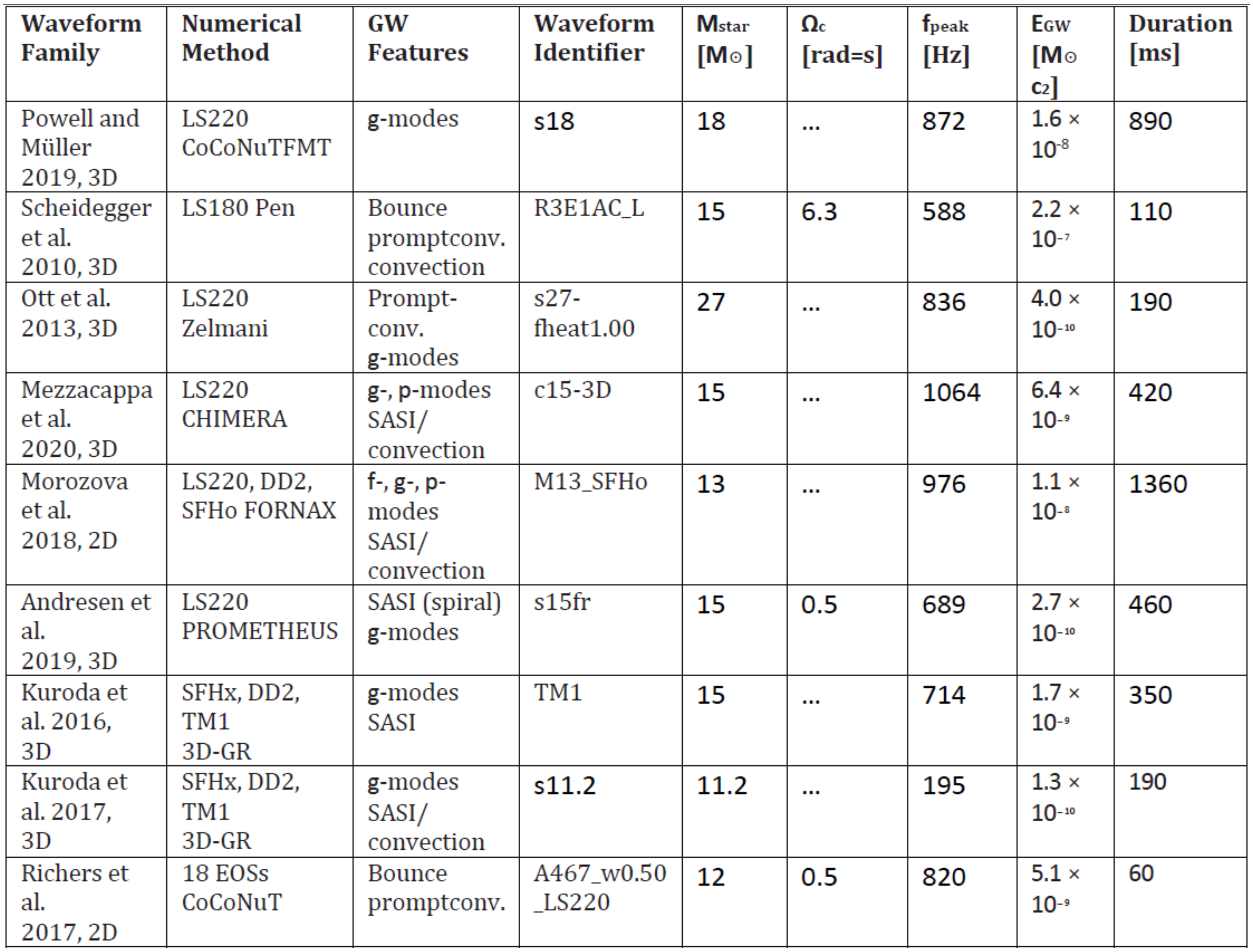

Waveform Family	Numerical Method	GW Features	Waveform Identifier	M_{star} [$M_\odot$]	Ω_c [rad=s]	f_{peak} [Hz]	E_{GW} [$M_\odot$ c^2]	Duration [ms]
Powell and Müller 2019, 3D	LS220 CoCoNuTFMT	g-modes	s18	18	...	872	1.6×10^{-8}	890
Scheidegger et al. 2010, 3D	LS180 Pen	Bounce promptconv. convection	R3E1AC_L	15	6.3	588	2.2×10^{-7}	110
Ott et al. 2013, 3D	LS220 Zelmani	Prompt-conv. g-modes	s27-fheat1.00	27	...	836	4.0×10^{-10}	190
Mezzacappa et al. 2020, 3D	LS220 CHIMERA	g-, p-modes SASI/ convection	c15-3D	15	...	1064	6.4×10^{-9}	420
Morozova et al. 2018, 2D	LS220, DD2, SFHo FORNAX	f-, g-, p-modes SASI/ convection	M13_SFHo	13	...	976	1.1×10^{-8}	1360
Andresen et al. 2019, 3D	LS220 PROMETHEUS	SASI (spiral) g-modes	s15fr	15	0.5	689	2.7×10^{-10}	460
Kuroda et al. 2016, 3D	SFHx, DD2, TM1 3D-GR	g-modes SASI	TM1	15	...	714	1.7×10^{-9}	350
Kuroda et al. 2017, 3D	SFHx, DD2, TM1 3D-GR	g-modes SASI/ convection	s11.2	11.2	...	195	1.3×10^{-10}	190
Richers et al. 2017, 2D	18 EOSs CoCoNuT	Bounce promptconv.	A467_w0.50 _LS220	12	0.5	820	5.1×10^{-9}	60

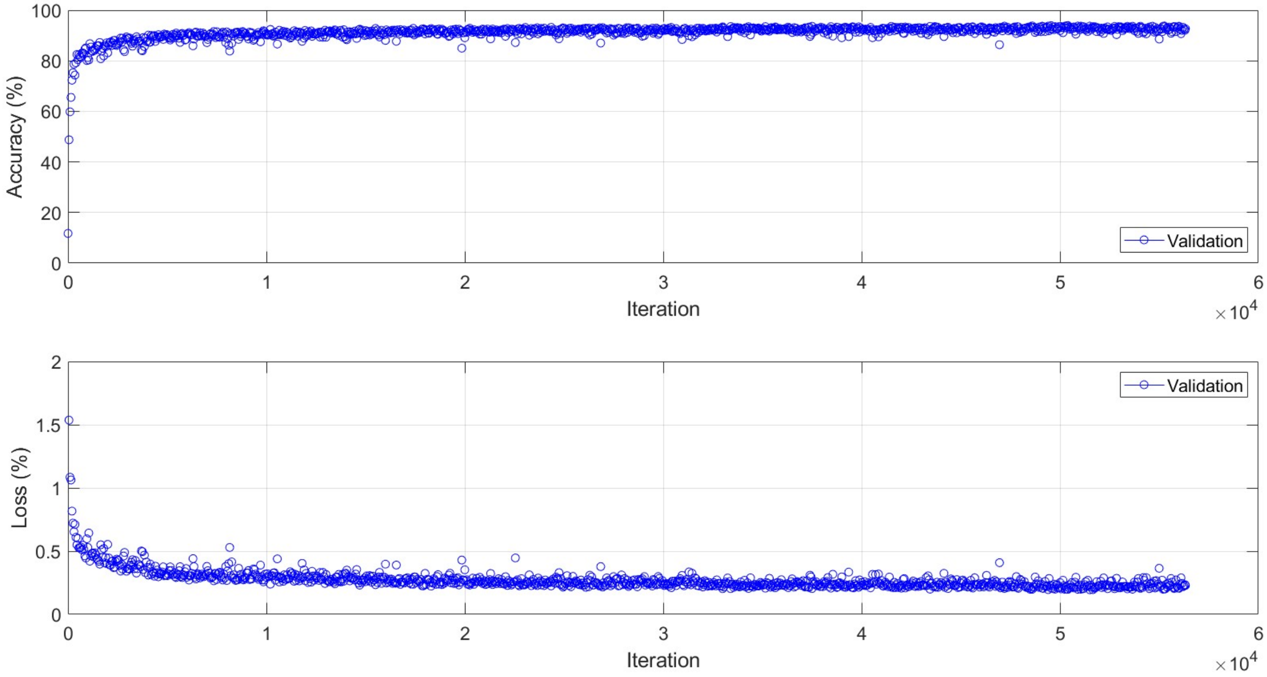

Figure 4.4.1: Accuracy and Loss plots of the first CNN with normalized data

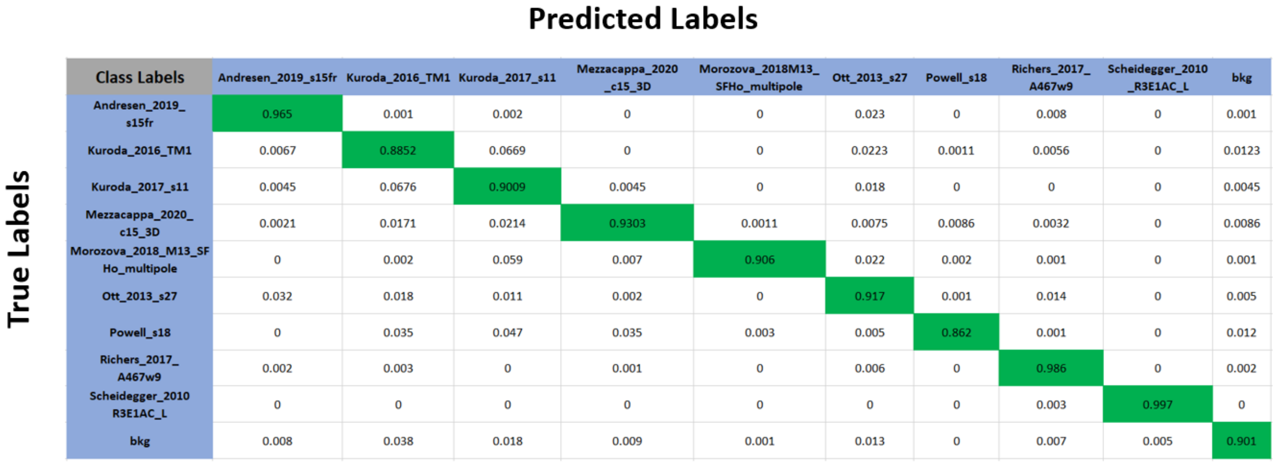

Predicted Labels

True Labels

Class Labels	Andresen_2019_s15fr	Kuroda_2016_TM1	Kuroda_2017_s11	Mezzacappa_2020_c15_3D	Morozova_2018M13_SFHo_multipole	Ott_2013_s27	Powell_s18	Richers_2017_A467w9	Scheidegger_2010_R3E1AC_L	bkg
Andresen_2019_s15fr	0.965	0.001	0.002	0	0	0.023	0	0.008	0	0.001
Kuroda_2016_TM1	0.0067	0.8852	0.0669	0	0	0.0223	0.0011	0.0056	0	0.0123
Kuroda_2017_s11	0.0045	0.0676	0.9009	0.0045	0	0.018	0	0	0	0.0045
Mezzacappa_2020_c15_3D	0.0021	0.0171	0.0214	0.9303	0.0011	0.0075	0.0086	0.0032	0	0.0086
Morozova_2018_M13_SFHo_multipole	0	0.002	0.059	0.007	0.906	0.022	0.002	0.001	0	0.001
Ott_2013_s27	0.032	0.018	0.011	0.002	0	0.917	0.001	0.014	0	0.005
Powell_s18	0	0.035	0.047	0.035	0.003	0.005	0.862	0.001	0	0.012
Richers_2017_A467w9	0.002	0.003	0	0.001	0	0.006	0	0.986	0	0.002
Scheidegger_2010 R3E1AC_L	0	0	0	0	0	0	0	0.003	0.997	0
bkg	0.008	0.038	0.018	0.009	0.001	0.013	0	0.007	0.005	0.901

Figure 4.4.2: Confusion Matrix of trained Convolutional Neural Network (CNN)

4.4.2 Testing the Trained CNN

In order to analyze our trained CNN we used 4 waveforms - Powell and Muller s18, Kuroda 2016 TM1, Mezzacappa c15 3D, which were part of the training set and Morozova M19, which was not part of the training set.

4.4.3 Powell and Muller s18

Powell and Muller s18 [93] is a 3D general relativistic simulation of CCSN GW signal. It is a non-rotating 18 solar mass progenitor with peak frequency 872 Hz and duration of 892 ms. From the time-frequency plot of the waveform the gravity mode (g-mode) is very prominent, which corresponds to the increase in frequency.

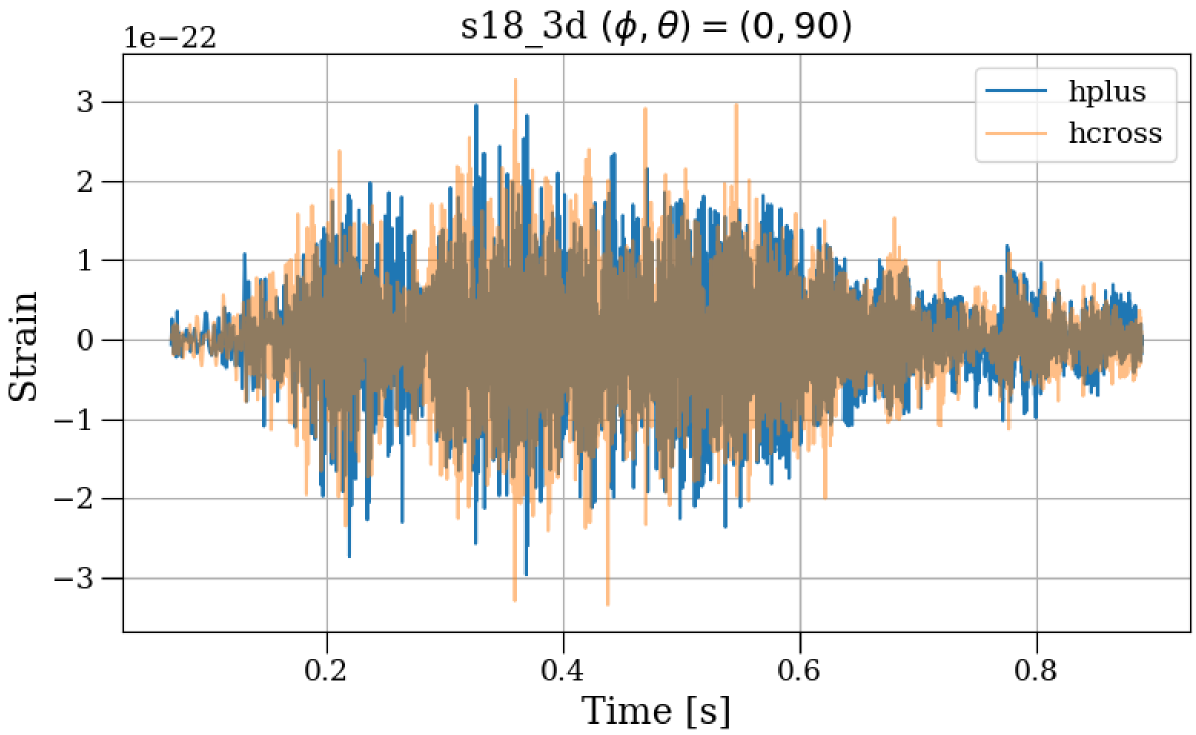

Figure 4.4.3: Powell and Muller s18 Time Series

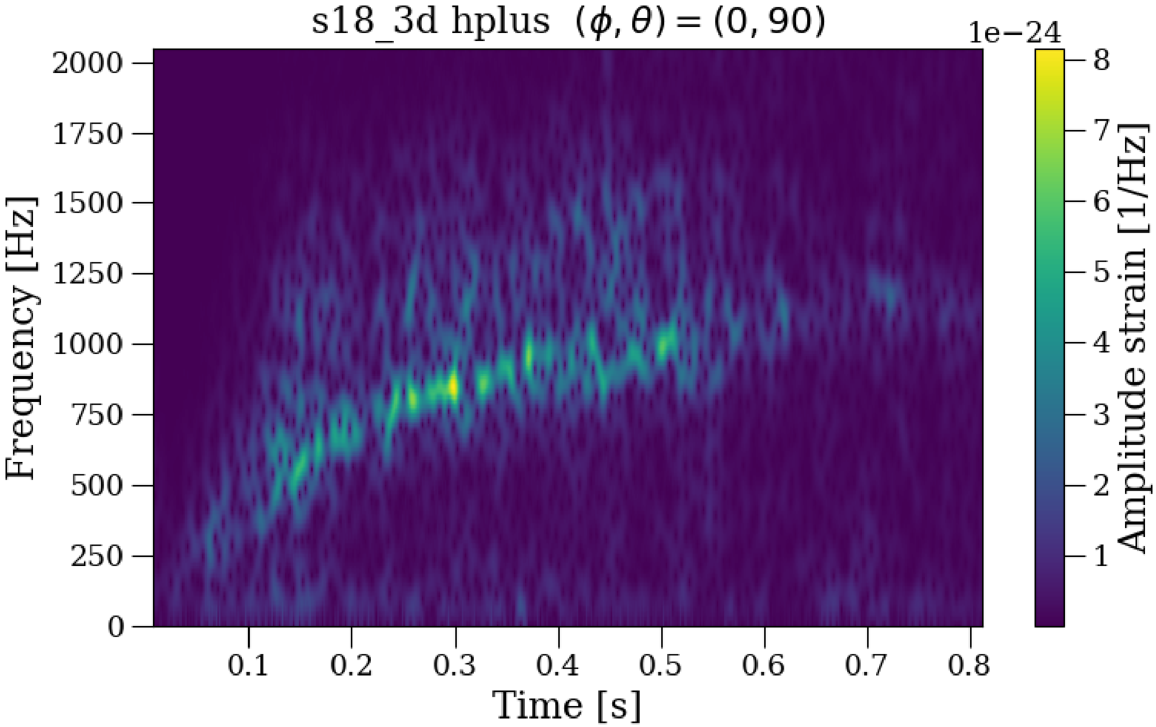

Figure 4.4.4: Powell and Muller s18 Time-Frequency plot. This shows the frequency evolution of the signal with time. https://git.ligo.org/marek.szczepanczyk/sngw/-/tree/master/Powell$_2$018

4.4.4 Morozova M19

Morozova M19 [94] is a 2D general relativistic simulation of CCSN GW signal. It is a non-rotating 19 solar mass progenitor with peak frequency 1851 Hz and duration of 1540 ms. g-mode and f-mode are clearly visible in the time-frequency plot.

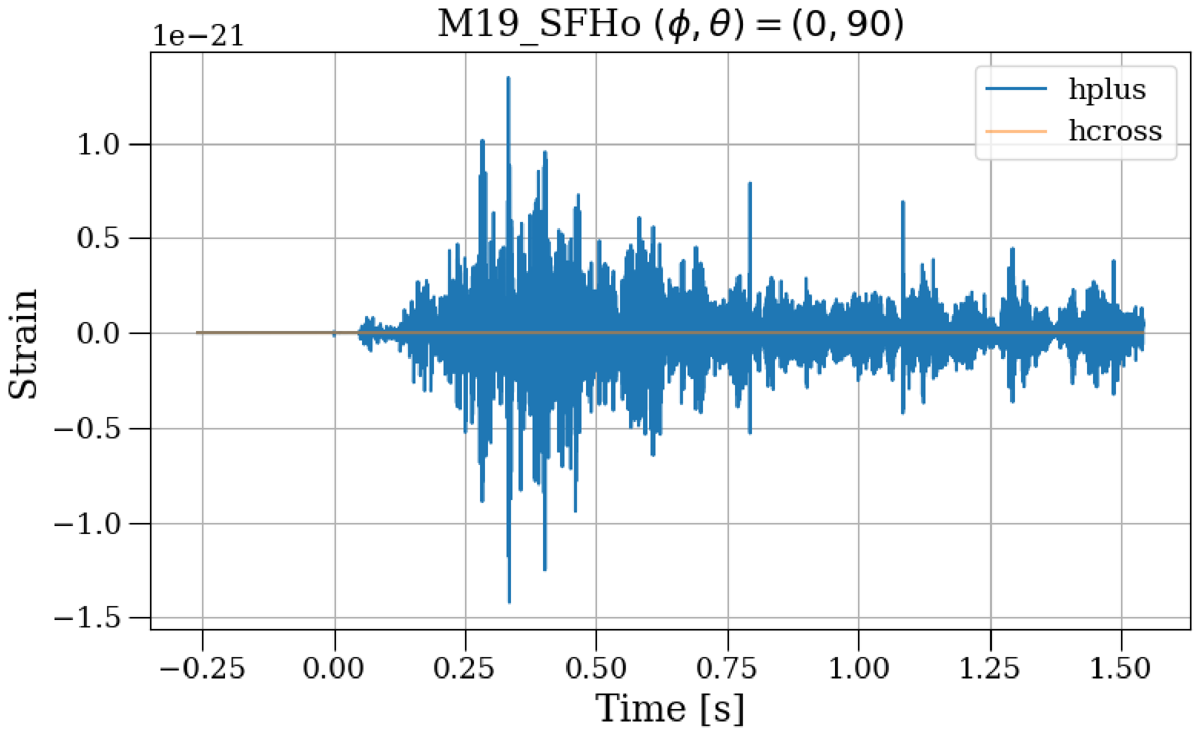

Figure 4.4.5: Morozova M19 Time Series

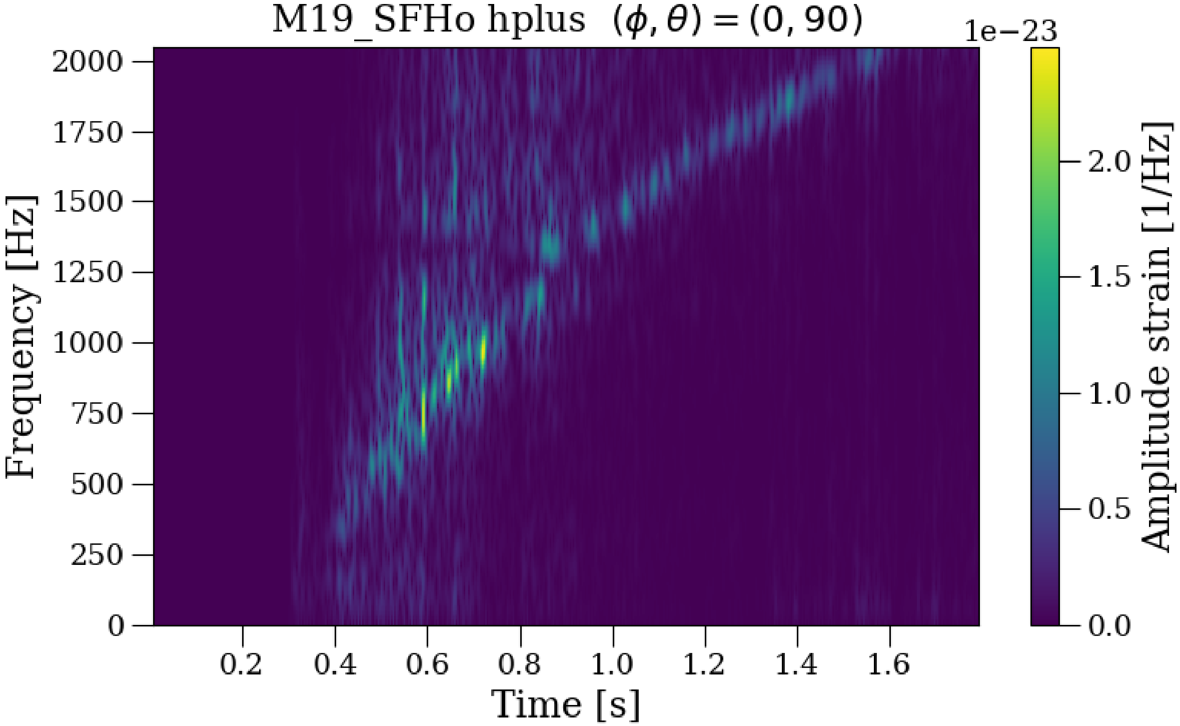

Figure 4.4.6: Morozova M19 Time-Frequency plot. This shows the frequency evolution of the signal with time. https://git.ligo.org/marek.szczepanczyk/sngw/-/tree/master/Morozova$_2018/M19_SFHo$

4.4.5 Kuroda 2016 TM1

Kuroda 2016 TM1 [95] is a 3D general relativistic simulation of CCSN GW signal. It is a non-rotating 15 solar mass progenitor with peak frequency 714 Hz and duration of 350 ms. Both gravity mode and SASI is present in the Time-Frequency plot.

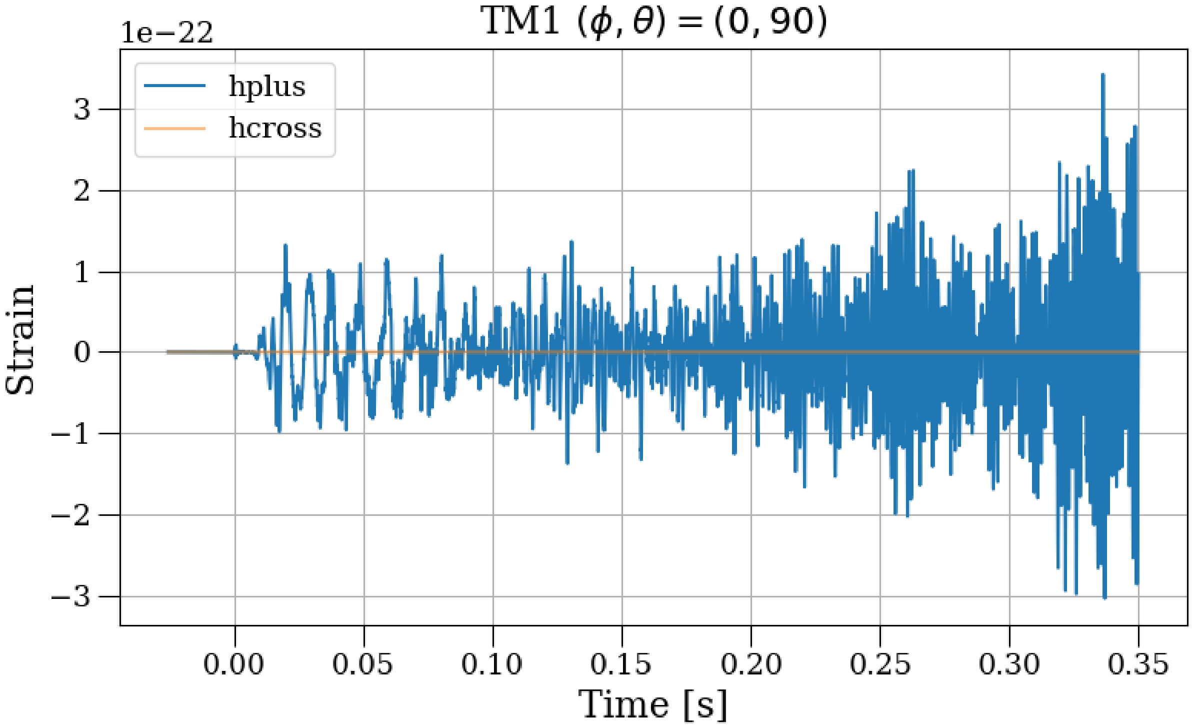

Figure 4.4.7: Kuroda 2016 TM1 Time Series

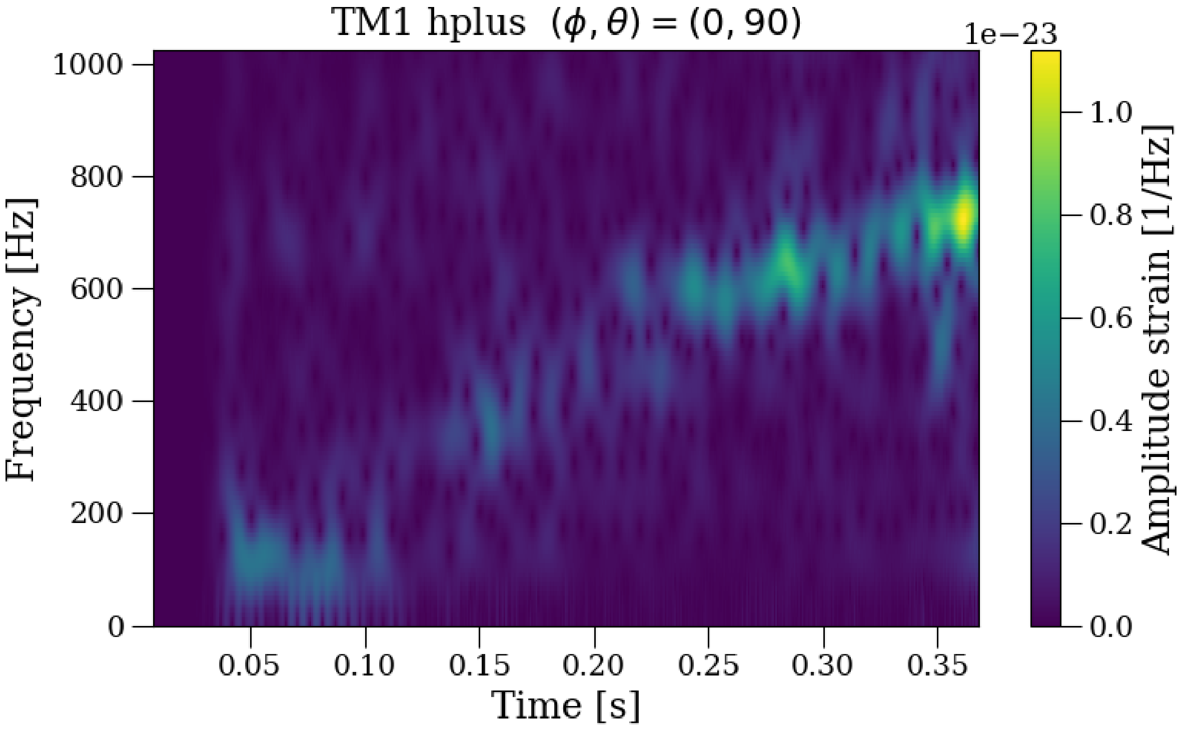

Figure 4.4.8: Kuroda 2016 TM1 Time-Frequency plot. This shows the frequency evolution of the signal with time. https://git.ligo.org/marek.szczepanczyk/sngw/-/tree/master/Kuroda$_2016/TM1$

4.4.6 Mezzacappa C15 3D

Mezzacappa C15 3D [96] is a 3D general relativistic simulation of CCSN GW signal. It is a non-rotating 15 solar mass progenitor with peak frequency 1064 Hz and duration of 420 ms. From the time-frequency plot of the waveform the gravity mode (g-mode) and SASI are present.

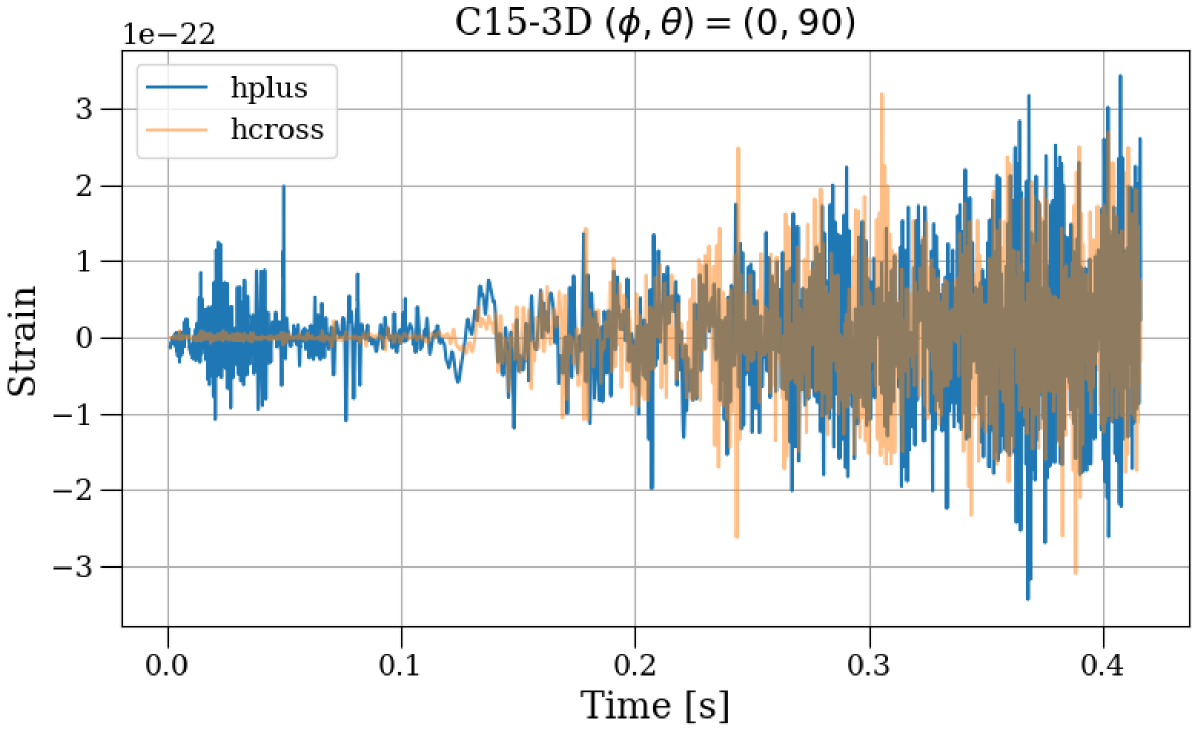

Figure 4.4.9: Mezzacappa C15 3D Time Series

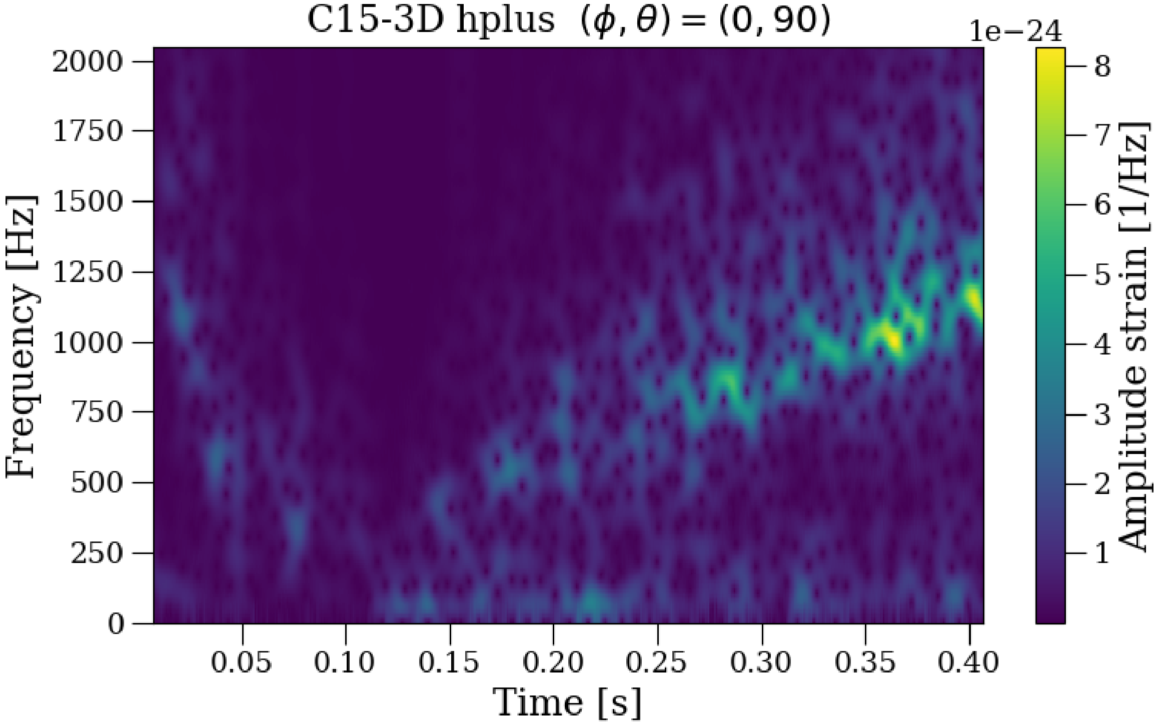

Figure 4.4.10: Mezzacappa C15 3D Time-Frequency plot. This shows the frequency evolution of the signal with time. https://git.ligo.org/marek.szczepanczyk/sngw/-/tree/master/Mezzacappa$_2$020$/C15-3D$

4.4.7 Detection Efficiency

Efficiency Curve

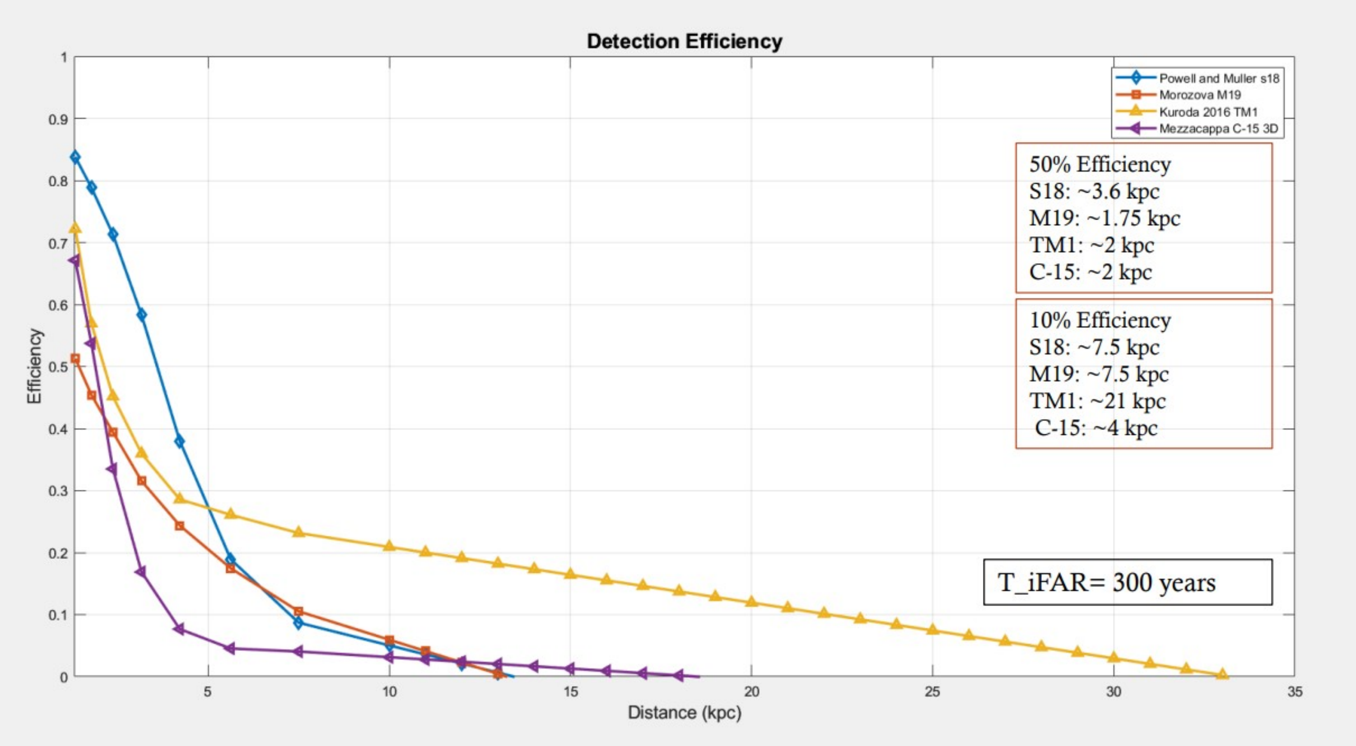

Figure 4.4.11: This figure shows the detection efficiency of 4 waveforms - Powell and Muller s18, Morozova M19, Kuroda 2016 TM1 and Mezzacappa c15 3D by MuLaSEcC pipeline as a function of distance

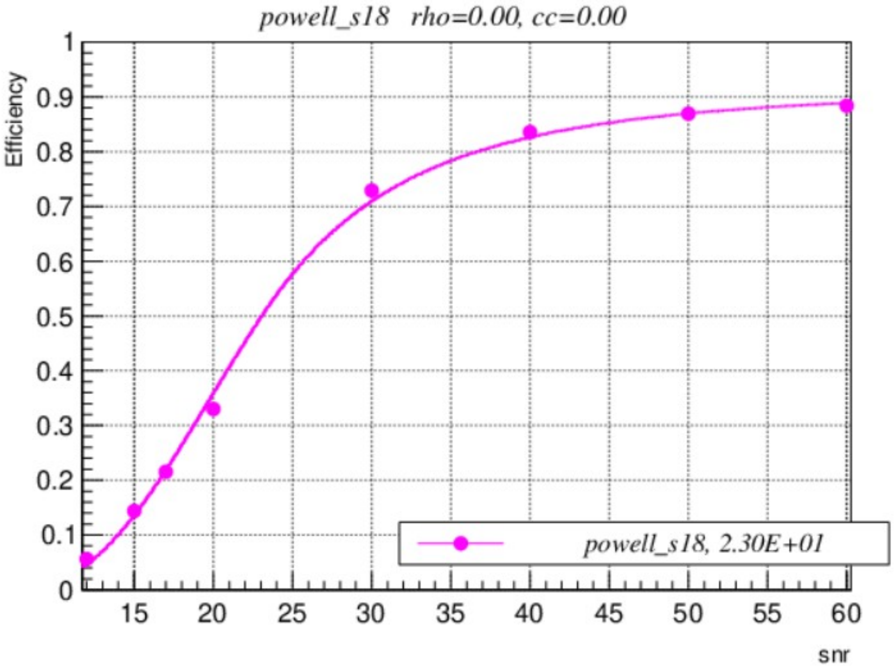

Figure 4.4.12: This figure shows the detection efficiency of Powell and Muller s18 waveform by MuLaSEcC pipeline as a function of Signal to Noise Ratio (SNR)

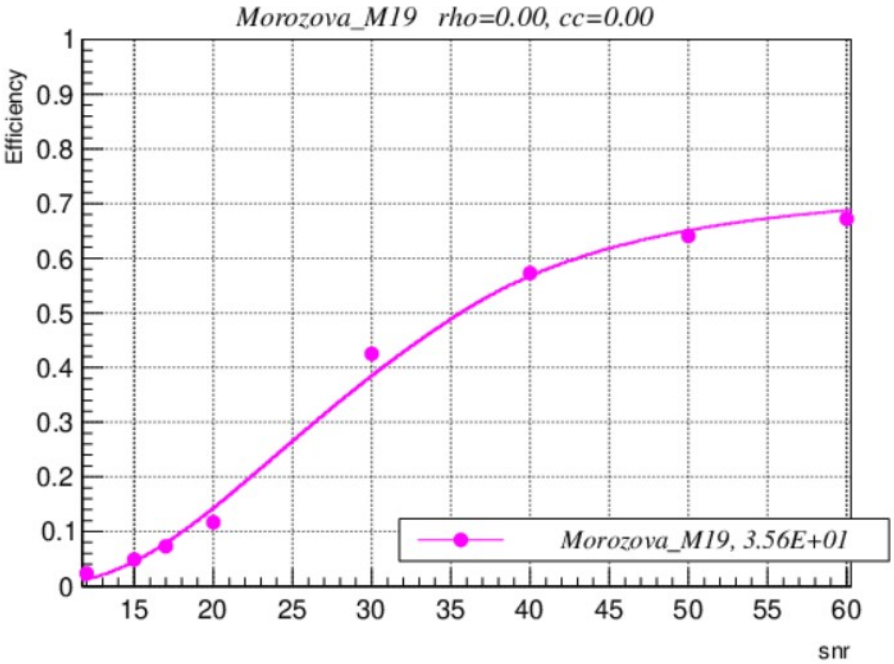

Figure 4.4.13: This figure shows the detection efficiency of Morozova M19 waveform by MuLaSEcC pipeline as a function of Signal to Noise Ratio (SNR)

4.4.8 RHO Distribution of Detected Injectiions

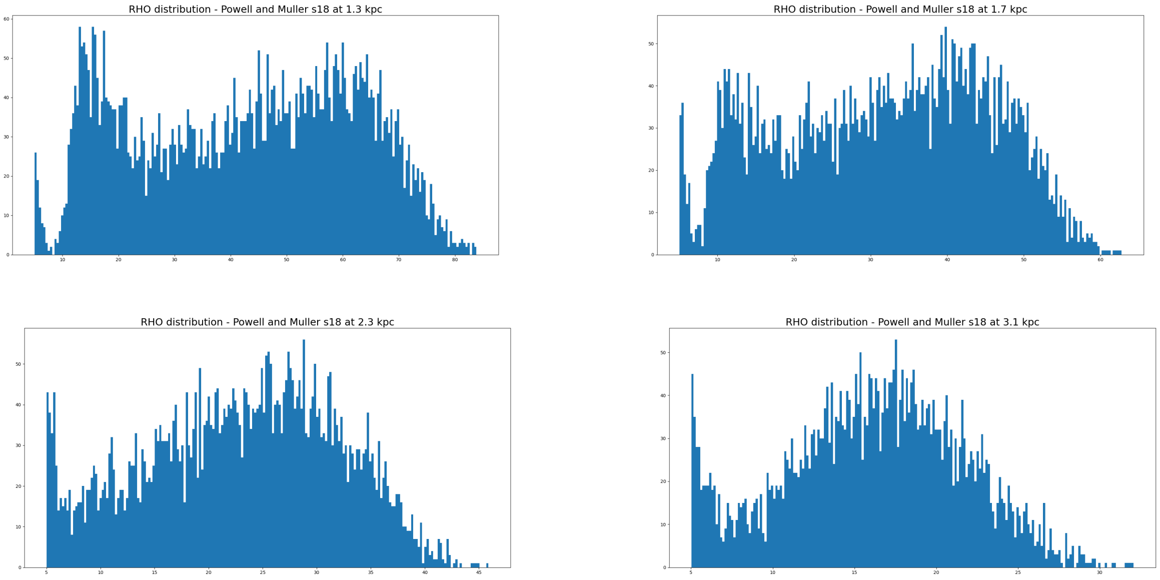

Figure 4.4.14: This figure shows the distribution of RHO values for Powell and Muller s18 waveforms injected at distances 1.3, 1.7, 2.3 and 3.1 kpc. x-axis is RHO and y-axis is numbers.

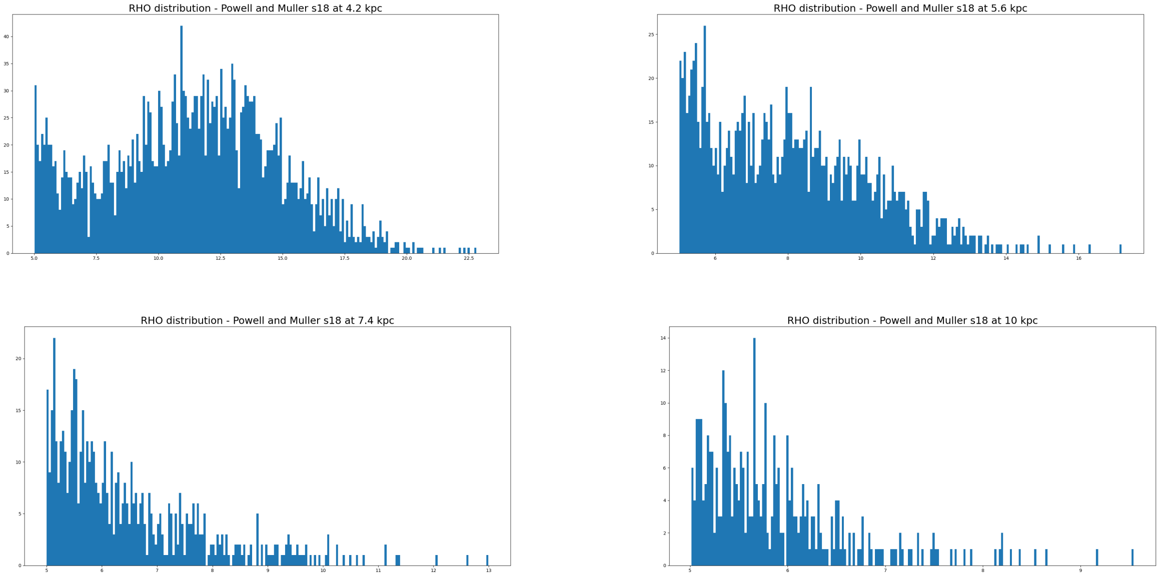

Figure 4.4.15: This figure shows the distribution of RHO values for Powell and Muller s18 waveforms injected at distances 4.2, 5.6, 7.4 and 10 kpc. x-axis is RHO and y-axis is numbers.

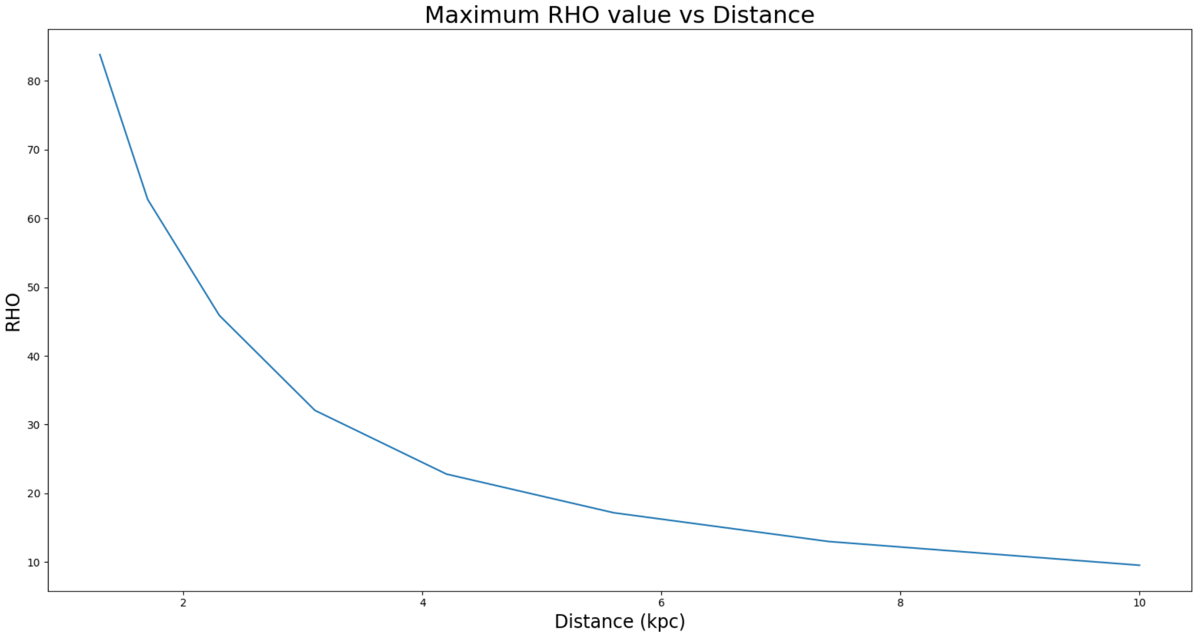

Figure 4.4.16: This figure shows how the maximum RHO value or strength of the signal detected is changing with the distance it was injected at. As expected, maximum values of RHO go down with increasing distance.

4.4.9 Reconstructions

Besides detecting GW signals parameter estimation and reconstruction of the detected signal is important in order to gather information about the source. We have been able to achieve superior reconstructions as compared to cWB for sources that are around the middle of the galaxy, i.e., between 3 to 8 kpc for both Powell and Muller s18 and Morozova M19 that are shown in the following figures.

4.4.10 Powell and Muller s18

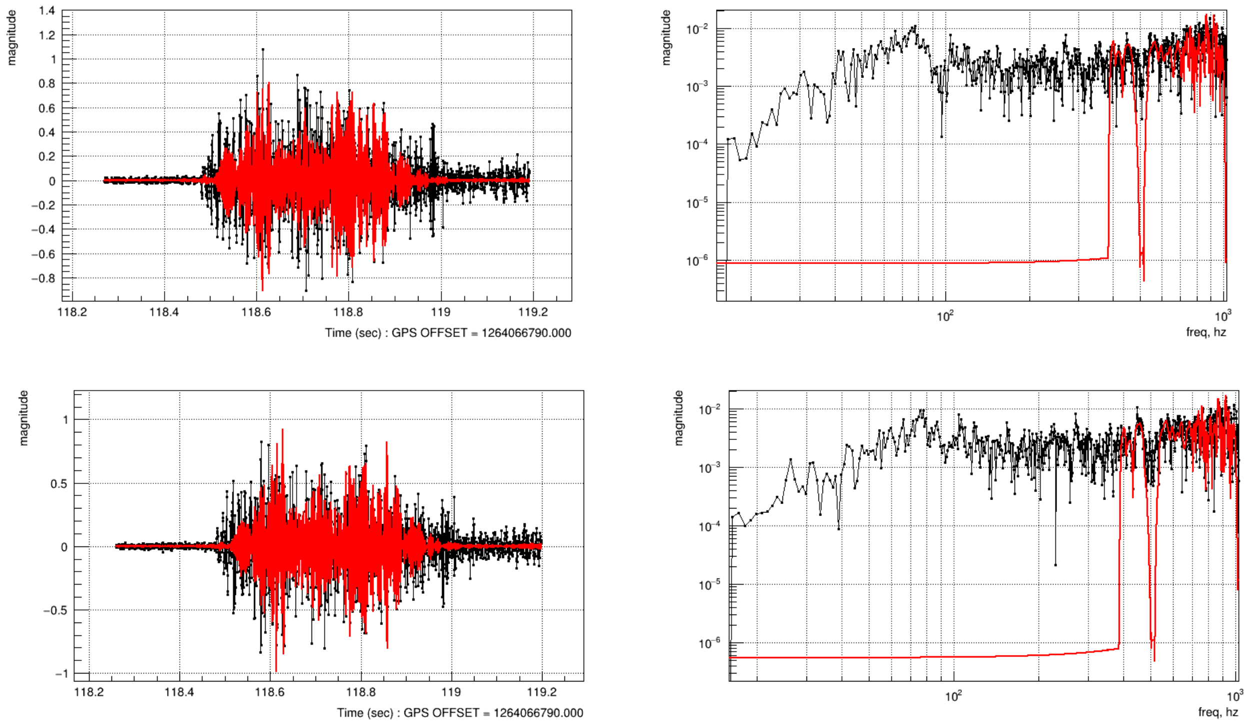

Figure 4.4.17: Reconstructions of detected signal by cWB that was injected at 2.3 kpc. Top row is for L1 and bottom row is for H1. Left column is the time series and right column is the frequency map of the signal. Black is the injected signal and red is the reconstructed signal.

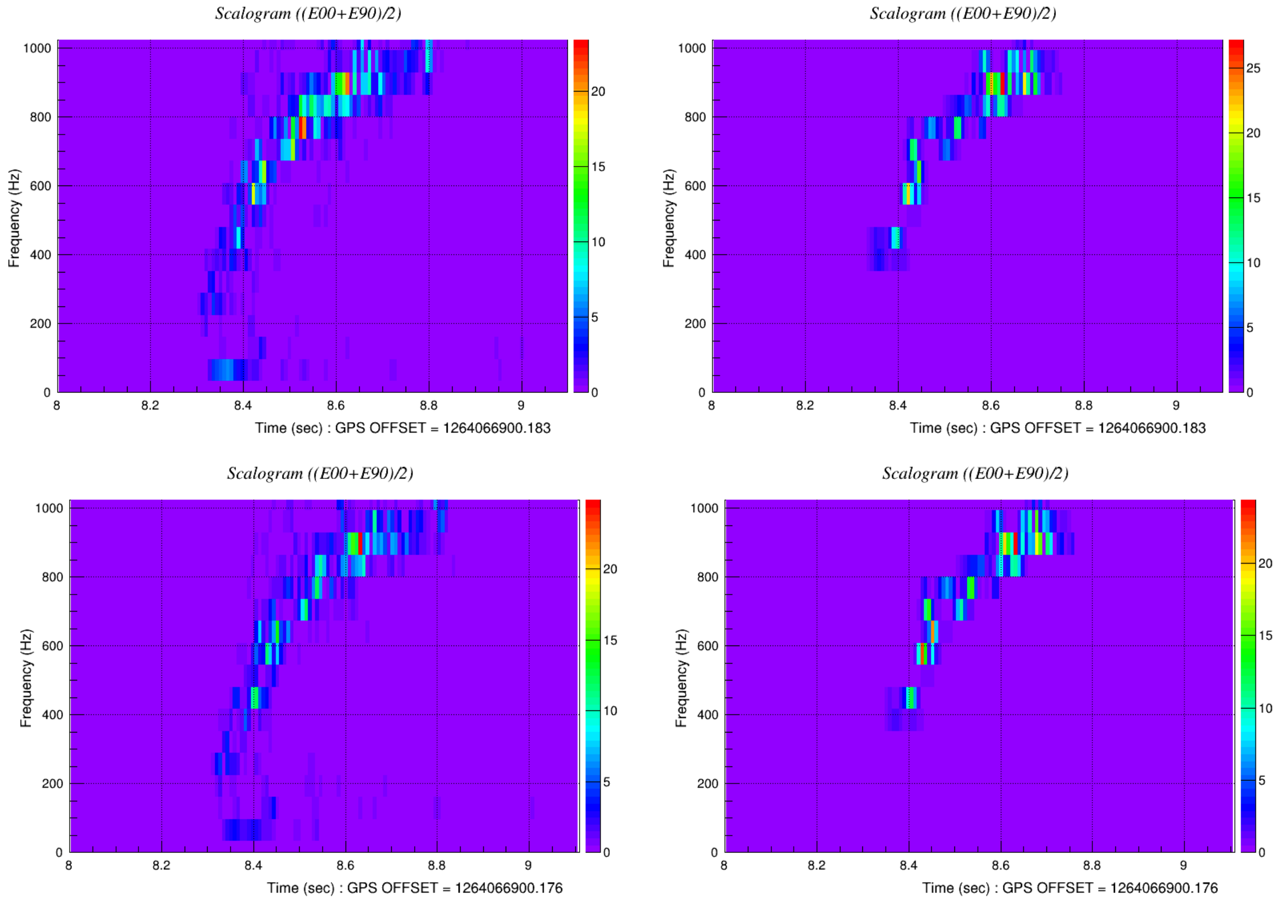

Figure 4.4.18: Time-frequency representation of injected signal at 2.3 kpc on the left and reconstructed signal by cWB on the right. Top row is for L1 and bottom row is for H1 detector.

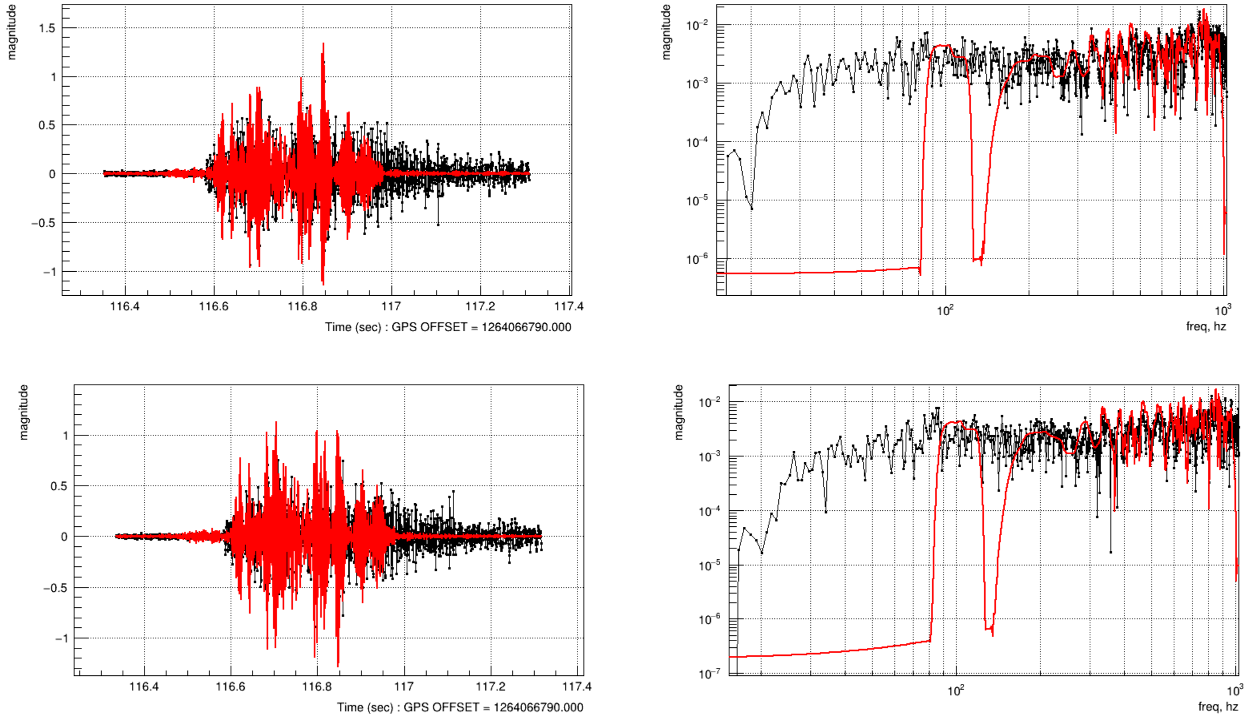

Figure 4.4.19: Reconstructions of detected signal by MuLaSE injected at 2.3 kpc. Top row is for L1 and bottom row is for H1. Left column is the time series and right column is the frequency map of the signal. Black is the injected signal and red is the reconstructed signal.

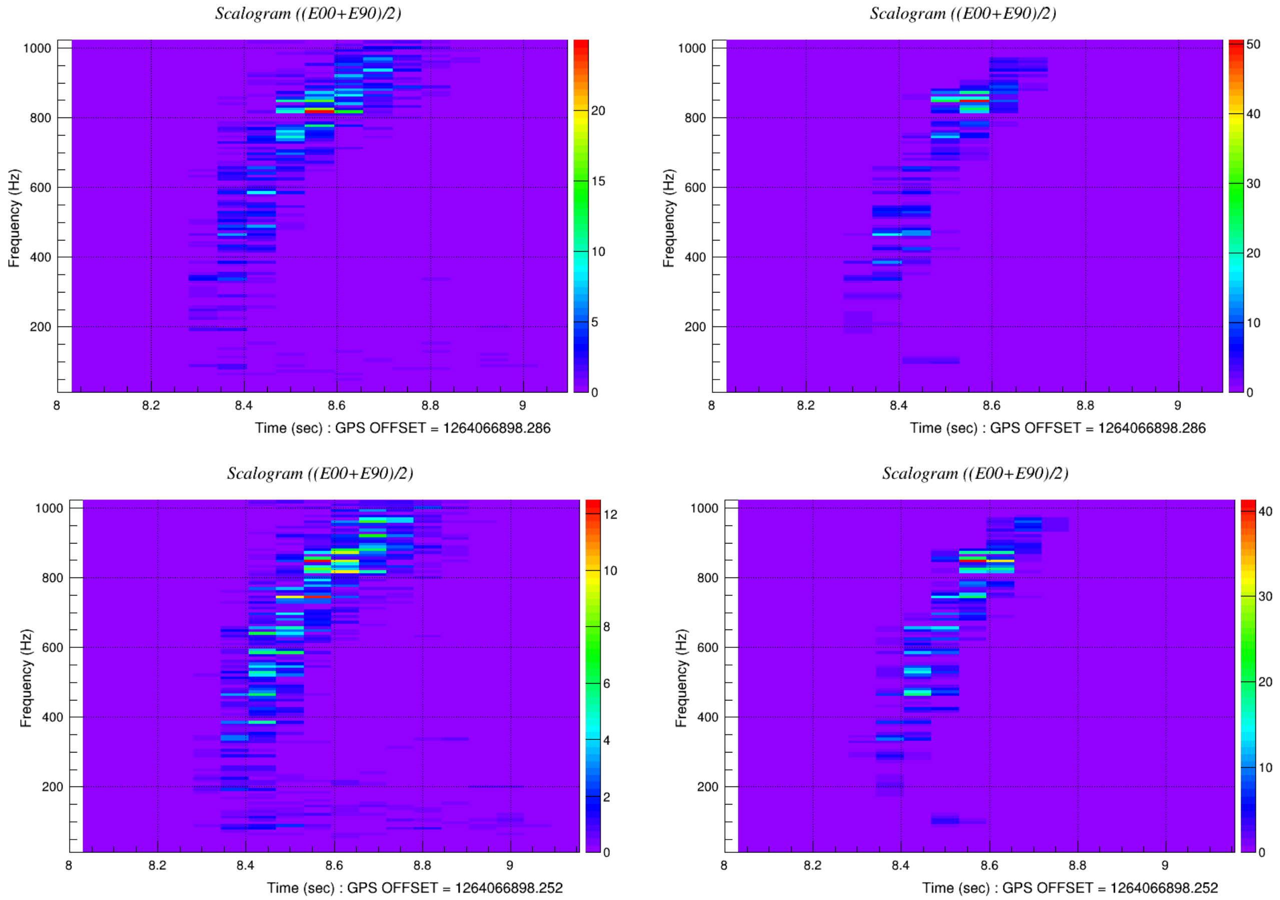

Figure 4.4.20: Time-frequency representation of injected signal at 2.3 kpc on the left and reconstructed signal by MuLaSE on the right. Top row is for L1 and bottom row is for H1 detector.

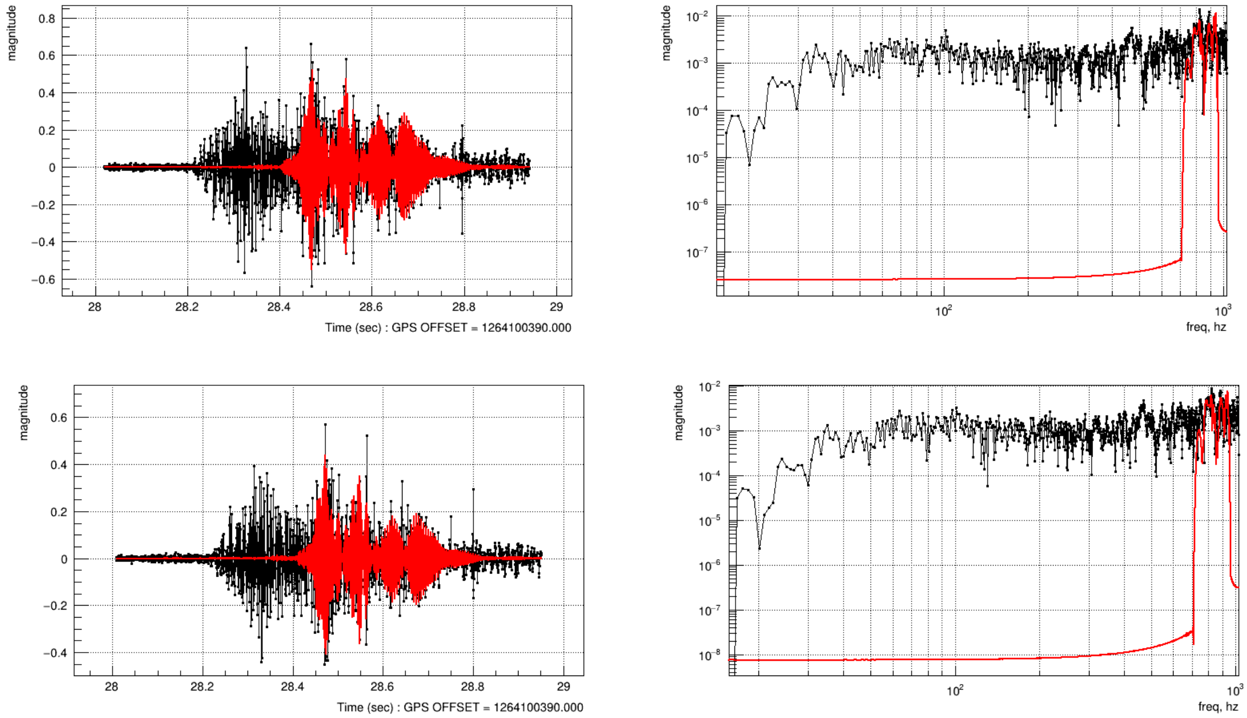

Figure 4.4.21: Reconstructions of detected signal by cWB injected at 5.6 kpc. Top row is for L1 and bottom row is for H1. Left column is the time series and right column is the frequency map of the signal. Black is the injected signal and red is the reconstructed signal.

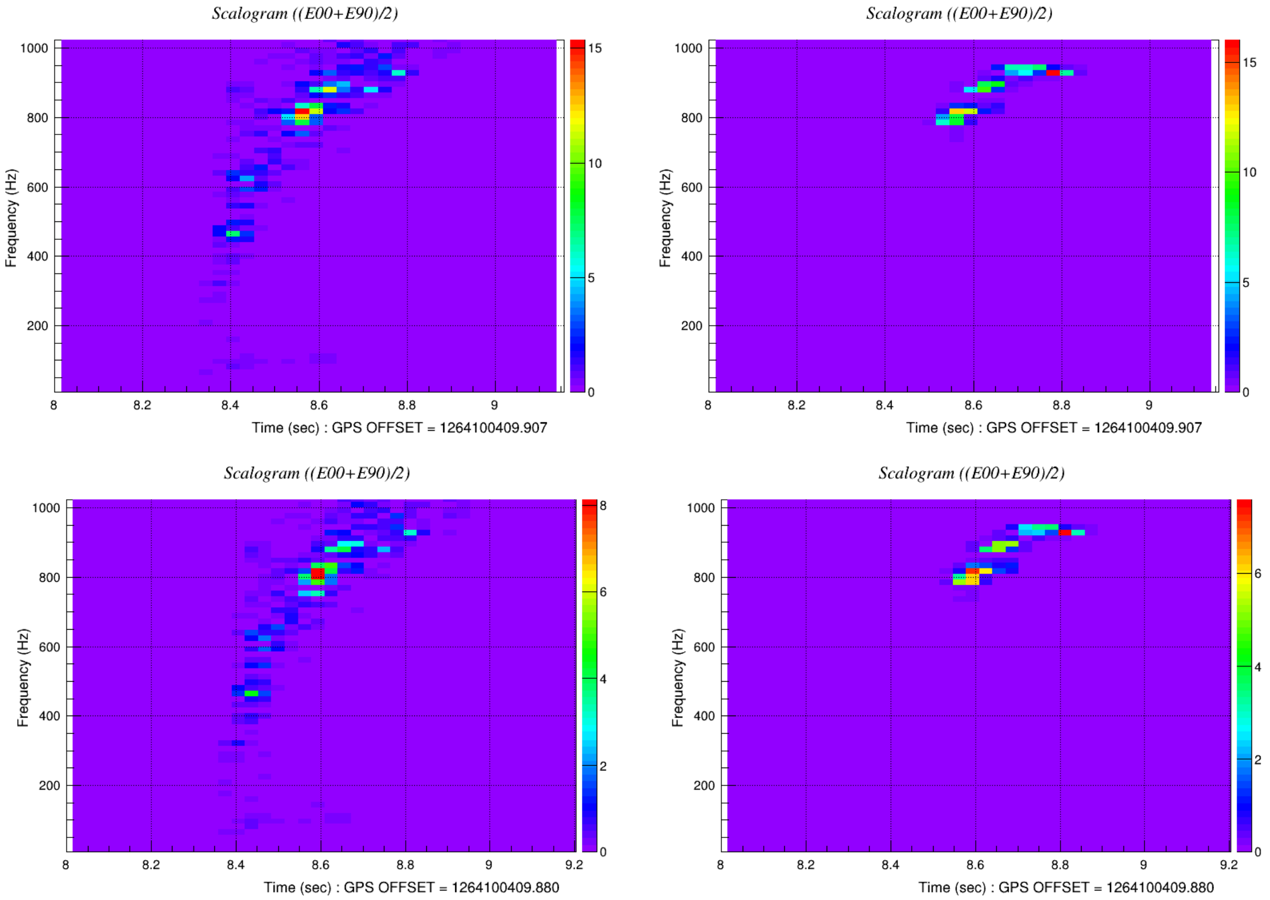

Figure 4.4.22: Time-frequency representation of injected Powell and Muller s18 signal at 5.6 kpc on the left and reconstructed signal by cWB on the right. Top row is for L1 and bottom row is for H1 detector.

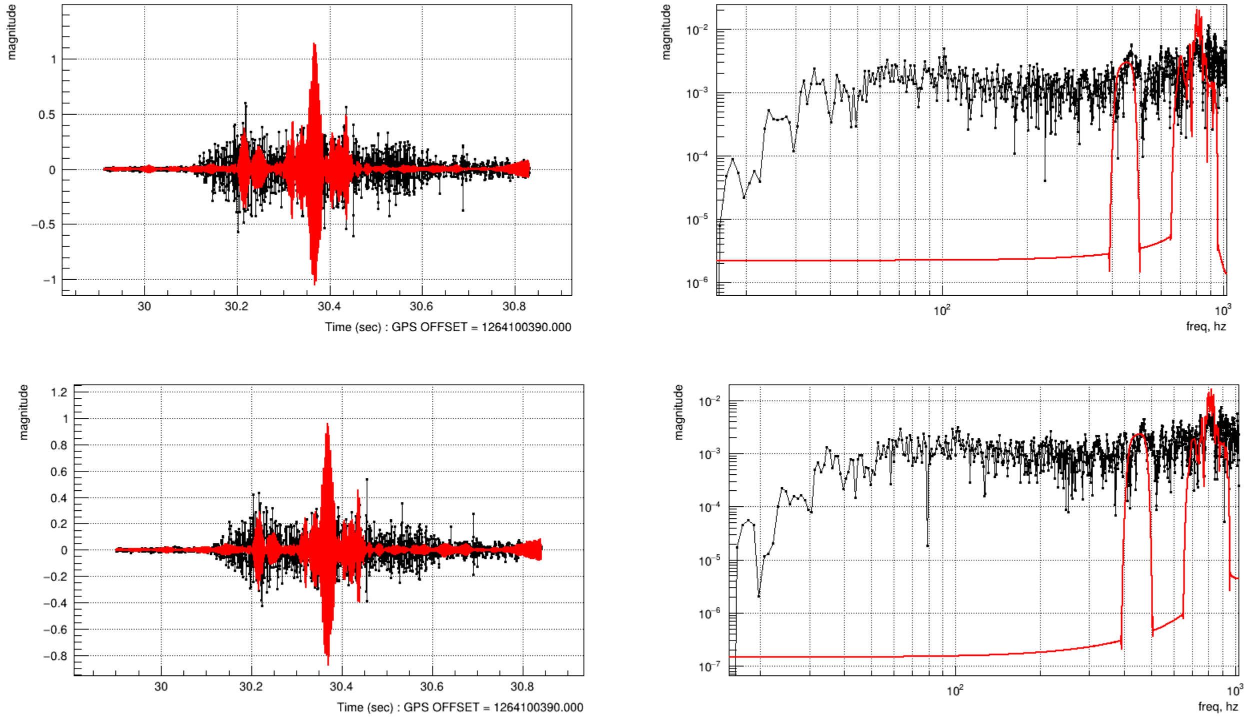

Figure 4.4.23: Reconstructions of detected signal by MuLaSE injected at 5.6 kpc. Top row is for L1 and bottom row is for H1. Left column is the time series and right column is the frequency map of the signal. Black is the injected signal and red is the reconstructed signal.

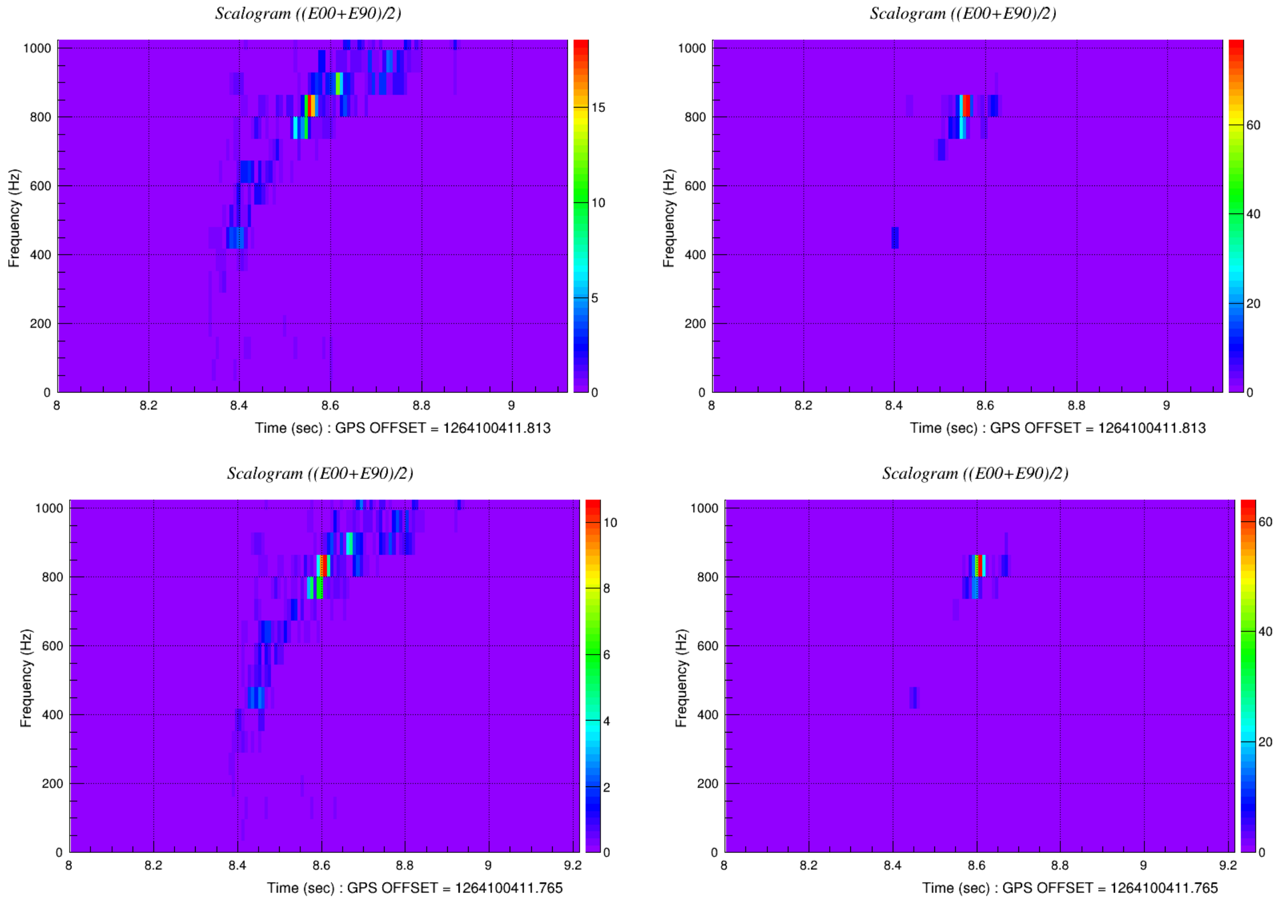

Figure 4.4.24: Time-frequency representation of injected Powell and Muller s18 signal at 5.6 kpc on the left and reconstructed signal by MuLaSE on the right. Top row is for L1 and bottom row is for H1 detector.

4.4.11 Morozova M19

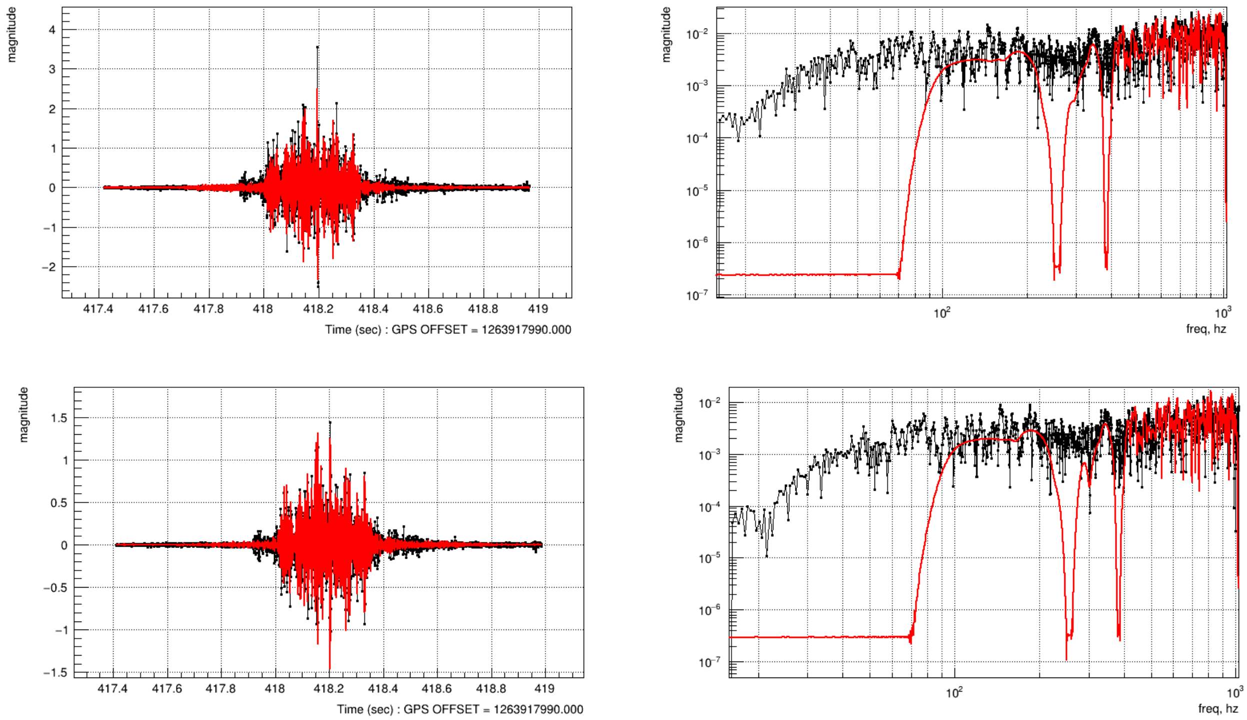

Figure 4.4.25: Reconstructions of detected signal by cWB injected at 2.3 kpc. Top row is for L1 and bottom row is for H1. Left column is the time series and right column is the frequency map of the signal. Black is the injected signal and red is the reconstructed signal.

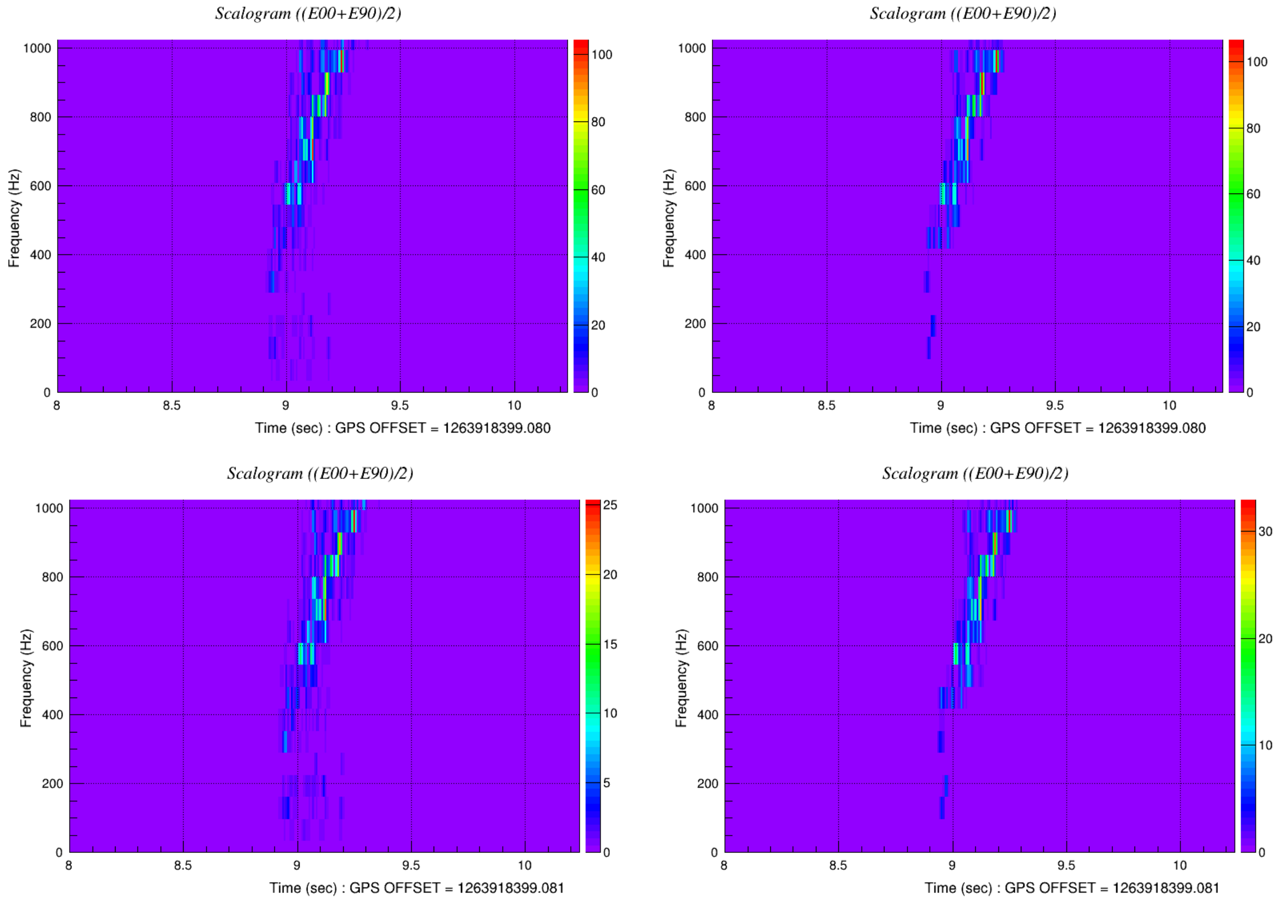

Scalogram ((E00+E90)/2)

Scalogram ((E00+E90)/2)

Scalogram ((E00+E90)/2)

Scalogram ((E00+E90)/2)

Figure 4.4.26: Time-frequency representation of injected signal at 2.3 kpc on the left and reconstructed signal by cWB on the right. Top row is for L1 and bottom row is for H1 detector.

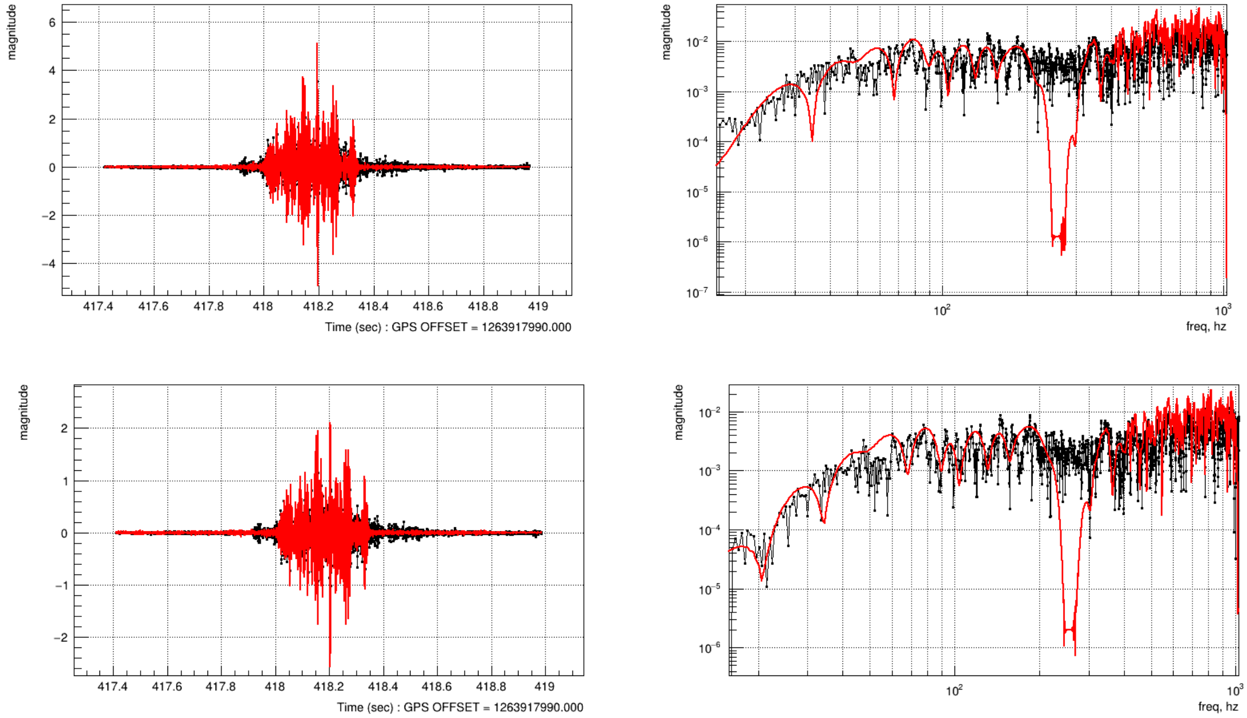

Figure 4.4.27: Reconstructions of detected signal by MuLaSE injected at 2.3 kpc. Top row is for L1 and bottom row is for H1. Left column is the time series and right column is the frequency map of the signal. Black is the injected signal and red is the reconstructed signal.

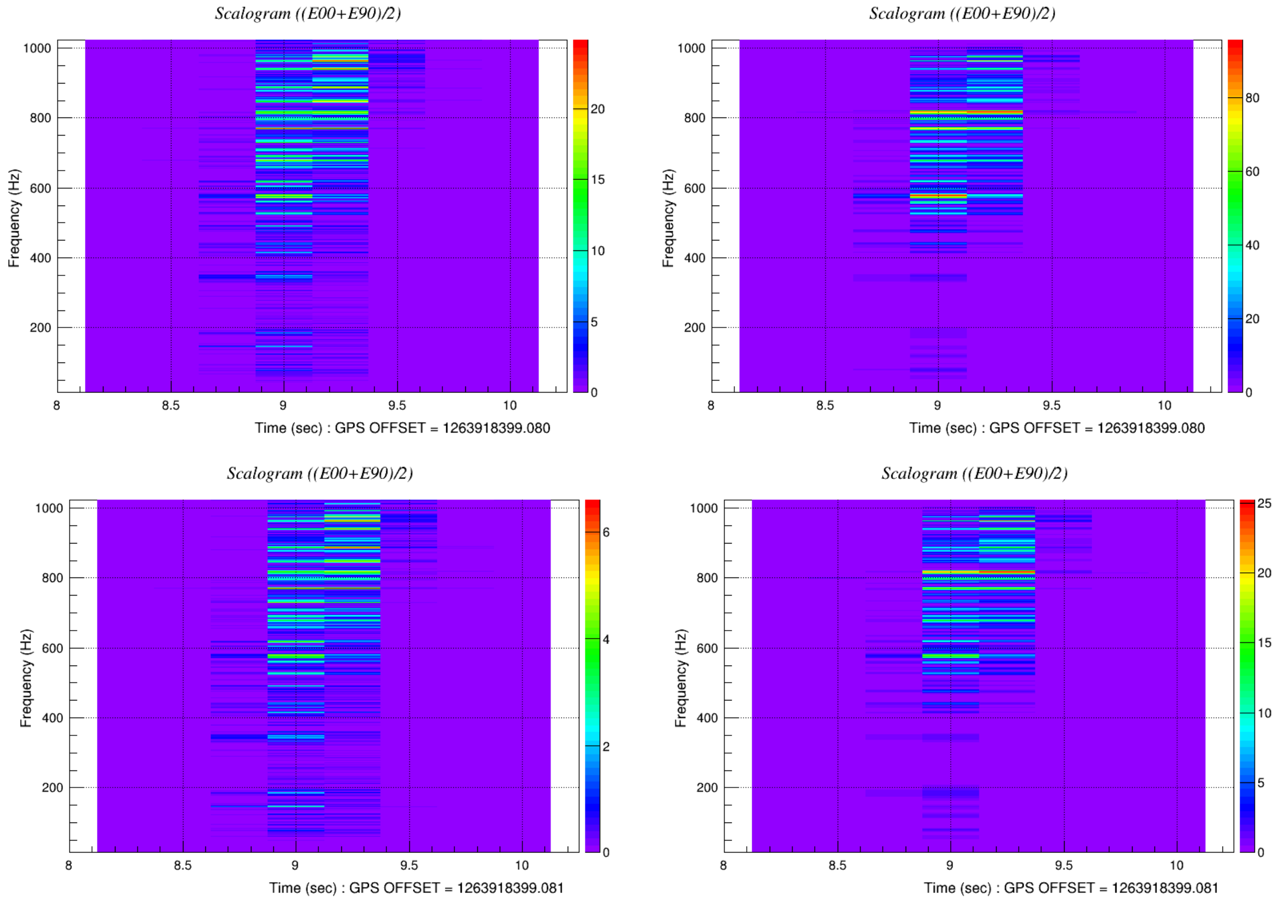

Figure 4.4.28: Time-frequency representation of injected signal at 2.3 kpc on the left and reconstructed signal by MuLaSE on the right. Top row is for L1 and bottom row is for H1 detector.

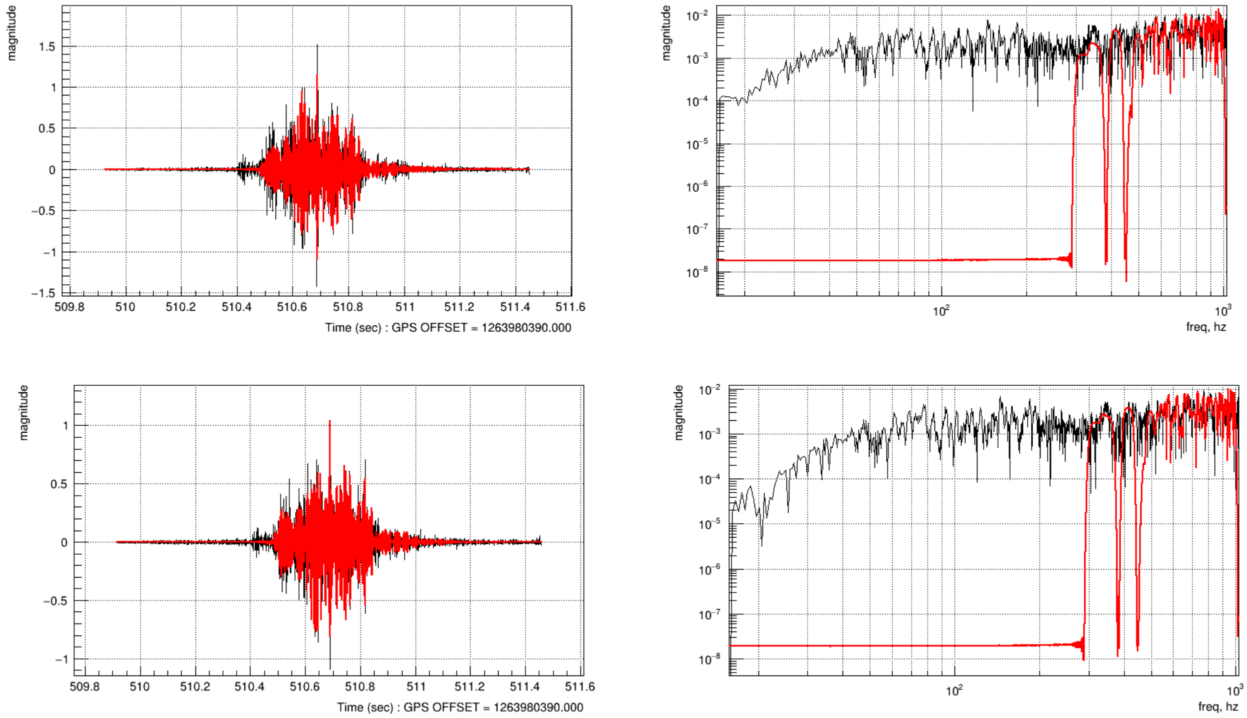

Figure 4.4.29: Reconstructions of detected signal by cWB injected at 5.6 kpc. Top row is for L1 and bottom row is for H1. Left column is the time series and right column is the frequency map of the signal. Black is the injected signal and red is the reconstructed signal.

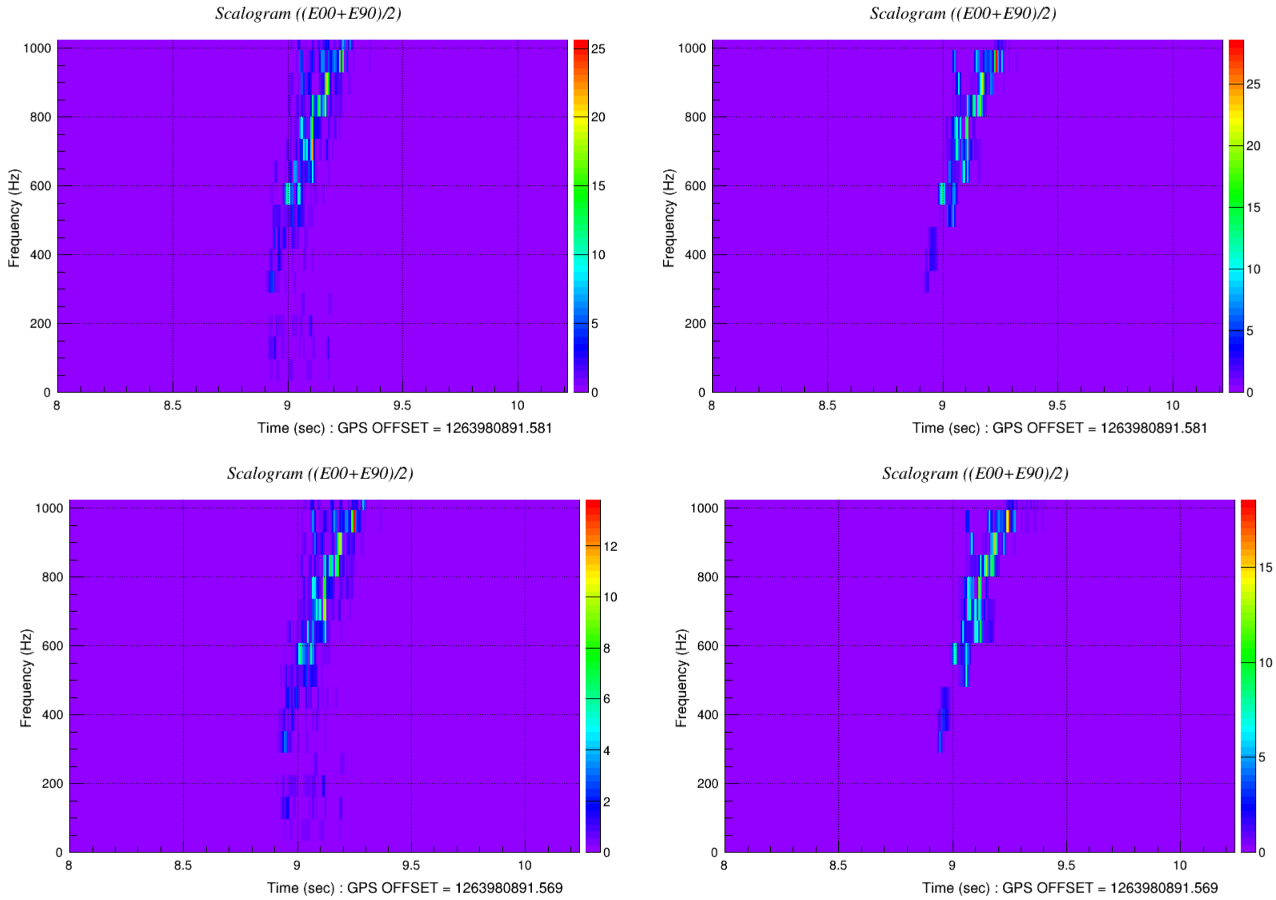

Figure 4.4.30: Time-frequency representation of injected signal at 5.6 kpc on the left and reconstructed signal by cWB on the right. Top row is for L1 and bottom row is for H1 detector.

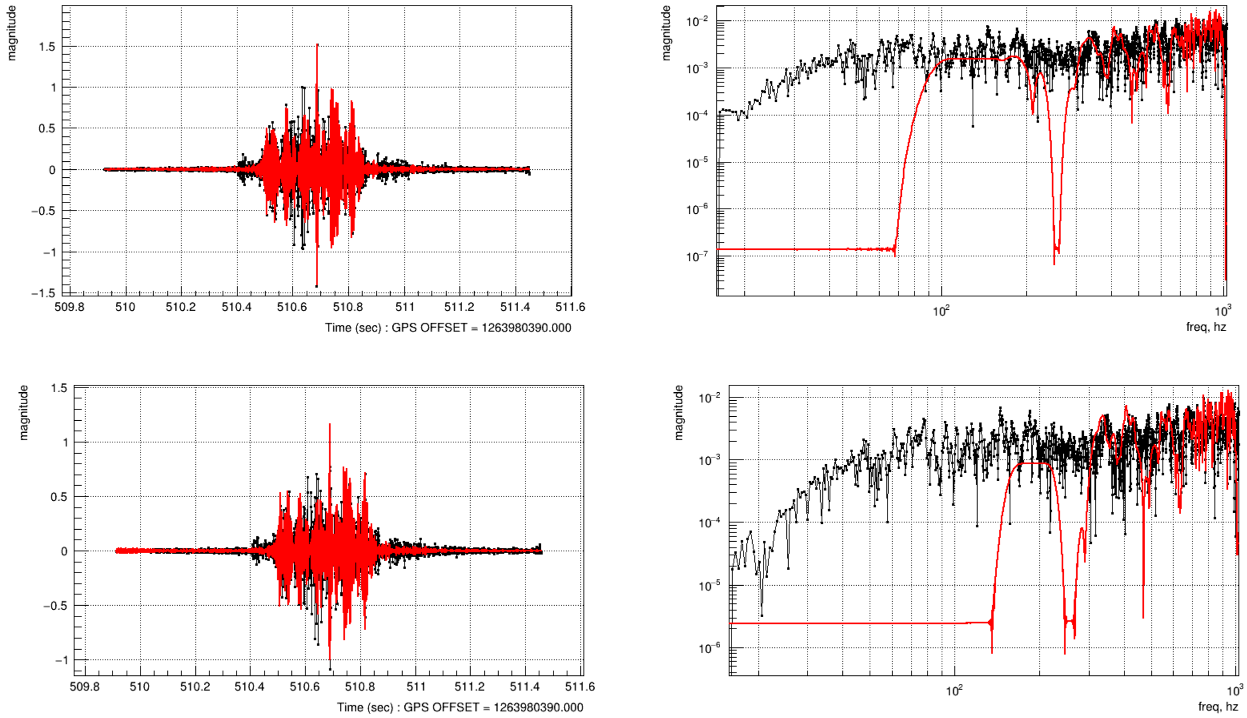

Figure 4.4.31: Reconstructions of detected signal by MuLaSE injected at 5.6 kpc. Top row is for L1 and bottom row is for H1. Left column is the time series and right column is the frequency map of the signal. Black is the injected signal and red is the reconstructed signal.

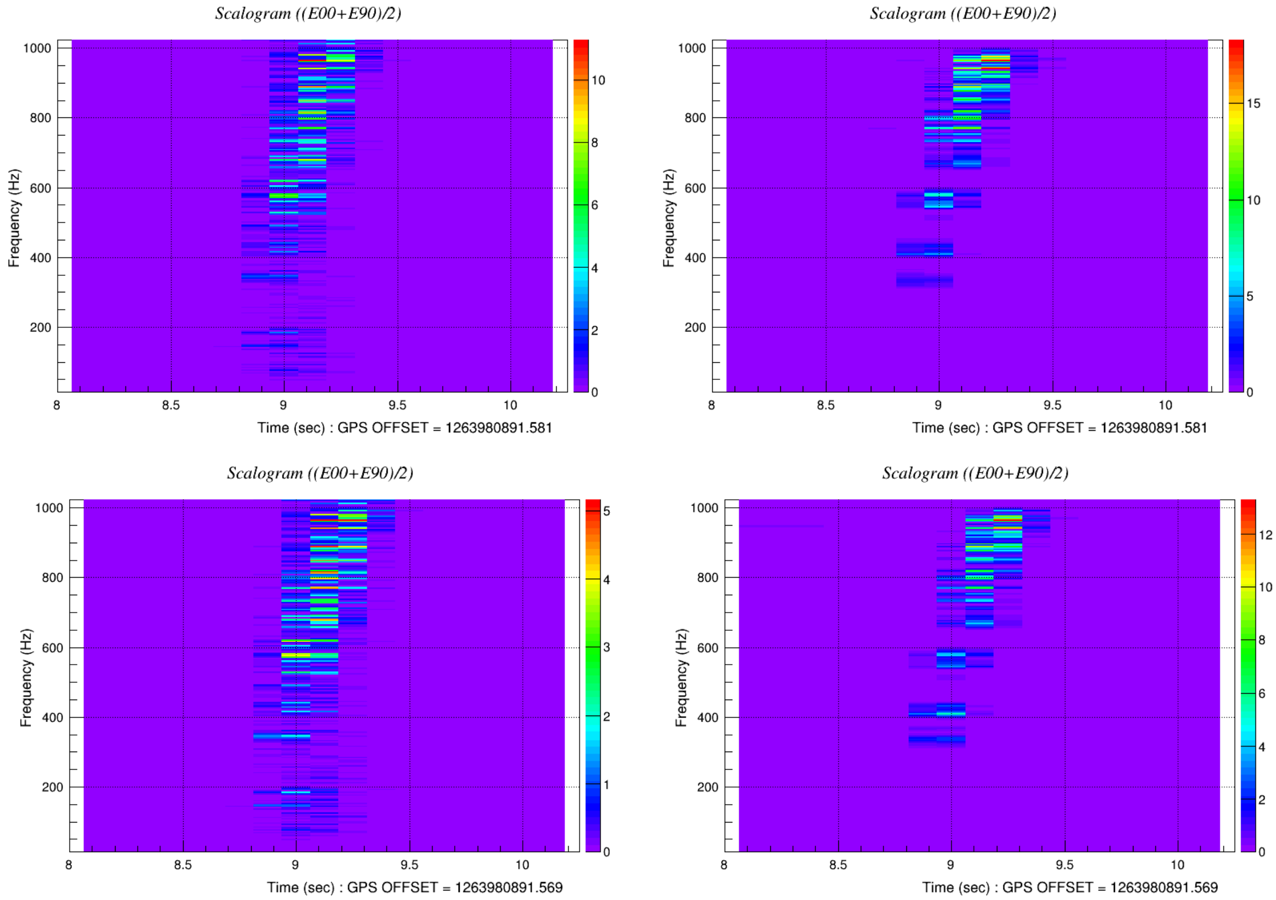

Figure 4.4.32: Time-frequency representation of injected signal at 5.6 kpc on the left and reconstructed signal by MuLaSE on the right. Top row is for L1 and bottom row is for H1 detector.

4.4.12 Mezzacappa c15 3D

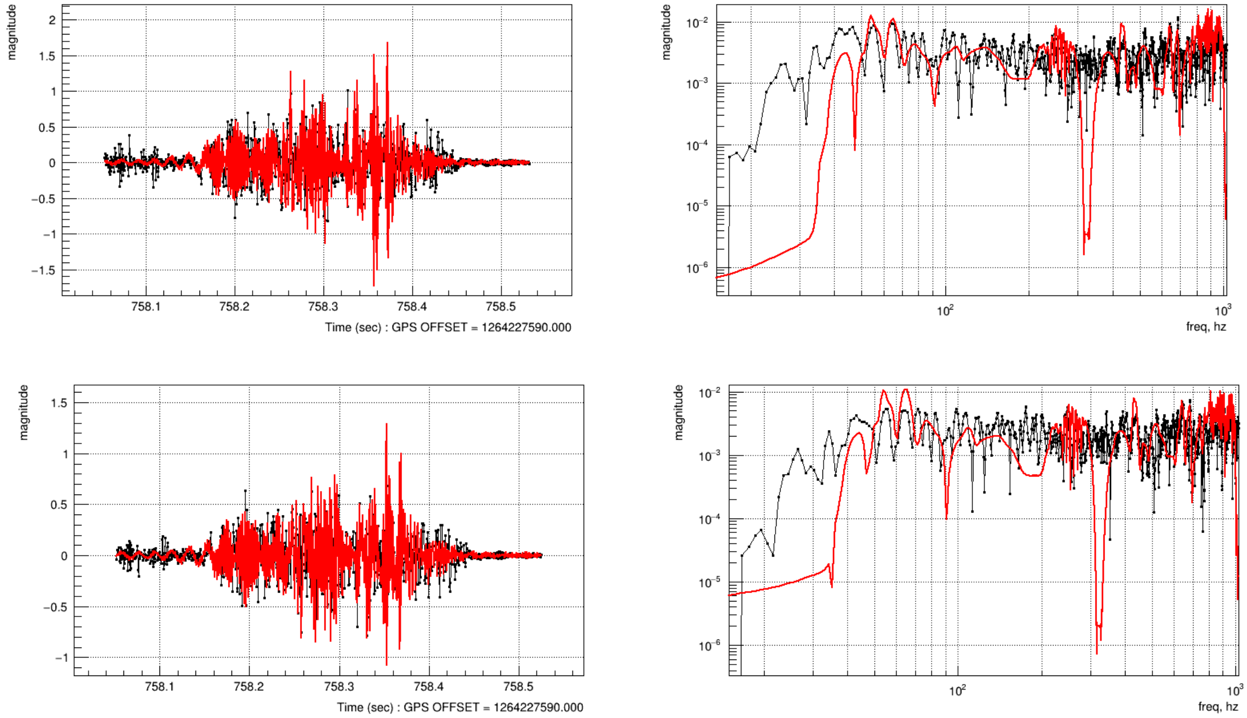

Figure 4.4.33: Reconstructions of detected signal by MuLaSE injected at 2.3 kpc. Top row is for L1 and bottom row is for H1. Left column is the time series and right column is the frequency map of the signal. Black is the injected signal and red is the reconstructed signal.

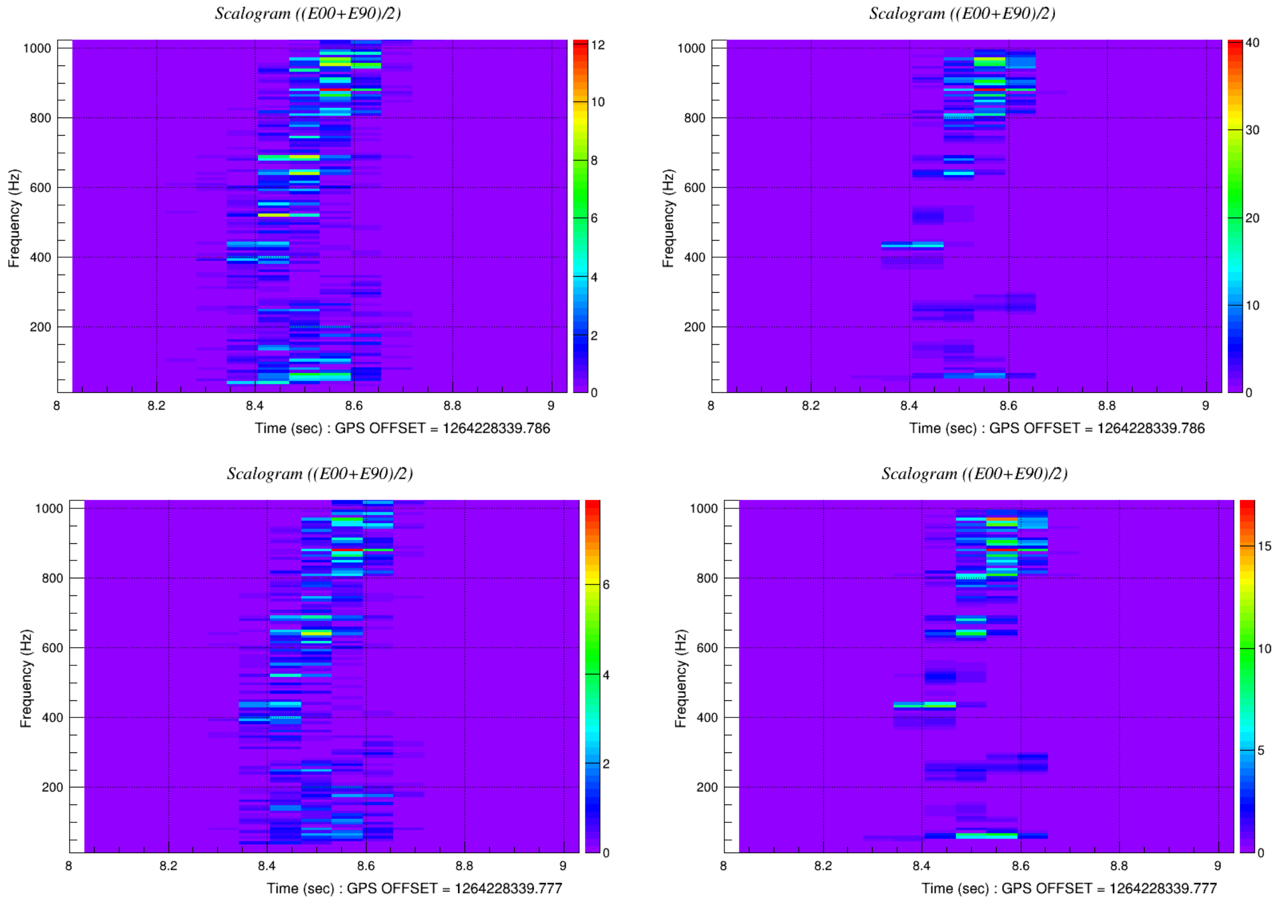

Figure 4.4.34: Time-frequency representation of injected Mezzacappa c15 3D signal at kpc on the left and reconstructed signal by MuLaSE on the right. Top row is for L1 and bottom row is for H1 detector.

4.4.13 Receiver Operating Characteristic

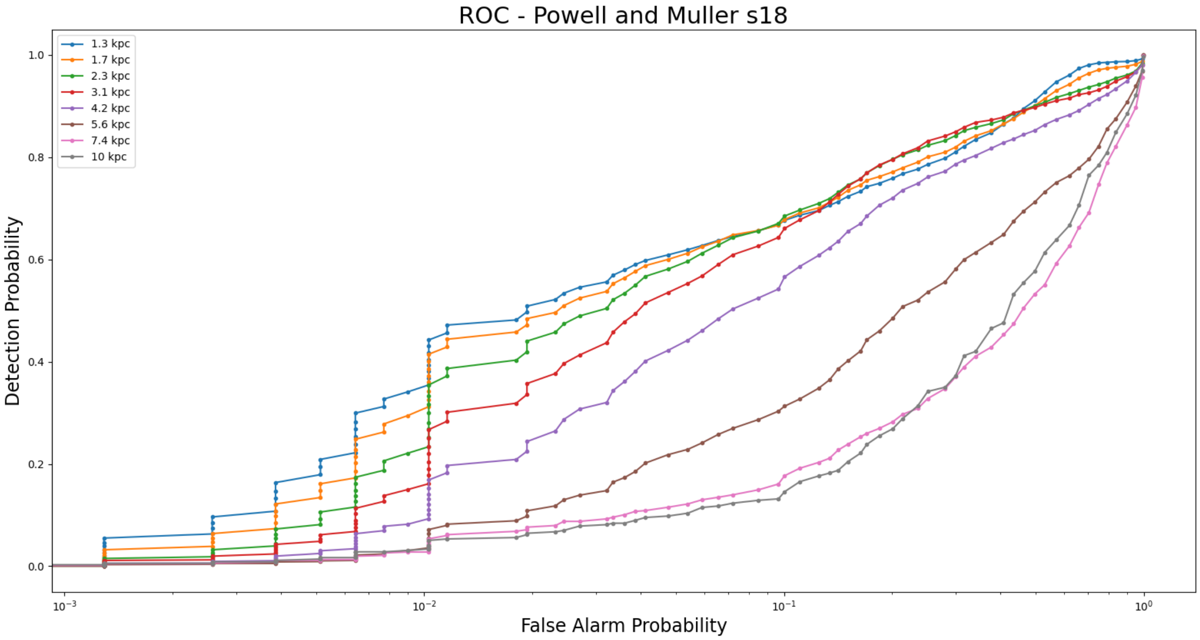

Figure 4.4.35: Receiver Operating Characteristic of Powell and Muller s18 at distances between 1.3 and 10 kpc. Along the x axis there is False Alarm Probability (FAP) and along the y axis there is Detection Probability (DP). Detection Probability increases with False Alarm Probability

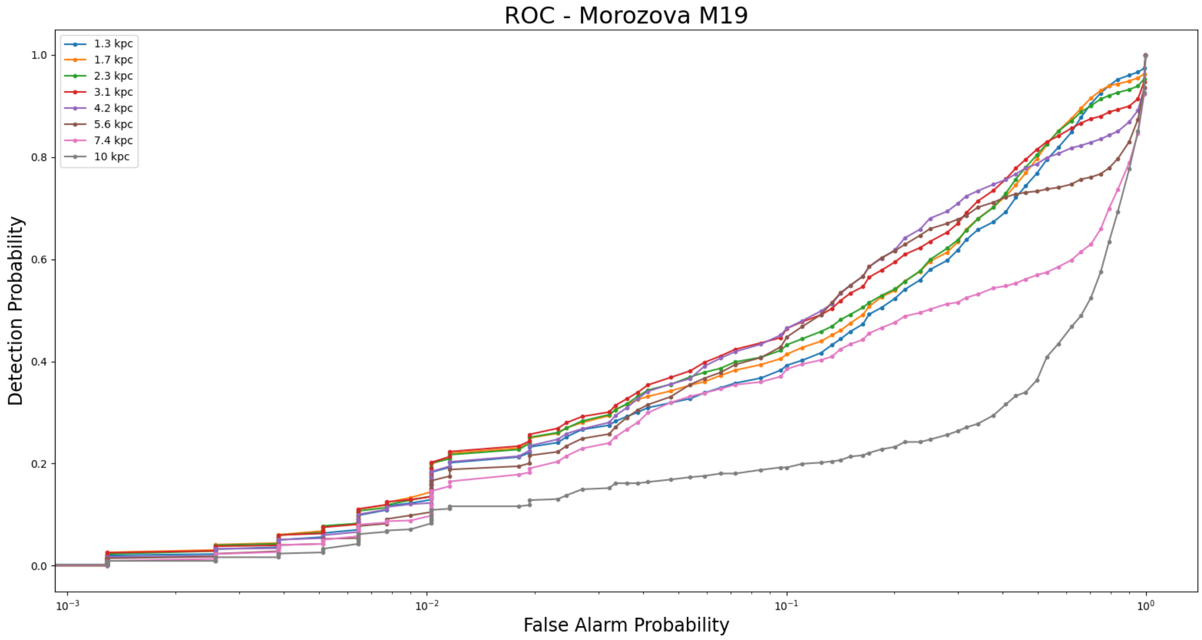

Figure 4.4.36: Receiver Operating Characteristic of Morozova M19 at distances between 1.3 and 10 kpc. Along the x axis there is False Alarm Probability (FAP) and along the y axis there is Detection Probability (DP). Detection Probability increases with False Alarm Probability

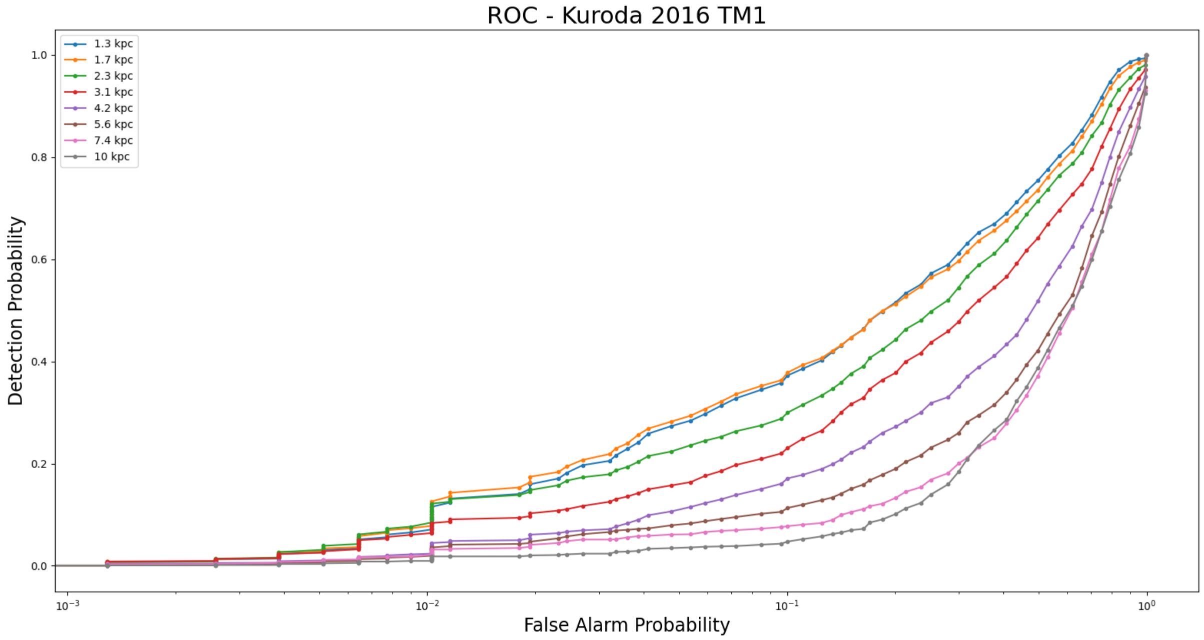

Figure 4.4.37: Receiver Operating Characteristic of Kuroda 2016 TM1 at distances between 1.3 and 10 kpc. Along the x axis there is False Alarm Probability (FAP) and along the y axis there is Detection Probability (DP). Detection Probability increases with False Alarm Probability

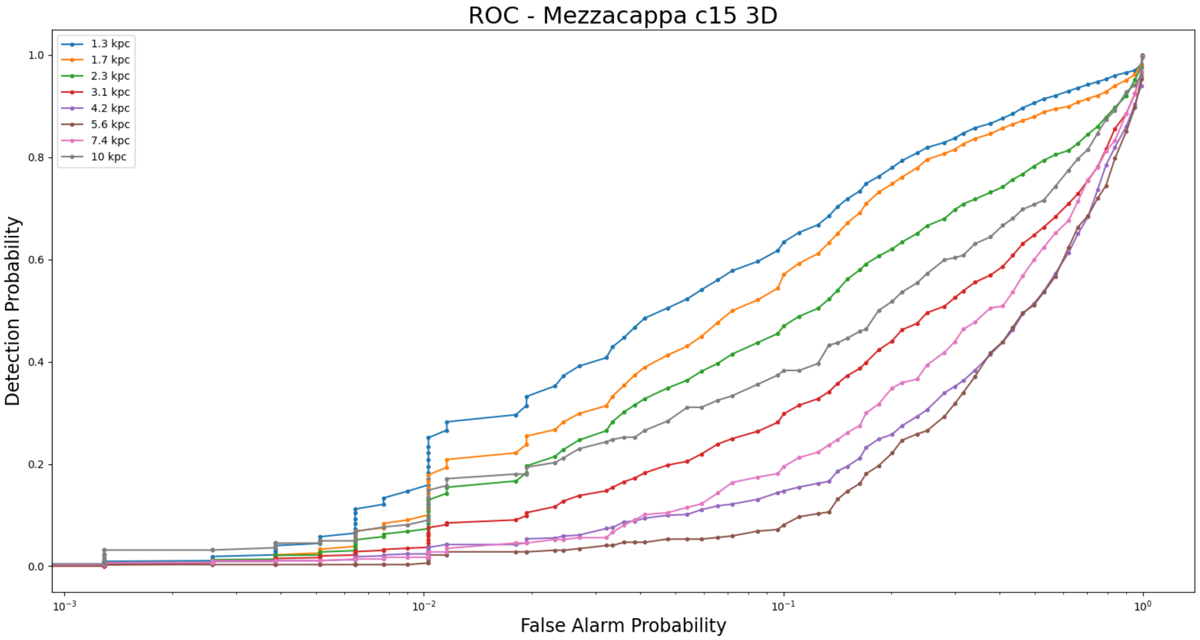

Figure 4.4.38: Receiver Operating Characteristic of Mezzacappa c15 3D at distances between 1.3 and 10 kpc. Along the x axis there is False Alarm Probability (FAP) and along the y axis there is Detection Probability (DP). Detection Probability increases with False Alarm Probability

CHAPTER V

CONCLUSION

As described in chapter 3, we used a novel pipeline MuLaSEcC for our analysis that uses a prior non-parametric estimation of the signal before the data is passed to the network analysis. It finds an estimator of the signal which is a function of noise power spectral density (PSD), signal PSD and the observed data, with an aim to minimize distortion between true signal and estimated signal. Along with MuLaSEcC, we have incorporated a Convolutional Neural Network (CNN) that substantially cuts down background triggers in the GW detectors and hence reduce False Alarm Probability (FAP).

CNN was also used to discriminate between signal and noise in the output triggers of the search pipeline. For most simulated signals and noise triggers it was able to classify over 90% of them correctly as can be seen in the confusion matrix in Chapter 4. The CNN was trained with different types of CCSN GW signal models and background noise triggers. The CCSN GW signals were chosen by performing a multivariate classification analysis with K-Means in a four dimensional parameter space belonging to over 50 different available CCSN waveforms corresponding to various explosion scenarios. Four statistically significant clusters were found. Selected waveforms from each of these waveform classes were chosen to train the CNN.

Efficiency of the searches with waveforms used After training the CNN was tested using 4 different non-rotating waveforms - Powell-Müller s18, Morozova M19, Kuroda 2016 TM1 and Mezzacappa c15 3D described earlier in this thesis. Detection efficiency curves were generated as a function of distance. From the efficiency curve it is evident that MuLaSEcC was able to detect signals at distances over 10 kpc (galactic center) for all waveforms, even though M19 was not part of the training set. This proves that the implementation of a CNN architecture with expanded CCSN

Waveform	d_{max} (kpc)	ε_{40} (kpc)	ε_{10} (kpc)	Features
Powell-Müller s18	13.5	3.6	7.5	g-modes
Mezzacappa c-15 3D	18.0	2.0	4.0	g, p-modes, SASI, convection
Kuroda 2016 TM1	33.0	2.0	21.0	g-modes, SASI
Morozova M19	13.5	1.75	7.5	f, p, g-modes, SASI, convection

Table 5.1: The table summarizes the distances (d_{max}) and efficiencies (ε_{40} and ε_{10}) of the test waveforms along with their signatures.

parameter space has been successful at recognizing CCSN models beyond the ones we trained with. M19 is a difficult test in the sense that it is a very long (1.6 s) and very broadband (250-2000 Hz) waveform. None of the training waveforms have such extended time-frequency evolution. Yet, the MuLaSEcC pipeline successfully detected the injections up to galactic distances and beyond. Table 5.1 summarizes the maximum distance, 40% and 10% efficiencies and features of each of the above test waveforms.

Signal reconstruction is another important part of the analysis. For both s18 and M19 waveforms, MuLaSEcC was able to reconstruct the injected signals at 2.3 kpc and 5.6 kpc over a broader frequency band than seen in cWB reconstructions. This is particularly important because appearance of lower frequencies in the reconstructed signals confirm the assumption of the standing accretion shock instability (SASI).

Receiver Operating Characteristic (ROC) curves were generated from the analysis of Powell-Müller s18, Morozova M19, Kuroda 2016 TM1 and Mezzacappa c15 3D waveforms with MuLaSEcC. Calculations of the detection probability (DP) plotted on the y-axis and the FAP plotted on the x-axis take into account identification of background noise and CCSN signals as determined by post trigger production CNN classification. As expected, the DP goes up with FAP. However, the rise is slower for lower FAP and picks up as FAP approaches 1.0. The most likely explanation of this trend is that, because the CNN classification already cuts down on the FA in the population of the detected triggers, the DP does not rise as it would have in absence of FA removal by the CNN. This is a positive pointer that while the FA rises, it doesn't affect the DP since the CNN effectively cuts down the false events.

One of the important future directions of the analysis will be to perform a blind injection challenge, where a signal will be injected at an unknown point in time in the data and the analysis pipeline will be used to recover and reconstruct the signal. We will also be working on further development of the current CNN both in terms of the network structure itself and the hyper-parameters. A good method to optimize the hyper-parameters would be to use Reinforcement Learning (RL) algorithm, instead of Genetic Algorithm that we have used before.

We plan to expand our network analysis from the current two-detector LIGO (LH) network to LIGO-Virgo (LHV) and then LIGO-Virgo-KAGRA (LHVK) network, which will enhance the performance of the analysis. In future, one can possibly explore implementation of a new type of network analysis with different types of regulators. So far our focus has been in the non-rotating CCSN progenitors. We will be expanding the analysis incorporating all the rotating and non-rotating models.

The MuLaSEcC pipeline used in this analysis is currently under review by the LIGO Scientific Collaboration (LSC) for O4 preparedness. O4 is scheduled to start in March 2023 and run for a year. All four detectors, HLVK, are expected to operate simultaneously during O4.

There are two ways MuLaSEcC will be used in analyzing O4 data - one is when there is a CCSN event, another when there is no CCSN event. In the case of a CCSN event, a zero lag run with data from the detectors will be performed to look for GW signals. If there is no CCSN event during the observation run, it will be used to generate efficiency curves to explore the detection range of various CCSN explosion models.

There are several significant new developments in the work described in this thesis. (1) The implementation of the expanded training parameter space using statistical multivariate clustering and selection of training waveforms to maximize the variance of the characteristic parameters is new. This has expanded the CNN's ability to classify nine different types of waveforms and noise. The CNN can now discriminate between CCSN signal and noise both as a binary classification, and also in a multi-class mode if required. (2) MuLaSEcC is the first CCSN search pipeline that fully integrates ML with a network analysis. The integration of the expanded CNN has strengthened the performance of the pipeline. (3) A paper is in preparation on the results of this analysis of O3b data using the HL network with MuLaSEcC. This is the first end to end analysis of this type. (4) Several new codes have been developed, viz. (a) multi-class CNN codes; (b) ROC generation codes based on new calculations of DR and FAP with ρ thresholds. (5) This work is instrumental in making MuLaSEcC LSC code-review ready.

REFERENCES

[1] T. Foglizzo, R. Kazeroni, J. Guilet, F. Masset, M. González, B. K. Krueger, J. Novak, M. Oertel, J. Margueron, J. Faure, *et al.*, “The explosion mechanism of core-collapse supernovae: progress in supernova theory and experiments,” *Publications of the Astronomical Society of Australia*, vol. 32, 2015.

[2] M. J. Szczepańczyk, J. M. Antelis, M. Benjamin, M. Cavaglia, D. Gondek-Rosińska, T. Hansen, S. Klimenko, M. D. Morales, C. Moreno, S. Mukherjee, *et al.*, “Detecting and reconstructing gravitational waves from the next galactic core-collapse supernova in the advanced detector era,” *Physical Review D*, vol. 104, no. 10, p. 102002, 2021.

[3] A. Einstein, “Die feldgleichungen der gravitation,” *Sitzung der physikalische-mathematischen Klasse*, vol. 25, pp. 844–847, 1915.

[4] B. P. Abbott, R. Abbott, T. Abbott, M. Abernathy, F. Acernese, K. Ackley, C. Adams, T. Adams, P. Addesso, R. Adhikari, *et al.*, “Observation of gravitational waves from a binary black hole merger,” *Physical review letters*, vol. 116, no. 6, p. 061102, 2016.

[5] B. C. Barish and R. Weiss, “Ligo and the detection of gravitational waves,” *Physics Today*, vol. 52, pp. 44–50, 1999.

[6] G. M. Harry, L. S. Collaboration, *et al.*, “Advanced ligo: the next generation of gravitational wave detectors,” *Classical and Quantum Gravity*, vol. 27, no. 8, p. 084006, 2010.

[7] T. Accadia, F. Acernese, M. Alshourbagy, P. Amico, F. Antonucci, S. Aoudia, N. Arnaud, C. Arnault, K. Arun, P. Astone, *et al.*, “Virgo: a laser interferometer to detect gravitational waves,” *Journal of Instrumentation*, vol. 7, no. 03, p. P03012, 2012.

[8] B. P. Abbott, R. Abbott, T. Abbott, F. Acernese, K. Ackley, C. Adams, T. Adams, P. Addesso, R. X. Adhikari, V. Adya, *et al.*, “Search for post-merger gravitational waves from the remnant of the binary neutron star merger gw170817,” *The Astrophysical Journal Letters*, vol. 851, no. 1, p. L16, 2017.

[9] R. Abbott, T. Abbott, S. Abraham, F. Acernese, K. Ackley, C. Adams, R. X. Adhikari, V. Adya, C. Affeldt, M. Agathos, *et al.*, “Gw190814: gravitational waves from the coalescence of a 23 solar mass black hole with a 2.6 solar mass compact object,” *The Astrophysical Journal Letters*, vol. 896, no. 2, p. L44, 2020.

[10] T. Akutsu *et al.*, “Kagra: 2.5 generation interferometric gravitational wave detector. nat astron 3: 35–40,” 2019.

[11] R. Abbott, T. Abbott, F. Acernese, K. Ackley, C. Adams, N. Adhikari, R. Adhikari, V. Adya, C. Affeldt, D. Agarwal, *et al.*, "Gwtc-3: compact binary coalescences observed by ligo and virgo during the second part of the third observing run," *arXiv preprint arXiv:2111.03606*, 2021.

[12] L. S. Collaboration, V. Collaboration, K. S. Collaboration, *et al.*, "The population of merging compact binaries inferred using gravitational waves through gwtc-3," *arXiv preprint arXiv:2111.03634*, 2021.

[13] A. A. Penzias and R. W. Wilson, "A measurement of excess antenna temperature at 4080 mc/s.," *The Astrophysical Journal*, vol. 142, pp. 419–421, 1965.

[14] L. Ferrarese and H. Ford, "Supermassive black holes in galactic nuclei: past, present and future research," *Space Science Reviews*, vol. 116, no. 3, pp. 523–624, 2005.

[15] M. Enoki, K. T. Inoue, M. Nagashima, and N. Sugiyama, "Gravitational waves from supermassive black hole coalescence in a hierarchical galaxy formation model," *The Astrophysical Journal*, vol. 615, no. 1, p. 19, 2004.

[16] R. S. Foster III, *Constructing a pulsar timing array*. University of California, Berkeley, 1990.

[17] D. Yardley, W. Coles, G. Hobbs, J. Verbiest, R. Manchester, W. van Straten, F. Jenet, M. Bailes, N. Bhat, S. Burke-Spolaor, *et al.*, "On detection of the stochastic gravitational-wave background using the parkes pulsar timing array," *Monthly Notices of the Royal Astronomical Society*, vol. 414, no. 2, pp. 1777–1787, 2011.

[18] P. Amaro-Seoane, H. Audley, S. Babak, J. Baker, E. Barausse, P. Bender, E. Berti, P. Binetruy, M. Born, D. Bortoluzzi, *et al.*, "Laser interferometer space antenna," *arXiv preprint arXiv:1702.00786*, 2017.

[19] K. Riles, "Recent searches for continuous gravitational waves," *Modern Physics Letters A*, vol. 32, no. 39, p. 1730035, 2017.

[20] M. Sieniawska and M. Bejger, "Continuous gravitational waves from neutron stars: current status and prospects," *Universe*, vol. 5, no. 11, p. 217, 2019.

[21] R. Easther and E. A. Lim, "Stochastic gravitational wave production after inflation," *Journal of Cosmology and Astroparticle Physics*, vol. 2006, no. 04, p. 010, 2006.

[22] N. Christensen, "Stochastic gravitational wave backgrounds," *Reports on Progress in Physics*, vol. 82, no. 1, p. 016903, 2018.

[23] B. P. Abbott, R. Abbott, T. Abbott, M. Abernathy, F. Acernese, K. Ackley, C. Adams, T. Adams, P. Addesso, R. Adhikari, *et al.*, "Gw150914: Implications for the stochastic gravitational-wave background from binary black holes," *Physical review letters*, vol. 116, no. 13, p. 131102, 2016.

[24] K. Hirata, T. Kajita, M. Koshiba, M. Nakahata, Y. Oyama, N. Sato, A. Suzuki, M. Takita, Y. Totsuka, T. Kifune, *et al.*, "Observation of a neutrino burst from the supernova sn1987a," *Physical Review Letters*, vol. 58, no. 14, p. 1490, 1987.

[25] R. Bionta, G. Blewitt, C. Bratton, D. Casper, A. Ciocio, R. Claus, B. Cortez, M. Crouch, S. Dye, S. Errede, *et al.*, “Observation of a neutrino burst in coincidence with supernova 1987a in the large magellanic cloud,” in *Neutrinos And Other Matters: Selected Works of Frederick Reines*, pp. 340–342, World Scientific, 1991.

[26] S. J. Smartt, “Progenitors of core-collapse supernovae,” *arXiv preprint arXiv:0908.0700*, 2009.

[27] P. Ledoux, “Chandrasekhar, s.-an introduction to the study of stellar structure,” *Ciel et Terre*, vol. 74, p. 379, 1958.

[28] W. Bambynek, H. Behrens, M. Chen, B. Crasemann, M. Fitzpatrick, K. Ledingham, H. Genz, M. Mutterer, and R. Intemann, “Orbital electron capture by the nucleus,” *Reviews of Modern Physics*, vol. 49, no. 1, p. 77, 1977.

[29] D. Wilkinson, “Nuclear photodisintegration,” *Physica*, vol. 22, no. 6-12, pp. 1039–1061, 1956.

[30] C. Y. Cardall, “Degeneracy, the virial theorem, and stellar collapse,” *arXiv preprint arXiv:0812.0114*, 2008.

[31] V. Imshennik and E. Zabrodina, “Hydrodynamic models for explosions of rapidly rotating and collapsing supernovae with allowance for iron dissociation/recombination,” *Astronomy Letters*, vol. 25, pp. 93–110, 1999.

[32] A. Marek and H.-T. Janka, “Delayed neutrino-driven supernova explosions aided by the standing accretion-shock instability,” *The Astrophysical Journal*, vol. 694, no. 1, p. 664, 2009.

[33] C. Cutler and K. S. Thorne, “An overview of gravitational-wave sources,” *General Relativity and Gravitation*, pp. 72–111, 2002.

[34] B. P. Abbott, R. Abbott, T. Abbott, F. Acernese, K. Ackley, C. Adams, T. Adams, P. Addesso, R. Adhikari, V. B. Adya, *et al.*, “Gw170817: observation of gravitational waves from a binary neutron star inspiral,” *Physical review letters*, vol. 119, no. 16, p. 161101, 2017.

[35] G. Tammann, W. Loeffler, and A. Schroeder, “The galactic supernova rate,” *The Astrophysical Journal Supplement Series*, vol. 92, pp. 487–493, 1994.

[36] “Supernova waveforms webpage.” www.stellarcollapse.org.

[37] M. J. Szczepańczyk, J. M. Antelis, M. Benjamin, M. Cavaglià, D. Gondek-Rosińska, T. Hansen, S. Klimenko, M. D. Morales, C. Moreno, S. Mukherjee, G. Nurbek, J. Powell, N. Singh, S. Sitmukhambetov, P. Szewczyk, O. Valdez, G. Vedovato, J. Westhouse, M. Zanolin, and Y. Zheng, “Detecting and reconstructing gravitational waves from the next galactic core-collapse supernova in the advanced detector era, phys,” *Rev. D*, vol. 104, no. 10200, p. 2, 2021.

[38] T. Kuroda, K. Kotake, and A. T. Takiwaki, “New gravitational-wave signature from standing accretion shock instability in supernovae,” *The Astrophysical Journal Letters*, vol. 14, p. 6, 2016.

[39] T. Kuroda, K. Kotake, K. Hayama, and T. Takiwaki, “Correlated signatures of gravitational-wave and neutrino emission in three-dimensional general-relativistic core-collapse supernova simulations,” *Astrophysical Journal*, vol. 851, p. 1, 2017.

[40] J. W. Murphy, C. D. Ott, and A. Burrows, “Apj,” vol. 707, p. 1173, 2009.

[41] B. Muller, H. T. Janka, and A. Marek, “Apj,” vol. 766, p. 43, 2013.

[42] T. Akutsu, M. Ando, K. Arai, *et al.*, “Kagra: 2.5 generation interferometric gravitational wave detector,” *Nat Astron*, vol. 3, pp. 35–40, 2019.

[43] S. Richers, C. D. Ott, E. Abdikamalov, E. O’Connor, and C. Sullivan, “Equation of state effects on gravitational waves from rotating core collapse, phys,” *Rev. D*, vol. 95, p. 063019, 2017.

[44] E. O’Connor and C. D. Ott, “The progenitor dependence of the pre-explosion neutrino emission in core collapse supernovae,” *The Astrophysical Journal*, vol. 762, p. 2, 2013.

[45] E. O’Connor and S. Couch, *Exploring Fundamentally Three-dimensional Phenomena in High-fidelity Simulations of Core-collapse Supernovae*. The Astrophysical Journal, 2018.

[46] S. Scheidegger, R. K"appeli, S. C. Whitehouse, and G. T. Fischer, “waves from supernova matter, and m,” *Liebend"orfer, Astron. Astrophys.*, vol. 514, 2010.

[47] B. P. Abbott *et al.*, “(ligo scientific collaboration and virgo collaboration), first targeted search for gravitational-wave bursts from core-collapse supernovae in data of first-generation laser interferometer detectors, phys,” *Rev. D*, vol. 94, no. 10200, p. 1, 2016.

[48] B. P. Abbott *et al.*, “(ligo scientific collaboration and virgo collaboration, asas-sn collaboration, dlt40 collaboration), optically targeted search for gravitational waves emitted by core-collapse supernovae during the first and second observing runs of advanced ligo and advanced virgo, phys,” *Rev. D*, vol. 101, p. 084002, 2020.

[49] K. Hayama, T. Kuroda, K. Kotake, and T. Takiwaki, “Circular polarization of gravitational waves from non-rotating supernova cores: a new probe into the pre-explosion hydrodynamics,” *MNRAS 000*, pp. 1–5, 2018.

[50] S. E. Gossan, P. Sutton, A. S. P., M. Z. A., K. Gill, and C. D. Ott, “Observing gravitational waves from core-collapse supernovae in the advanced detector era,” *Physical Review D*, vol. 93, p. 4, 2016.

[51] D. Lai, “in aip conf,” in *Proc. 575: Astrophysical Sources for Ground-Based Gravitational Wave Detectors*, p. 246: J. M. Centrella, 2001.

[52] C. D. Ott, A. Burrows, T. A. Thompson, E. Livne, and R. Walder, “Astrophys,” *J. Suppl*, vol. 164, p. 130, 2006.

[53] P. M.-R. M. A. Bizouard, A. Torres-Forné, M. Obergaulinger, P. Cerdá-Durán, N. Christensen, J. A. Font, and R. Meyer, “Inference of proto-neutron star properties from gravitational-wave data in core-collapse supernovae,” *[gr-qc]*, vol. 2020.

[54] S. Mukherjee, G. Nurbek, and O. Valdez, “Study of efficient methods of detection and reconstruction of gravitational waves from nonrotating 3d general relativistic core collapse supernovae explosion using multilayer signal estimation method, phys,” *Rev. D*, vol. 103, p. 10300, May 2021.

[55] S. Mukherjee, L. Salazar, J. Mittelstaedt, and O. Valdez, “New method for enhanced efficiency in detection of gravitational waves from supernovae using coherent network of detectors,” *Physical Review D*, vol. 96, no. 10, p. 104033, 2017.

[56] N. Raza, J. McClever, G. Dalya, and P. Raffai, *Prospects for reconstructing the gravitational-wave signals from core-collapse supernovae with Advanced LIGO-Virgo and the BayesWave algorithm, [astro-ph.* E], 2022.

[57] N. Cornish, “Neil and t,” *Littenberg, BayesWave: Bayesian Inference for Gravitational Wave Bursts and Instrument Glitches,Classical and Quantum Gravity*, vol. 32, 2015.

[58] M. Szczepanczyk and M. Zanolin, “Gravitational waves from a core-collapse supernova: Perspectives with detectors in the late 2020s and early 2030s, gravitational waves from a core-collapse supernova: Perspectives with detectors in the late 2020s and early 2030s,” *Galaxies*, vol. 10, p. 70, 2022.

[59] V. Srivastava, S. Ballmer, D. A. Brown, C. Afle, A. Burrows, D. Radice, and D. Vartanyan, “Detection prospects of core-collapse supernovae with supernova-optimized third-generation gravitational-wave detectors, phys,” *Rev. D*, vol. 100, p. 043026, 2019.

[60] J. Hough and S. Rowan, “Laser interferometry for the detection of gravitational waves,” *Journal of Optics A: Pure and Applied Optics*, vol. 7, no. 6, pp. S257–S264, 2005.

[61] J. M. Antelis, M. Cavaglia, T. Hansen, M. D. Morales, C. Moreno, S. Mukherjee, M. J. Szczepańczyk, and M. Zanolin, “Using supervised learning algorithms as a follow-up method in the search of gravitational waves from core-collapse supernovae, phys,” *Rev. D*, vol. 105, April 2022.

[62] A. Iess, E. Cuoco, F. Morawski, and J. Powell, “Core-collapse supernova gravitational-wave search and deep learning classification, mach,” *Learn.: Sci. Techno*, 2020. In press.

[63] M. Cavaglia, S. Gaudio, T. Hansen, K. Staats, M. Szczepanczyk, and M. Zanolin, “Improving the background of gravitational-wave searches for core collapse supernovae: a machine learning approach,” *Machine Learning: Science and Technology*, vol. 1, 2020.

[64] M. L. Chan, I. S. Heng, and C. Messenger, “Detection and classification of supernova gravitational wave signals: A deep learning approach,” *Physical Review D*, 2020. Accepted.

[65] D. George, H. Shen, E. A. Huerta, and G. C. and, “and clustering for ligo with deep transfer learning, phys,” *Rev. D*, vol. 97, no. 10150, p. 1, 2018.

[66] M. L. Portilla, I. D. Palma, M. Drago, P. Cerda-Duran, and F. Ricci, “Deep learning for multimessenger core-collapse supernova detection,” vol. 2020.

[67] P. Astone, P. Cerdá-Durán, I. D. Palma, M. Drago, F. Muciaccia, C. Palomba, and F. Ricci, “New method to observe gravitational waves emitted by core collapse supernovae,” *Phys Rev D*, vol. 98, no. 12200, p. 2, 2018.

[68] R. Abbott, T. D. Abbott, F. Acernese, K. Ackley, C. Adams, N. Adhikari, R. Adhikari, V. Adya, C. Affeldt, D. Agarwal, *et al.*, “All-sky search for short gravitational-wave bursts in the third advanced ligo and advanced virgo run,” *Physical Review D*, vol. 104, no. 12, p. 122004, 2021.

[69] B. Abbott, R. Abbott, T. Abbott, S. Abraham, F. Acernese, K. Ackley, C. Adams, V. Adya, C. Affeldt, M. Agathos, *et al.*, “Optically targeted search for gravitational waves emitted by core-collapse supernovae during the first and second observing runs of advanced ligo and advanced virgo,” *Physical Review D*, vol. 101, no. 8, p. 084002, 2020.

[70] M. Drago, S. Klimenko, C. Lazzaro, E. Milotti, G. Mitselmakher, V. Necula, B. O’Brian, G. A. Prodi, F. Salemi, M. Szczepanczyk, *et al.*, “Coherent waveburst, a pipeline for unmodeled gravitational-wave data analysis,” *SoftwareX*, vol. 14, p. 100678, 2021.

[71] S. Klimenko and G. Mitselmakher, “A wavelet method for detection of gravitational wave bursts,” *Classical and Quantum Gravity*, vol. 21, no. 20, p. S1819, 2004.

[72] S. Klimenko, S. Mohanty, M. Rakhmanov, and G. Mitselmakher, “Constraint likelihood analysis for a network of gravitational wave detectors,” *Physical Review D*, vol. 72, no. 12, p. 122002, 2005.

[73] S. Klimenko, S. Mohanty, M. Rakhmanov, and G. Mitselmakher, “Constraint likelihood method: generalization for colored noise.,” in *Journal of Physics: Conference Series*, vol. 32, p. 003, IOP Publishing, 2006.

[74] S. Klimenko, I. Yakushin, A. Mercer, and G. Mitselmakher, “A coherent method for detection of gravitational wave bursts,” *Classical and Quantum Gravity*, vol. 25, no. 11, p. 114029, 2008.

[75] R. Brun and F. Rademakers, “Root—an object oriented data analysis framework,” *Nuclear instruments and methods in physics research section A: accelerators, spectrometers, detectors and associated equipment*, vol. 389, no. 1-2, pp. 81–86, 1997.

[76] I. Antcheva, M. Ballintijn, B. Bellenot, M. Biskup, R. Brun, N. Buncic, P. Canal, D. Casadei, O. Couet, V. Fine, *et al.*, “Root—a c++ framework for petabyte data storage, statistical analysis and visualization,” *Computer Physics Communications*, vol. 180, no. 12, pp. 2499–2512, 2009.

[77] V. Necula, S. Klimenko, and G. Mitselmakher, “Transient analysis with fast wilson-daubechies time-frequency transform,” in *Journal of Physics: Conference Series*, vol. 363, p. 012032, IOP Publishing, 2012.

[78] D. Zhang, “Wavelet transform,” in *Fundamentals of image data mining*, pp. 35–44, Springer, 2019.

[79] I. Daubechies, A. Grossmann, and Y. Meyer, “Painless nonorthogonal expansions,” *Journal of Mathematical Physics*, vol. 27, no. 5, pp. 1271–1283, 1986.

[80] C. E. Heil and D. F. Walnut, “Continuous and discrete wavelet transforms,” *SIAM review*, vol. 31, no. 4, pp. 628–666, 1989.

[81] P. Delsarte and Y. Genin, “On the splitting of classical algorithms in linear prediction theory,” *IEEE Transactions on Acoustics, Speech, and Signal Processing*, vol. 35, no. 5, pp. 645–653, 1987.

[82] W. G. Anderson, P. R. Brady, J. D. Creighton, and E. E. Flanagan, “Excess power statistic for detection of burst sources of gravitational radiation,” *Physical Review D*, vol. 63, no. 4, p. 042003, 2001.

[83] L. Cadonati, “Coherent waveform consistency test for ligo burst candidates,” *Classical and Quantum Gravity*, vol. 21, no. 20, p. S1695, 2004.

[84] S. Albawi, T. A. Mohammed, and S. Al-Zawi, “Understanding of a convolutional neural network,” in *2017 international conference on engineering and technology (ICET)*, pp. 1–6, Ieee, 2017.

[85] N. Kalchbrenner, E. Grefenstette, and P. Blunsom, “A convolutional neural network for modelling sentences,” *arXiv preprint arXiv:1404.2188*, 2014.

[86] O. Abdel-Hamid, A.-r. Mohamed, H. Jiang, and G. Penn, “Applying convolutional neural networks concepts to hybrid nn-hmm model for speech recognition,” in *2012 IEEE international conference on Acoustics, speech and signal processing (ICASSP)*, pp. 4277–4280, IEEE, 2012.

[87] M. Liang and X. Hu, “Recurrent convolutional neural network for object recognition,” in *Proceedings of the IEEE conference on computer vision and pattern recognition*, pp. 3367–3375, 2015.

[88] W. S. Sarle, “Neural networks and statistical models,” 1994.

[89] K. Fukushima, S. Miyake, and T. Ito, “Neocognitron: A neural network model for a mechanism of visual pattern recognition,” *IEEE transactions on systems, man, and cybernetics*, no. 5, pp. 826–834, 1983.

[90] T. Guo, J. Dong, H. Li, and Y. Gao, “Simple convolutional neural network on image classification,” in *2017 IEEE 2nd International Conference on Big Data Analysis (ICBDA)*, pp. 721–724, IEEE, 2017.

[91] R. Martin, “Noise power spectral density estimation based on optimal smoothing and minimum statistics,” *IEEE Transactions on speech and audio processing*, vol. 9, no. 5, pp. 504–512, 2001.

[92] N. Wiener, N. Wiener, C. Mathematician, N. Wiener, N. Wiener, and C. Mathématicien, *Extrapolation, interpolation, and smoothing of stationary time series: with engineering applications*, vol. 113. MIT press Cambridge, MA, 1949.

[93] J. Powell and B. Müller, “Gravitational wave emission from 3d explosion models of core-collapse supernovae with low and normal explosion energies,” *Monthly Notices of the Royal Astronomical Society*, vol. 487, no. 1, pp. 1178–1190, 2019.

[94] V. Morozova, D. Radice, A. Burrows, and D. Vartanyan, “The gravitational wave signal from core-collapse supernovae,” *The Astrophysical Journal*, vol. 861, no. 1, p. 10, 2018.

[95] T. Kuroda, K. Kotake, and T. Takiwaki, “A new gravitational-wave signature from standing accretion shock instability in supernovae,” *The Astrophysical Journal Letters*, vol. 829, no. 1, p. L14, 2016.

[96] A. Mezzacappa, P. Marronetti, R. E. Landfield, E. J. Lentz, K. N. Yakunin, S. W. Bruenn, W. R. Hix, O. B. Messer, E. Endeve, J. M. Blondin, *et al.*, “Gravitational-wave signal of a core-collapse supernova explosion of a 15 m star,” *Physical Review D*, vol. 102, no. 2, p. 023027, 2020.

BIOGRAPHICAL SKETCH

Shahrear Khan Faisal was born in Kushtia, Bangladesh. He completed high school from Govt. M. M. City College, Khulna, Bangladesh in 2014. After that he received his Bachelor of Science with a major in Mechanical Engineering from Bangladesh University of Engineering and Technology in April 2019. He earned a Master of Science in Interdisciplinary Studies with a concentration in Science and Technology from University of Texas Rio Grande Valley in December 2022. Shahrear Khan's research has been in collaboration with LIGO Scientific Collaboration which has resulted in various talks and posters including LIGO and APS meetings. His email is faisalshahrearkhan@gmail.com.